Transport Phenomena in Liquid Phase Diffusion Growth of Silicon Germanium

by

Neil Alexander Armour
B.A., University of California, Berkeley, 2002
M.A.Sc., University of Victoria, 2006

A Dissertation Submitted in Partial Fulfillment of the
Requirements for the Degree of

DOCTOR OF PHILOSOPHY

in the Department of Mechanical Engineering

Transport Phenomena in Liquid Phase Diffusion Growth of Silicon Germanium

by

Neil Alexander Armour
B.A., University of California, Berkeley, 2002
M.A.Sc., University of Victoria, 2006

Supervisory Committee

Dr. Sadik Dost, Supervisor
(Department of Mechanical Engineering)

Dr. Henning Struchtrup, Departmental Member
(Department of Mechanical Engineering)

Dr. Rustom Bhiladvala, Departmental Member
(Department of Mechanical Engineering)

Dr. Alexandre Brolo, Outside Member
(Department of Chemistry)

Supervisory Committee

Dr. Sadik Dost, Supervisor
(Department of Mechanical Engineering)

Dr. Henning Struchtrup, Departmental Member
(Department of Mechanical Engineering)

Dr. Rustom Bhiladvala, Departmental Member
(Department of Mechanical Engineering)

Dr. Alexandre Brolo, Outside Member
(Department of Chemistry)

ABSTRACT

Silicon Germanium, SiGe, is an important emerging semiconductor material. In order to optimize growth techniques for SiGe production, such as Liquid Phase Diffusion, LPD, or Melt Replenishment Czochralski, a good understanding of the transport phenomena in the melt is required. In the context of the Liquid Phase Diffusion growth technique, the transport phenomena of silicon in a silicon-germanium melt has been explored. Experiments isolating the dissolution and transport of silicon into a germanium melt have been conducted under a variety of flow conditions. Preliminary modeling of these experiments has also been conducted and agreement with experiments has been shown. In addition, full LPD experiments have also been conducted under varying flow conditions. Altered flow conditions were achieved through the application of a variety of magnetic fields. Through the experimental and modeling work better understanding of the transport mechanisms at work in a silicon-germanium melt has been achieved.

Contents

List of Tables

List of Figures

ACKNOWLEDGEMENTS

I would like to thank all the members of the Crytsal Growth Laboratory and the Department of Mechanical Engineering Staff and Faculty for their help in completing this work. In addition, I would further like to thank Dr Sadik Dost for his help, support and mentorship.

I would also like to thank the following funding agencies for the resources provided to complete this work:

Natural Sciences and Engineering Research Council of Canada

Canadian Space Agency

DEDICATION

To my parents for their support and to Kyla for her endless patience, help and encouragement.

Chapter 1

Introduction

1.1 Motivation

The $Si_xGe_{1\text{-}x}$ material system is of interest over its entire composition range [1–3]. The material is currently in use in device layers for optoelectronics, radiation detectors, heterojunction structures and other similar applications [4–7]. Bulk material for use as a device substrate is not currently widely available [2, 8, 9]. Bulk material is very difficult to produce using common melt growth crystal production techniques. This is because the material exhibits a large separation between the solidus and liquidus lines in its phase diagram. The miscibility gap makes controlling the composition in the growing material very difficult when using typical melt growth techniques. SiGe devices currently in use are typically grown by molecular beam epitaxy or chemical vapor deposition on silicon substrates [1, 10].

Bulk SiGe wafers would have application in the solar energy industry as a substrate material for a multi-junction solar cell [5,11]. In addition, bulk material could be used as a substrate for system-on-a-chip applications where optoelectronic components are integrated with other electronics on the same die. This principle has already seen limited use in optoelectronics and detector applications where the radiation sensor and the readout electronics are on the same SiGe die [12–15].

For SiGe, the band gap and lattice parameter vary with the composition of the material [2, 16, 17]. This allows for the material to be tuned to specific applications by adjusting the composition. The composition of the material can also be graded. This creates material with a graded band gap such as that used in heterobipolar transistors [8, 9, 18–20]. The variation of lattice parameter with composition allows the material to be adjusted to accommodate different device layers with little to no strain from lattice mismatch. This can be used to integrate Type III-V semiconductor materials, such as GaAs, directly on a SiGe die with other Si based electronics also included [3, 21, 22].

In order to produce high quality bulk material, better understanding of the mass transport properties of silicon germanium is required. Currently little data exists on the properties of silicon germanium melts at high temperatures. The high melting point of silicon germanium makes studying these properties in isolation very difficult.

The material system has a number of interesting properties from a transport perspective. The material is fully miscible across its composition range. There is a large separation between the solidus and liquidus lines. This leads to segregation of germanium back into the melt as material solidifies. The silicon species exhibits buoyancy in the melt. This leads to solutal driven flow structures in the melt [23–26]. The flow structure in the melt is also influenced by thermally driven buoyancy flows. The combination of these features leads to material system with numerous mass transport processes in effect during a growth process.

The Liquid Phase Diffusion crystal growth technique for producing silicon germanium was previously developed at the University of Victoria [25]. In the course of this work, graded blocks of single crystal SiGe were produced. In addition, a numerical model for the growth system was developed [25, 26]. One of the difficulties encountered in this process was the rate of silicon transported through the melt. The growth interface exhibited significant curvature evolution during growth. This made the radial composition gradients in most extracted wafers unsuitable for use. To flatten the growth interface, the application of magnetic fields to alter the melt flow structure was examined numerically. This showed that alteration of the flow field could aid in flattening the growth interface.

The Liquid Phase Diffusion growth technique is an interesting crystal growth technique as the growth process takes place very close to equilibrium. Growth is driven by a thermal gradient applied to the growth system. The temperature gradient is not moved nor is the sample translated. Instead growth is driven by diffusion of silicon from a hot dissolution interface to a cold growth interface. The dissolution interface is at the top of the melt where a silicon source is placed. The growth interface is at the bottom of the melt where germanium single crystal seed is placed. As transport proceeds, the silicon constitutionally super-cools the melt at the growth interface and solidification occurs. The buoyancy of the silicon in the melt has been shown to suppress thermally driven convective buoyancy flows in the melt. This leads to transport through the melt being diffusion dominated. The slow transport of silicon through the melt, by a diffusion dominated process, leads to slow growth rates but also means that there is very stable silicon transport in the melt and a very stable growth interface due to the lack of flow.

Given the properties above, the Liquid Phase Diffusion process offers a good platform for studying the transport properties of silicon in the melt. Any modification in flow structure can be examined against the backdrop of a diffusion dominated process. As the transport proceeds diffusion dominated, the growth rate of the crystal and the dissolution rate of the silicon source should provide information on the effective diffusion coefficient of silicon for the given conditions in the melt.

In addition to information relevant to the Liquid Phase Diffusion growth process, the transport of silicon from a dissolution interface into the melt is of interest in other crystal growth techniques. One specific application is melt-replenishment Czochralski growth. The Czochralski melt growth technique is the technique of choice for producing large bulk high quality crystals very efficiently. This technique is not easily utilized in silicon germanium growth due to the large separation between the solidus and liquidus lines. To keep the composition in the growing crystal constant, the melt must be replenished with silicon [27]. One method of achieving this is to feed silicon rods into the melt in an arrangement similar to the Liquid Phase Diffusion system. In this case, the transport of silicon from the dissolution interface to the growth interface is key in keeping the composition of the growing crystal constant.

The Liquid Phase Diffusion technique could be used to produce high quality seed material for a successive growth technique, such as Czochralski growth. Ultimately it will be a technique like melt replenishment Czochralski that makes the production of SiGe substrates viable for widespread use. In order to achieve the optimization of these techniques, good understanding of the transport of the silicon species in the melt is required. In both Liquid Phase Diffusion and melt replenishment Czochralski, the transport of silicon through the melt from a dissolution interface will determine the quality of the grown material.

1.2 Approach

Two main experimental configurations were examined in the course of this work. First a simplified Liquid Phase Diffusion, LPD, system was examined. This system isolated the dissolution interface as much as possible from flow effects present in the LPD system. These experiments are titled the Dissolution Experiments. In addition to these experiments, the full LPD system was examined under a variety of applied stimuli including magnetic fields, translation and altered thermal field.

1.2.1 Dissolution Experiments

The Dissolution Experiments were designed to examine the dissolution of silicon into a silicon germanium melt. To remove thermal flow effects, the experiments were carried out at a constant temperature. To clearly define a time period for the experiments, a system of rapidly heating and quenching the samples was developed. This allowed the experiment start time and end time to be known with reasonable accuracy.

The starting material arrangement is a silicon source with pure germanium as the melt. The experiments were conducted at a temperature consistent with the LPD experiments. The diameter of the crucible was also kept consistent with the LPD system. The effect of solutal buoyancy was investigated by varying the orientation of the dissolution interface with respect to gravity. Marangoni convective flows were investigated by varying the free surface condition of the melt. The Dissolution Experiments were also conducted with a static magnetic field applied. The static magnetic field should serve to suppress any remaining convective flow in the melt. The combination of experimental conditions should make it possible to show the relative contribution of each transport effect to the overall silicon transport in the system. Of specific interest is the diffusion contribution to mass transport as this is the primary mass transport mechanism in LPD growth of silicon germanium.

In addition to the samples processed on a similar scale to the LPD experiments, small diameter samples were also processed. In these experiments, it is expected that the flow structure in the melt will be further reduced due to the flow interaction with the crucible wall. This should further limit transport in the melt to diffusion dominated. The temperature dependence of the dissolution phenomena is also examined in these experiments.

For the samples processed in the Dissolution Experiments, the dissolved height of silicon is measured. This measure gives the amount of silicon dissolved in the experiment time and should directly relate to the amount of silicon transport in the melt. In addition to the dissolved height, the distribution of silicon in the melt can be qualitatively analyzed by utilizing an anisotropic etchant to reveal structure in the solidified material. The structure of the samples change with the silicon concentration. To quantitatively analyze the silicon composition in the melt, the samples were analyzed with a scanning electron microscope, SEM, equipped with an energy dispersive x-ray spectrometer, EDS.

To better understand the transport and flow phenomena observed in this work, a variety of numerical models have been prepared by the author and collaborators. These models and the insight they provide into the transport processes present in the melt will be discussed. Specifically, a configuration similar to that used in LPD, with silicon dissolving from the top of the melt, has been extensively modeled.

The height of silicon dissolved and the distribution of silicon in the melt gives insight into the transport mechanisms at work. Better understanding of the effective diffusion coefficient of silicon in the melt will be gained from the dissolved height of silicon and its distribution through the melt. The parameters that affect the transport in the melt and their relative contribution to the overall mass transport will be analyzed. With better information on the factors affecting the transport of silicon in the melt, the LPD growth system can be optimized to take advantage of favorable mechanisms of silicon transport.

This work has been published by the author and collaborators in eight articles [28–35].

1.2.2 Liquid Phase Diffusion Experiments

The Liquid Phase Diffusion experiments performed examine the growth process under a variety of applied stimuli. Three magnetic field conditions were used to vary the flow structure in the melt. In addition, the crucible was translated and a heat sink was used with the crucible. Both of these conditions effectively modify the thermal field of the growth system. The transport of silicon in the melt varies with each stimulus. The effect of each stimulus to modify the growth process will be shown and the change to the silicon transport analyzed and discussed. This work will provide better direction in optimizing the LPD growth system.

A static magnetic field is used to suppress convective flow in the melt and increase the relative contribution of diffusion to the silicon mass transport. A rotating magnetic field is used to induce controlled mixing in the melt and increase the transport of silicon from tangential flow structure. The two fields are combined to see if the suppression of convective flows in the melt, with the additional mixing induced by the rotating field, will increase or decrease the overall mass transport rate of silicon.

The LPD process currently produces a graded composition crystal. In order to flatten the axial composition profile in the crystal, the growth interface must be maintained at a constant temperature. This could be accomplished by translating the LPD crucible with the growth rate. The crucible has been translated in this work to see the effect of a time dependant temperature gradient on the transport in the system. In these experiments, the translation velocity was not matched to the growth rate. Instead, a fixed translation rate was used. These experiments provide insight on the time evolution of the growth velocity. In the sections where the axial composition profile flattens the translation velocity and the growth interface velocity are close in value.

Previous LPD experiments were noted to have a significantly curved initial growth interface. This is an undesirable condition for growth. To aid in flattening the growth interface, a heat sink was utilized with the intent to extract heat from the center of the growth interface, reducing the curvature of the interface.

The LPD samples were analyzed in the same fashion as the Dissolution Experiment samples. Structure and qualitative composition information was obtained by differential etching of the samples. Quantitative composition measurements were obtained by analyzing the samples with a SEM equipped with an EDS system.

The most promising mechanisms to improve the transport of silicon in the melt will be shown in this work. These will directly apply to the transport of silicon in the Liquid Phase Diffusion growth of silicon germanium. The same principles that apply to the LPD process will indicate the types of stimuli that produce desirable transport in the melt for general crystal growth processes.

This work has been published by the author in five articles [24,32,36–38].

1.3 Outline

This work will begin with background material in Chapter 2. This includes a brief overview of crystal structure and its relation to semiconductor materials and their behavior. An overview of crystal growth processes and silicon germanium as a semiconductor material will then be discussed. A brief introduction to the foundation of the numerical work presented here is also included.

In Chapter 3, the Dissolution Experiments will be discussed in detail. The experimental procedure and design will be outlined. The results from each set of experimental conditions will be analyzed. This will be followed with a presentation of the numerical work completed by the author and collaborators. Finally, the results from the small diameter dissolution experiments will be presented.

In Chapter 4, the LPD experiments will be presented in similar form to the Dissolution Experiments. The experimental procedure and design will be outlined. The results from each set of experiments will then be discussed in detail.

The contributions of this work will be discussed in Chapter 5. Specifically, the insights into the understanding of silicon transport in a silicon germanium melt will be presented. This will be followed by recommended improvements to the LPD system and the new understanding gained applicable to the Liquid Phase Diffusion transport processes. The application of these findings to other techniques will also be discussed. Future work in the crystal growth of silicon germanium alloys will also be presented.

Chapter 2

Background

This section introduces background information on topics that are related to the work that will be presented in this dissertation. The information here will be discussed in detail sufficient to the work being presented.

2.1 Crystal Structure

Crystal structure is a defining property of most semiconductor materials. As such, good understanding of crystal properties is necessary in the optimization of semiconductor materials.

2.1.1 Crystal Lattice

A crystalline material differs from an amorphous material in that it consists of a pattern of constituents that repeats in space. An amorphous material lacks the pattern of constituents. A result of the crystalline pattern is that all directions in the crystal are not necessary equivalent. In an amorphous material, all directions are statistically equivalent. One example of directions being inequivalent is the spacing between the atoms in the crystal lattice. This distance may change depending on what direction through the material is being considered. This anisotropic nature can also extend to other physical properties of the crystal. This type of variation is not seen in amorphous materials. The structure of the crystal is determined by the nature of the bonding between the constituent materials [39].

The most basic structure in a crystal is the unit cell. The unit cell is what is repeated in space to build the lattice. The unit cell and the lattice overall are patterns

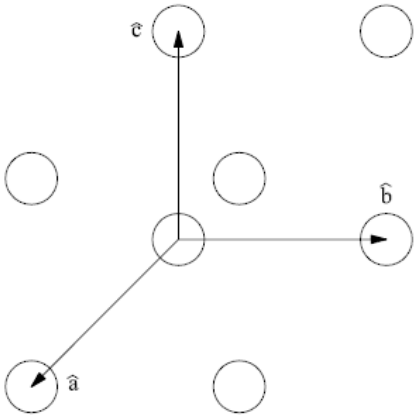

Figure 2.1: Shown is an example of a cubic crystal lattice. The lattice sites are illustrated by the circles. The lattice translations are indicated by the arrows. Any lattice site can be reached by a linear combination of the lattice translations.

of points in space. A lattice translation is defined as a vector that moves from one point on the lattice to another. The set of the translation vectors are reduced to a set of three vectors which correspond to the three closest unique lattice points. The axes of the lattice are defined by the directions of the three lattice translations. A basic unit cell and its lattice translations are shown in Figure 2.1.

The length of a lattice translation is defined as the lattice parameter. The lattice parameter of a crystal is the physical distance between lattice points on a given crystal axis. Due to the repeating nature of the lattice, all lattice points are equivalent and the origin may be defined as any lattice point.

The lattice translations form a basis and can be written as vectors a, b and c. Any lattice point can be defined, in relation to an origin, by a linear combination of the lattice translation vectors, $ua+vb+wc$. In a given lattice, each lattice point is uniquely defined by the numbers uvw. Each linear combination also defines a direction. The direction is defined as $[uvw]$. In this notation scheme, negative numbers are indicated by a bar over the affected number.

2.1.2 Crystal Planes

Three points are required to define a plane in 3D space. In crystallography, planes are defined by use the three intersections of the plane with the lattice axes. These points are represented as m, n and p. These three numbers fully define the plane in

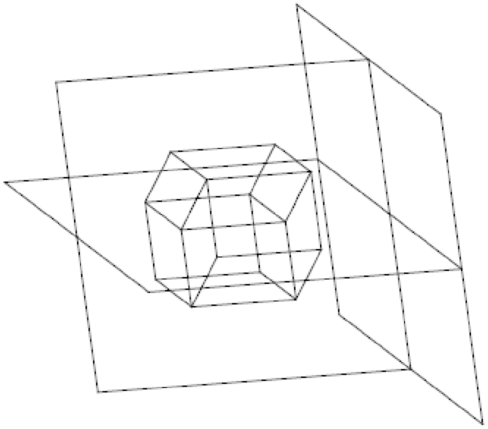

Figure 2.2: The diagram above shows a hexagonal crystal lattice. Three of its crystal planes are indicated by the superimposed rectangles. The hexagonal crystal lattice is found in quartz crystals. Quartz crystals take on the hexagonal shape at a macroscopic scale. This is typical of structure affecting the material morphology.

question. The general equation of a plane is the following,

$$\frac{X}{x} + \frac{Y}{y} + \frac{Z}{z} = C$$

X, Y and Z are points in the plane. x, y and z are the intersections with the axis. The constant C accounts for parallel planes. The plane passing through the origin is considered for simplicity. In this case C is zero. The equation in terms of the intercepts of the lattice axes becomes,

$$\frac{X}{m} + \frac{Y}{n} + \frac{Z}{p} = 0$$

For simplicity, the planes are identified by the reciprocals the intercepts.

$$\begin{aligned} h &= \frac{1}{m} \\ k &= \frac{1}{n} \\ l &= \frac{1}{p} \end{aligned}$$

These three numbers uniquely identify the crystal planes. These numbers are normally written as integers, which usually only involves a change of origin. They are often written in the form (hkl). In this form, the numbers are known as the Miller indices of the plane and are the common notation for specifying crystal planes.

Crystal planes are to be carefully considered in crystal growth. The lattice parameter can vary between planes which can affect the material's suitability for specific device structures. In addition, the growth rate of the material during production can be affected by the crystal plane chosen for growth [40]. A hexagonal crystal and its crystal planes are illustrated in Figure 2.2.

2.1.3 Symmetry Operations and Bravais Lattices

The repetitive nature of a crystal lattice leads to symmetry within the lattice. Types of symmetry include inversion points, rotation axes and mirror planes. New lattice sites can be added to a lattice provided they do not change its symmetry. The lattices able to fill a three dimensional volume with a regular repeating pattern are generally limited to the fourteen Bravais lattices. The fourteen lattices are illustrated in Figure 2.3. Most seemingly more complex patterns can be simplified to one of the Bravais lattices. Generally all solid crystalline materials possess one of these lattices [39].

2.1.4 Crystal Defects

Crystal defects are very important to semiconductor materials. These defects directly effect the electrical performance of the material. Some defects are intentional in order to obtain a desired material property.

2.1.4.1 Point Defects

Point defects are errors in the lattice at a given point. These include vacancies, interstitials, substitutional defects and Frenkel pairs. Vacancies are lattice points that are unoccupied leaving a gap in the lattice. An interstitial defect is an atom or molecule present between lattice points. The combination of a vacancy and an interstitial of a lattice constituent is a Frenkel pair. A substitutional defect is where a lattice constituent has been replaced with a different atom or molecule. The aforementioned defects are illustrated in Figure 2.4.

Impurities in semiconductor materials often manifest as point defects, substitutionally replacing lattice constituents or existing as interstitials between lattice points. Often, impurities in semiconductors are intentional and referred to as dopants.

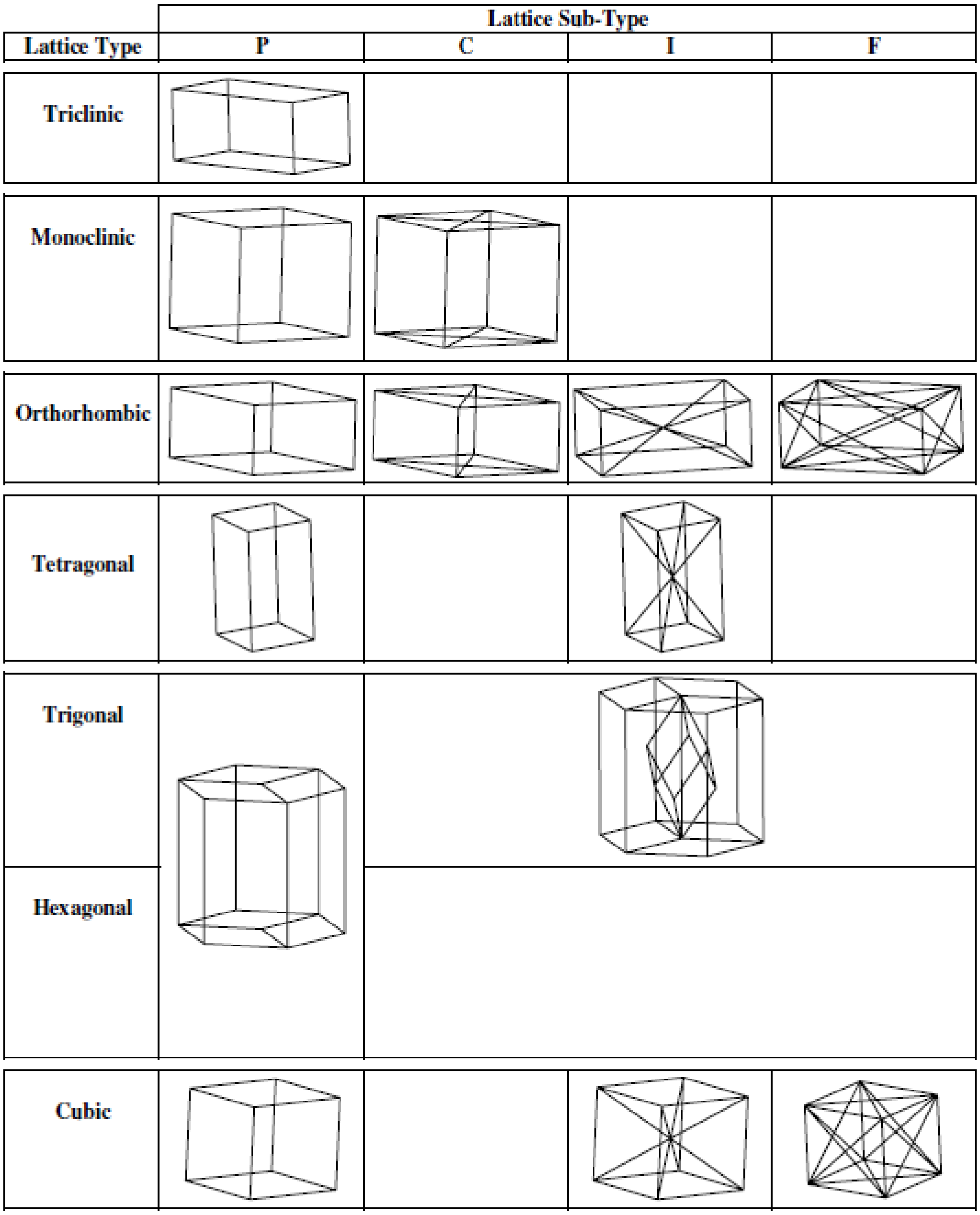

Figure 2.3: The 14 Bravais Lattices are illustrated above. The P column shows the primitive lattices. The other subtypes are generated by inserting new lattice points at symmetry locations. The columns represent the different types of symmetry points used.

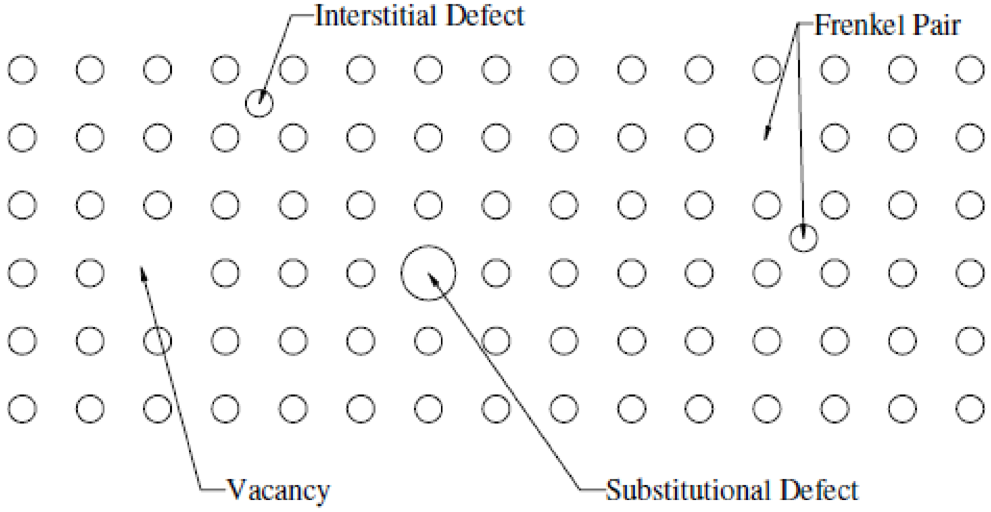

Figure 2.4: The four types of point defects are illustrated above.

Dopants are most often used to change electrical properties but can also effect properties like the lattice parameter.

2.1.4.2 Dislocations

Dislocations are line defects. These defects lower the critical shear stress of the material and allow slip to more easily take place within the lattice. The dislocation lowers the number of bonds to broken to allow slip to occur.

There are two main types of dislocations, edge and screw. An edge dislocation is essentially an extra lattice plane that only extends partially through the lattice. In a four by four square of lattice points, an edge location can be introduced by squeezing an extra half plane into the middle of the lattice. This leaves four lattice points on three edges and five on one edge. In the middle, five planes try to connect to four leaving one dangling connection. This is extended to a three dimensional array by stacking the planes on top of one another. When shear stress is applied on the two lattice edges with four lattice sites opposite one another, the dangling connection in the center will shift towards an edge and slip will occur. Due to the dangling connection, fewer bonds need to be broken as the dangling edge can move within the lattice facilitating slip. An edge dislocation is illustrated in Figure 2.5.

A screw dislocation marks the boundary between slipped and unslipped regions of the lattice. In the transitional region between slipped and unslipped volumes, slip

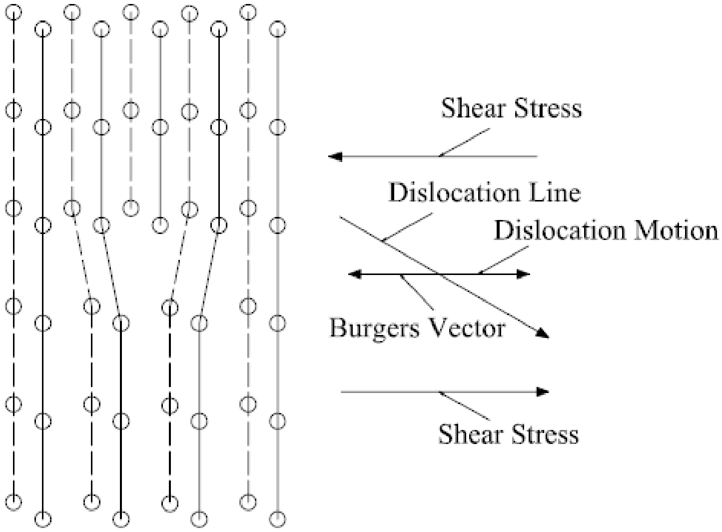

Figure 2.5: An edge dislocation and its relevant vectors are illustrated above.

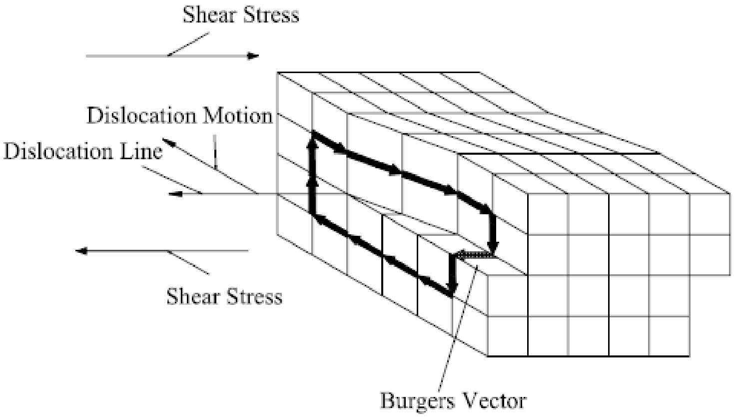

Figure 2.6: A screw dislocation and its relevant vectors are illustrated above.

more easily takes place. This type of dislocation moves into the unslipped region with applied shear stress. The direction the dislocation moves is perpendicular to the slip direction. A screw dislocation is illustrated in Figure 2.6.

Most dislocations present in a crystal are neither purely edge nor purely screw. Instead, combinations of the two types are the most common dislocations present. For semiconductors, dislocations weaken the lattice making the resultant crystals structurally weakened and more prone to damage. In addition, electronically they provide recombination centers for charge carriers, degrading device performance [41].

2.1.4.3 Stacking Faults

Stacking Faults are planar defects that occur when the crystal planes become disordered. For example, a lattice may have three unique planes A, B, and C which are repeated in that order. The ideal stacking of planes would be ABCABCABC continued throughout the material. However, this can become disordered such that it looks like ABCACBABC. The swap of the C and B planes in the middle of the pattern is a stacking fault. Stacking faults can lead to increased internal strain and compromised electrical properties of the material [41].

A specific type of stacking fault is twinning. Twinning is where the stacking pattern is mirrored around a plane. A twinning fault would appear as ABCABCBACBA. The pattern reverses at the second C plane. A twin defect is shown in Figure 2.7.

2.1.4.4 Grain Boundaries

In polycrystalline material, grain boundaries are where two crystal orientations meet. At these boundaries all crystal defects are common. The intersecting lattice orientation cause high strain. This can cause the formation of other defects [41]. In addition, dislocations are often trapped at these boundaries. An example of polycrystalline material is shown in Figure 2.7. Grain boundaries are usually undesirable in semiconductor material to be used for devices. As such, various techniques are used to produce single crystal material with no grain boundaries.

2.2 Semiconductors

Semiconductor materials exhibit conductivity between that of insulators and conductors. Rough divisions of the conductivity spectrum can be made as follows. Conduc-

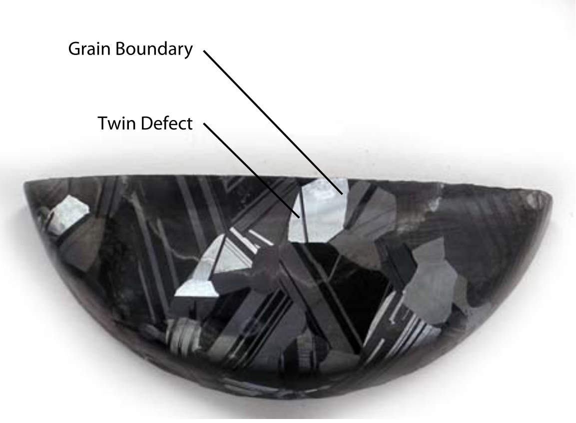

Figure 2.7: The above is a section of polycrystalline CdTe. The grains differ in colouring and have irregular boundaries. Twin defects can be seen in the individual grains. The twins differ from the grain bulk in color and show a very regular boundary through the grain. This boundary will be along a crystal plane. The above sample has been etched to highlight the contrast between grains and twins. Even without the etching, the grains are visible as the reflectivity of the material changes with orientation.

tors are materials with conductivities at or above $10^4 S\ cm^{-1}$. Insulators are materials with conductivities below $10^{-8} S\ cm^{-1}$. The gap between these two regimes is where the semiconductors lie. An intrinsic semiconductor is neither a good insulator nor a good conductor [41].

2.2.1 Energy Band Structure

A band structure of energy levels follows from the crystalline structure of semiconductors. Specifically, it is the periodic potential created by the regular spacing of atoms, like that found in a crystal lattice, which gives rise to the energy band structure found in semiconductors. The energy bands are groupings of energy levels separated by gaps where no energy levels exist. The energy levels can be closely spaced while the bands can be widely spaced. A basic illustration of the band structure is shown in Figure 2.8. When the electrons are at their lowest energy level they are said to be in the ground state. The highest energy band with electrons in their ground state is said to be the valence band. The energy band above the valence band is referred to as the conduction band. The gap between the conduction and valence bands is referred to as the band gap. The band gap determines the relative conductivity of the material. Good conductors will often have valence and conduction bands overlapping.

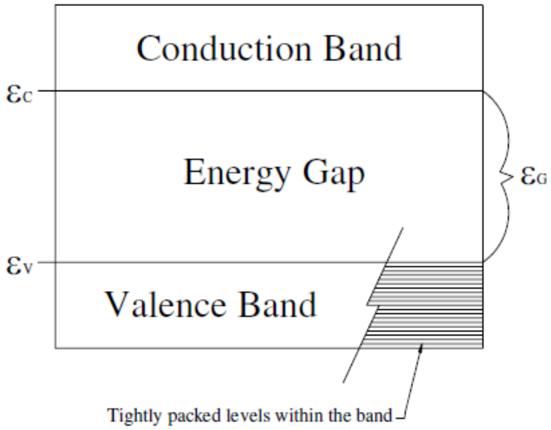

Figure 2.8: Diagram of the energy band structure indicating the fine energy level structure within a band.

A material with a large gap between the valence and conduction bands will tend to be a good insulator. Semiconductors have a gap between the conduction and valence bands somewhere between the two extremes. For electrons to conduct, they need to gain enough energy to transition from the valence band to the conduction band. A large band gap material requires electrons to gain relatively more energy to transition to the conduction band. This makes the material less conductive. A small band gap material requires much less energy for electrons to transition to the conduction band. This makes the material a better conductor. Band gap is an important property for semiconductors as it defines many of their electrical properties [41].

The mechanisms for exciting electrons across the band gap are numerous and varied. Some examples include thermal effects, photon interactions and applied fields. When designing a device such as a charge-coupled device, CCD, the band gap is taken into account to ensure that many conduction electrons will be created when exposed to incident photons of interest. It is the electrons excited into the conduction band which are collected and the intensity of light deduced [42].

2.2.2 Conduction in Semiconductors

An intrinsic semiconductor is a material with very low impurity levels. They are neither conductors nor insulators as previously explained. In this state, when an electron transitions from the valence band to the conduction band, two charge carriers are created. One is the electron now in the conduction band. The other is the hole

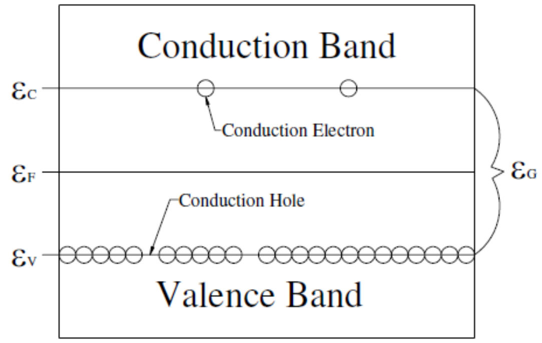

Figure 2.9: A diagram of an intrinsic semiconductor where two electron-hole generation events have occurred. Electrons moving in the valence band will transport the holes, effectively moving positive charge. The relevant band energy levels are also illustrated.

in the valence band created by the transition of the electron into the higher band. This is a pair production event. In intrinsic semiconductors, all charge carriers are the result of pair production events. The hole in the valence band is often considered to be a positive charge carrier. Like the electron in the conduction band, the hole is mobile within the material and it exhibits a very similar behavior to a conduction band electron. This is because the movement of the hole actually involves movement of electrons in the valence band.

The energy associated with the lower edge of the conduction band is denoted ϵ_C. The energy associated with the top edge of the valence band is denoted ϵ_V. The difference between ϵ_C and ϵ_V is the band gap denoted ϵ_G. In a pair production event, the energy transferred to the conduction electron must be at least ϵ_G for the transition to the conduction band to be successful. There is a reference energy level defined within the band gap called the Fermi energy and denoted ϵ_F. The Fermi energy indicates whether the material will form holes or conduction electrons. When it is in the middle of the band gap, the semiconductor is an intrinsic semiconductor and will form hole-electron pairs [43]. An illustration of the relevant energy levels is shown in Figure 2.9.

It is often desirable to increase the conductivity of a semiconductor. This is accomplished by introducing excess charge carriers into the material. Doping the intrinsic semiconductor with an impurity is usually the method employed to add excess carriers. If the added dopant contains more electrons in its valence band than the semiconductor atoms being replaced, then excess electrons have been added. This moves the Fermi energy up towards the conduction band. This type of doping makes the semiconductor n-type. Instead, if the dopant has less electrons in its valence band than the semiconductor material, then excess holes have been added. This moves the Fermi energy towards the valence band and the semiconductor is said to be p-type [41, 42].

2.2.3 Semiconductor Materials

2.2.3.1 Elemental

Two of the most common semiconductor materials are silicon and germanium. These elements in their crystalline form are good semiconductor materials as they possess favorable band structure. The majority of current semiconductor devices are based on silicon semiconductor technology. Many of the first semiconductor devices were based on germanium and its use continues today. Both elements are from the IV column of the periodic table. Other elements in this column, such as carbon, also exhibit semiconductor characteristics [41]. The periodic table, with the elements typically found in semiconductor materials indicated, is shown in Figure 2.10.

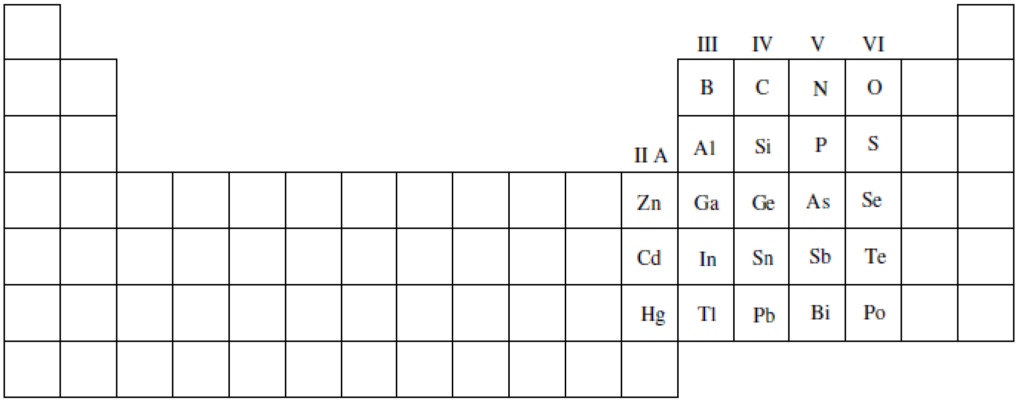

Figure 2.10: The relevant columns of the periodic table to the semiconductor materials discussed here are shown. The naming convention according to column is evident. Elemental semiconductors are Type IV from their column label. The Type III-V compound semiconductors include an element from column III and an element from column V. Type II-VI semiconductors have elements from the II A column and the VI column.

2.2.3.2 Binary

Compounds as well as elements exhibit semiconductor properties. Binary semiconductors are two element compounds usually formed between elements from the III and V columns of the periodic table. In addition, compounds formed from the II and VI columns and two elements from the IV column are also common. These materials are referred to as Type III-V, Type II-VI and Type IV-IV. Combinations of the elements between these columns often have favorable band structure. Type III-V semiconductors include GaAs, InAs, GaSb and InSb. Gallium and Indium are from the III column and Arsenic and Antimony are from the V column. Type II-VI semiconductors include CdTe, ZnTe, CdSe and ZnSe. Cadmium and Zinc are from the II column and Selenium and Tellurium are from the VI column. The common Type IV-IV material is SiGe. Both silicon and germanium are found in the IV column of the periodic table. For both the Type III-V and II-VI semiconductors listed, the elements form a compound in a stoichiometric ratio, one to one, in all the compounds listed. In contrast, SiGe does not form a compound but rather exists as a solid solution across its composition range.

The binary semiconductors that exist as compounds are found in fixed ratios and therefore have fixed physical properties. For semiconductors which exist for a range of compositions, like SiGe, physical properties vary according the ratio between the constituent elements [44].

2.2.3.3 Ternary and Quaternary Materials

Ternary semiconductors are mixtures of three elements. Often these can be considered as a mixture of two binary materials, such as GaAs and InAs. The ratio of Ga and In to As is fixed, but the ratio between Ga and In can vary. This type of material is often described by a pseudo-binary phase diagram where the composition axes reflects the ratio between Ga and In. This material is represented as $Ga_{1-x}In_xAs$, where x represents the ratio between Ga and In. Another important ternary material is $Cd_{1-x}Zn_xTe$. Like SiGe, the physical properties of the semiconductor will vary with the relative ratio between constituents [45].

As an extension of ternaries, quaternary materials can be thought of as mixtures of ternary materials. For example, one quaternary material is AlGaAsSb. This material can be represented as a mixture of AlGaAs and AlGaSb. Both of these ternaries can be considered mixtures of the binary constituents. This allows for further manip-

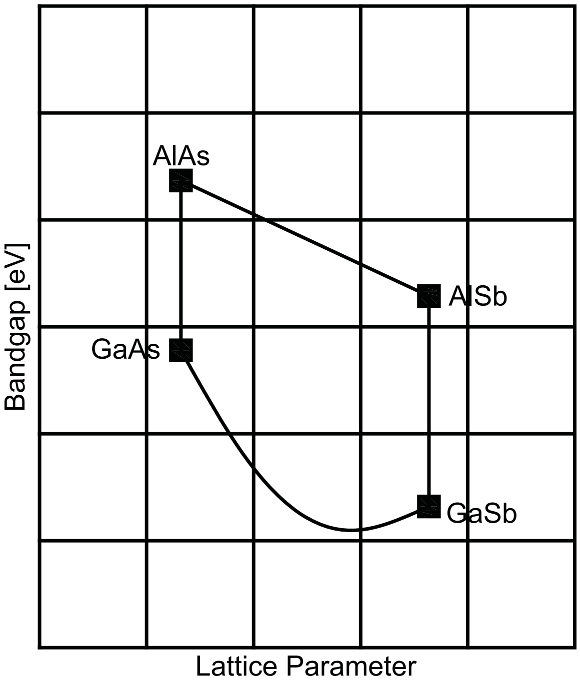

Figure 2.11: The above is an illustration of the quaternary AlGaAsSb system with respect to lattice parameter and bandgap. The material's properties can be varied within the enclosed area by utilizing the quaternary alloy, but not all values may be possible as discontinuities can exist. The edges of the enclosure represent the four ternary systems, AlGaAs, AlGaSb, AlAsSb and GaAsSb.

ulation of the physical properties of the material above what is possible with ternary materials. An illustration of the AlGaAsSb system, in relation to lattice parameter and bandgap, is given in Figure 2.11.

2.2.4 Band Gap Engineering

Using a material with a variable composition allows for manipulation of physical properties across the possible composition range. One property that can be varied is the material's band gap. A material's band gap could be tailored for a particular application by changing its composition. One such example of this could be material for a CCD. The material's band gap can be adjusted such that the highest response is realized for the photon energy of interest. This could allow for production of tuned sensitivity devices [46]. The variation of bandgap with composition in a quaternary system is illustrated in Figure 2.11.

2.2.5 Lattice Matching

Many semiconductor devices consist of multiple layers of differing semiconductor materials. The interfaces between the layers are often areas of high strain as the lattice parameter changes between layers. By varying the composition of the material in a layer, the lattice parameter can be adjusted leading to a less strained interface with the adjacent layers. The variation of lattice parameter with composition in a quaternary system is illustrated in Figure 2.11. Strain will lead to dislocations and other defects that may adversely affect the device's electronic properties [47].

An example of lattice matching can be found in production of HgCdTe infrared detectors. Producing a thick HgCdTe wafer is impractical so it is grown epitaxially on a substrate wafer, usually CdTe. There is lattice mismatch between the layer and the substrate leading to strain. Introducing zinc into the substrate, making the substrate the ternary CdZnTe, changes the lattice parameter and leads to more favorable matching between the device layer and the substrate [48].

2.3 Crystal Growth

Crystal growth is the production of crystalline materials. For semiconductor applications, single crystal material with very low defect density is usually the material of choice. Some applications do exist where polycrystalline material is utilized. There are numerous techniques for producing crystalline material. The main categories relevant to semiconductor materials will be presented.

2.3.1 Bulk and Epitaxial Growth

Bulk growth is generally defined as material growth on the millimeter scale. The bulk material grown by these techniques is often used as a substrate for further growth processes. Additional growth processes may deposit device layers onto the substrate. These layers are generally on the sub-millimeter scale in thickness. These layers are often deposited by epitaxial techniques. The techniques of bulk growth will be presented here.

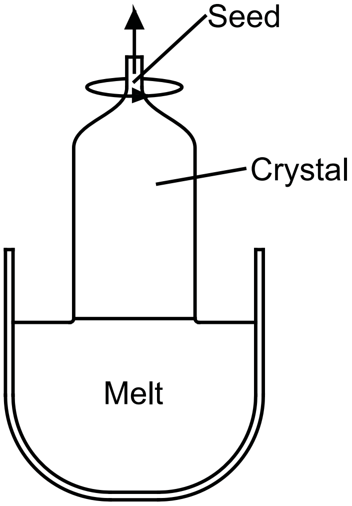

Figure 2.12: The above is an illustration of the Czochralski growth process.

2.3.2 Melt Growth Techniques

Melt growth is the most common and economical way to produce single crystal material. Specifically, the Czochralski method is used to produce most of the semiconductor material used in the device industry. Other important types of melt growth are Bridgman and Vertical Gradient Freeze.

2.3.2.1 Czochralski Method

The Czochralski method is a seeded melt growth technique. A seed of the same or similar material is lowered into a crucible of molten material. The seed is allowed to touch the melt surface and slowly withdrawn. The system is setup such that the top surface of the melt near the middle of the crucible is the coolest point. As the seed is withdrawn, melt is drawn upwards around the seed by surface tension. As the melt is drawn upwards, it further cools and solidifies resulting in additional crystal growth on the seed. An illustration of a typical Czochralski system is shown in Figure 2.12.

The orientation of the grown crystal can be set by the orientation of the seed. Similarly, defects from the seed can carry into the growing crystal. If no seed material is available, then a substitute may be used. If there is mismatch between the seed and the growing crystal material then there will be strain at the interface and this will cause defects in the growing material. Therefore, the quality and supply of seed material is of the utmost concern in this technique [49].

The pull speed of the seed and temperature of the melt can be manipulated to cause the growing crystal to spread out to larger diameters. Those variables can also cause the growing crystal to neck in to smaller diameters.

At the start of a growth process, the growing crystal is often necked in to a very small diameter to trap dislocations, preventing them from propagating from the seed into the growing crystal. The crystal is then necked out to a large diameter for the main growth stage. Current silicon semiconductor processes are usually based on wafers of either $300mm$ or $400mm$ diameters. The final grown crystals are in excess of $100kg$. The grown crystal is never in contact with any crucible wall or other constraint. This removes much of the thermal stress from the grown crystal when compared to a crucible grown crystal [50].

The large diameter possible with Czochralski, along with fast growth rates, make this a very attractive technique for producing bulk material. Growth rates in Czochralski are on the order of $25mm/hr$ for silicon. Thousands of wafers can be produced from a single boule. In addition, on a large diameter wafer more devices can be produced in a production step. Devices are produced side by side on a single wafer then diced up into final package size. A large diameter size allows more devices to be produced in parallel.

As the source material for the technique is melted, the technique has some disadvantages. For silicon, the melt has to be held above silicon's melting point of approximately 1450^oC. The high temperatures required for melt growth can lead to thermal stresses in the grown material. The technique is very successful for single element semiconductors, i.e. silicon and germanium. However, the phase diagrams for compound semiconductors often make melt growth problematic [44].

In the case of a compound semiconductor like GaAs, the compound forms in a one to one stoichiometric ratio. However, the solidus line is not completely vertical at the x=0.5 point on the T-x phase diagram. Instead, the solidus line deviates from vertical and diverges into two lines into both gallium rich and arsenic rich regions. As material is solidified from an x=0.5 melt the grown crystal composition will diverge from stoichiometry according to the solidus line. Melt growth cannot avoid this issue. In addition, there are often volatile components, such as arsenic in this case, that change the composition of the melt as growth proceeds. This can cause composition fluctuations in the growing crystal. For GaAs, these issues are overcome by a variety of techniques and Czochralski is still used as the primary means of production. These techniques include high pressure inert atmosphere over the melt, arsenic overpressure and encapsulating the melt in a material like boron oxide. These add significant cost

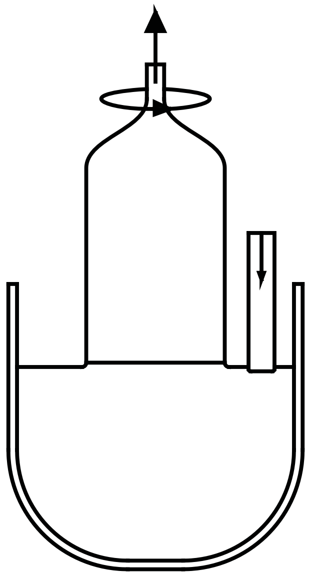

Figure 2.13: The above is an illustration of a variation of Melt-Replenishment Czochralski. Solid bars of feed material are fed into the melt to control composition.

and complexity to the growth process, but the high yield offered by Czochralski still makes the technique attractive [51].

For a compound semiconductor that forms a solid-solution across its composition range like SiGe, it is even more difficult to produce quality material by Czochralski [49]. The separation between the solidus and liquidus lines causes the composition of the melt to change as one constituent is rejected from the solidifying material at the growth interface. The changing melt composition in turn changes the growing crystal's composition. The result is a grown crystal with a graded composition profile. This is very difficult to overcome. Some type of melt replenishment is usually used to compensate for the changes in the melt composition. For silicon germanium, this can involve re-feeding solid silicon into the melt or a double crucible arrangement [27]. The re-feeding of silicon rods is illustrated in Figure 2.13. In a double crucible arrangement, the inner crucible is where growth is taking place and the outer crucible contains a melt reservoir of fixed composition. The melt from the outer crucible is fed into the inner in a controlled manner to compensate for the changing melt composition. This type of arrangement is shown in Figure 2.14.

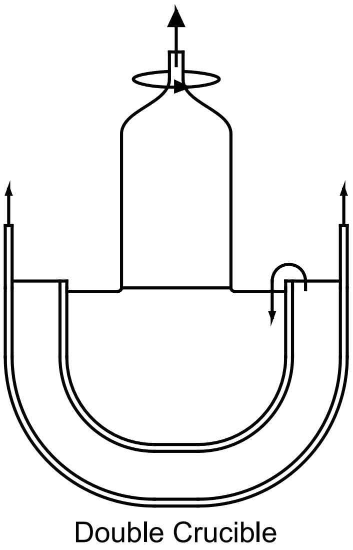

Figure 2.14: The above is an illustration of a double crucible melt replenishment Czochralski growth process. The material in the outer crucible differs in composition from that in the interior crucible. Material is fed from the outer crucible into the inner in order to control melt composition in the inner crucible.

2.3.2.2 Bridgman and Vertical Gradient Freeze Methods

Bridgman and Vertical Gradient Freeze, VGF, methods both operate on a similar principle to Czochralski. In these methods, the melt is contained in a crucible and held in a temperature gradient. The temperature gradient over the crucible is such that one end of the crucible is cool and the opposite end is hot. The gradient is then shifted by some method such that solidification proceeds from the cool end. The temperature gradient continues to move across the crucible and solidification proceeds from one end of the crucible to the other. The method of changing the temperature gradient is what differentiates Bridgman and VGF. In Bridgman growth, the crucible or furnace is translated and the temperature gradient is fixed. In VGF growth, the crucible and the furnace are stationary and the temperature gradient is moved by adjusting the furnace temperature. Both of these techniques can be either seeded or unseeded. In seeded growth, a seed crystal is placed in the crucible at the end where solidification will begin. The grown crystal will pattern off this seed. In unseeded growth, the melt will randomly nucleate onto the crucible wall and growth will proceed from these points. This can often lead to polycrystalline growth. The geometry of the crucible can be optimized to reduce the number of grains in a boule [52]. A typical crucible arrangement is illustrated in Figure 2.15.

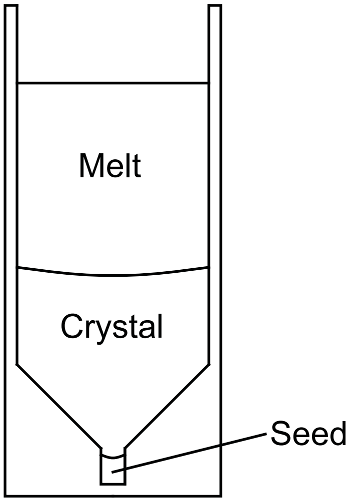

Figure 2.15: The above is an illustration of a typical seeded Bridgman crucible. The material is directionally solidified from the seed end.

Bridgman and VGF suffer from many of the disadvantages present in Czochralski growth. One additional disadvantage is the need to use a crucible to contain the melt. Strain may build up between the grown crystal and the crucible wall. This strain will degrade the material quality. However, it is often easier to control volatile components in these types of growth systems. This technique is often used for production of compound semiconductors such as CdTe and GaAs [53].

2.3.2.3 Float Zone Method

Float Zone is another melt growth technique that does not require a crucible. Rather than melt all the material, a small zone is melted in the middle and this zone is moved through the column of material. Melting takes place at the advancing front of this zone and the crystal is solidified at the trailing edge of the zone. There is no crucible containment for the molten zone, instead surface tension keeps the melt confined. The molten zone is generated by a sharp temperature spike usually produced by an RF heating coil. A typical arrangement for Float Zone is illustrated in Figure 2.16.

The lack of crucible in this technique improves thermal stresses in the grown material. In addition, the constant melting of source material lends this technique to compound semiconductor growth. The composition of the molten zone can be managed by choosing an appropriate composition for the feed material [54, 55].

Like other melt growth techniques, seed material is required for optimal growth. Unlike both Czochralski and Bridgman, using small seeds and growing out to a large

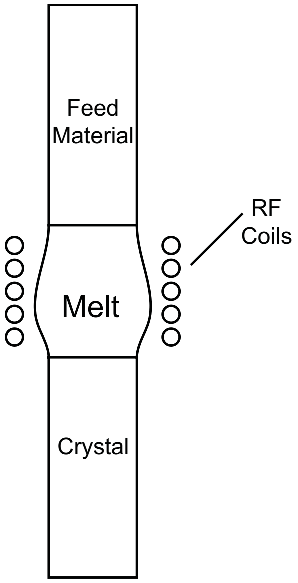

Figure 2.16: The above is an illustration of the Float Zone growth process.

diameter is not easily accomplished in Float Zone. Due to this, large high quality seed material is required.

2.3.3 Solution Growth Techniques

Solution growth techniques generally reduce the high temperatures associated with melt growth and some of the associated problems. They do so by using a solvent to lower melt temperature. Rather than solidifying by cooling across the liquidus line as in melt growth, the solution is forced to super-saturate and precipitation drives solidification. The method of driving the super-saturation varies from technique to technique.

2.3.3.1 Traveling Heater Method

The Traveling Heater Method, THM, moves a solvent zone through a column of material. Dissolution takes place at the advancing side of the solvent zone. This keeps the solvent zone saturated. At the receding side of the solvent zone, material is precipitated out of solution. The solvent zone is isolated in the material by a sharp temperature spike. The presence of solvent lowers the melting point in that region. As the temperature spike is translated relative to the material column, the solvent zone follows the temperature spike. The solution at the growth interface is

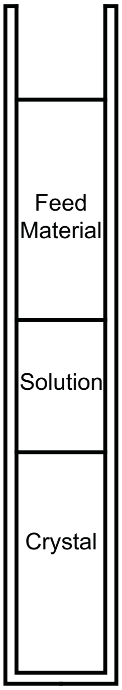

Figure 2.17: The above is an illustration of the THM growth process.

supersaturated by the drop in temperature as the temperature spike moves. A typical THM arrangement is illustrated in Figure 2.17.

CdTe is a material that is currently produced commercially by the THM method. CdTe is difficult to produce by melt growth techniques as the constituents both readily evaporate at high temperatures. In addition, the defects in CdTe have low energies of formation. Therefore the additional thermal stresses incurred during melt growth can significantly degrade material quality. THM has a significantly lower yield than melt growth techniques. The value of CdTe material offsets the downsides of the technique, which is why it is commercially produced this way [56].

Single crystal THM growth requires a seed crystal to initiate growth. Also, the material is grown in a crucible, which leads to additional stresses between the material and the walls. The growth rates for THM are significantly lower than melt growth techniques, on the order of millimeters per day. Due to the temperature spike required, the diameter of the crucible is limited. Large diameter crucibles would require a thicker solvent zone resulting in slower transport of material from the dissolution to growth interfaces along with a host of other issues. A large diameter THM crucible is on the order of $50mm$.

2.3.3.2 Liquid Phase Epitaxy

Liquid phase epitaxy, LPE, is another common solution growth technique. In this method, the solution is saturated away from the seed. Once saturated, the solution is introduced to the seed crystal. The temperature is lowered and the solution precipitates onto the seed crystal. The layer produced is relatively thin, on order of a few millimeters maximum. It is often used to produce thick device layers. By saturating the solution away from the seed, melt back of the seed is reduced or eliminated.

A variant of this technique is liquid phase electro-epitaxy. This technique uses an electric current to drive the superaturation at the seed rather than a temperature drop. In addition, the solution does not deplete of solute as it is in contact with source material where dissolution can take place. This method has a very low yield similar to LPE but is technically more difficult [57].

2.3.3.3 Liquid Phase Diffusion

Liquid Phase Diffusion, LPD, was the solution growth technique that was used for experiments in this work. In this technique, a graded composition crystal is produced. For silicon germanium growth, the solvent and the seed material are the same. The source material contains the solute. The initial system material arrangement is the seed separated from the source by a solvent zone. This is achieved by applying a steep temperature gradient across the materials. The seed-solvent interface is formed on the isotherm corresponding to the melting temperature of the seed. The dissolution interface is at a higher temperature than the seed interface. The solvent dissolves the source and the dissolved solute is mixed into the solvent. The saturation concentration of the solution is higher at the dissolution interface than it is at the seed interface. As solute is mixed towards the seed interface it saturates then supersaturates the solvent adjacent to the interface. Material is precipitated with a composition determined by the temperature at which solidification took place. This temperature varies during growth due to the applied temperature gradient. Each layer's composition will gradually vary as growth proceeds [36–38]. The growth conditions and crucible arrangement are illustrated in Figure 2.18.

In SiGe growth by LPD, a germanium seed and a silicon source is used. The silicon is transported in a diffusion dominated manner to the growth interface. This makes growth very slow and the composition varies with the solidus line of the SiGe T-x phase diagram and the applied temperature gradient. The application for this

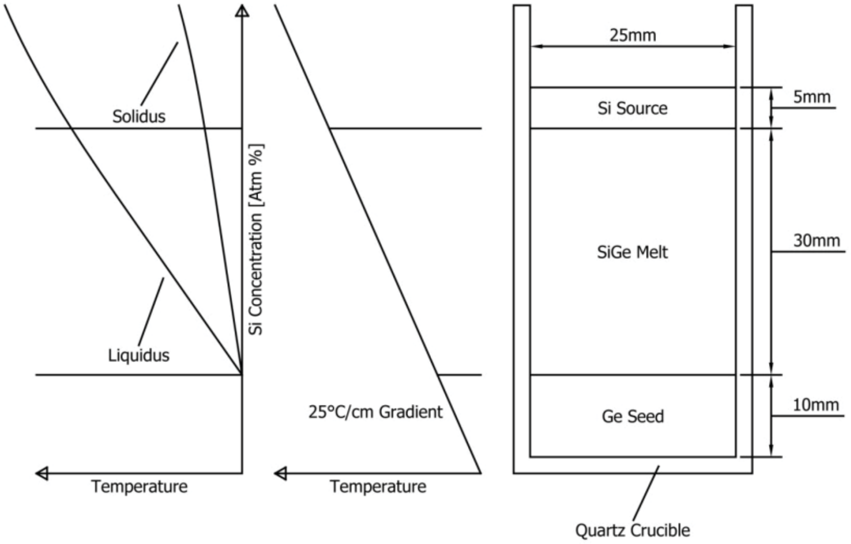

Figure 2.18: The above is an illustration of the SiGe LPD growth process. The temperature gradient and phase diagram are shown to illustrate the process. At the dissolution interface, the temperature is higher and the liquidus is at a greater Si composition than the solidification interface. The composition variation drives diffusion of Si towards the solidification interface. At the cooler temperature of the solidification interface, the melt is constitutionally super-cooled and solidification takes place.

type growth would be to use the resulting bulk material to extract wafers at various compositions of interest. Then subsequently use the wafers as seeds in further growth processes. Often obtaining reliable seeds for growth techniques is a major issue. This is true for silicon germanium. Czochalski growth techniques often use germanium or silicon seed material. This results in additional strain in the crystal due to the lattice mismatch [58, 59]. The strain is minimized in LPD crystals as the composition varies gradually and smoothly through the material.

2.3.4 Vapor Phase Growth Techniques

Vapor phase techniques are also utilized for bulk growth. Typically these techniques have lower yields than solution growth techniques and slower growth rates. However, they do offer the advantage of high quality growth of materials that are difficult to produce by other techniques. For example, vapor phase techniques have been examined for producing seeds for CdTe production. For both THM and Bridgman growth of CdTe, a seed is required for optimal material quality. Obtaining good seeds is often difficult. Currently, they are often mined out of polycrystalline boules from unseeded Bridgman growth. This results in significant defect density in the seed. Using a physical vapor transport technique would allow the production of high quality seed material. This type of technique is unlikely to become a viable bulk growth technique on its own, but like LPD, could be valuable for producing seed material.

2.3.5 Applied Magnetic Fields in Crystal Growth

The flow field in the melt profoundly effects the quality of the growing crystal. Strong flow can lead to interface breakdown trapping impurities. Weak flow can lead to a lack of mixing, resulting in the buildup of rejected constituents at the growth interface and very slow growth rates. Control of the mixing in the melt can be achieved to some extent through system geometry and temperature profile. To achieve further control of the mixing in the melt, magnetic fields are often utilized. The electrically conductive semiconductor melt experiences a Lorentz force in the presence of a magnetic field.

Static magnetic fields can be used to suppress the formation of convective cells in the melt. The Lorentz force disrupts the flow in the cell preventing strong convection [60]. Rotating magnetic fields can be used to add additional mixing into the melt. Other types of time varying fields also cause additional mixing in the melt. These include travelling and alternating magnetic fields [61].

2.4 Silicon Germanium

As previously discussed, silicon and germanium are both elemental semiconductors. As a compound, they form a solid solution across their composition range. This allows for variation of the material's physical properties to suit various use cases.

2.4.1 Applications

Silicon germanium has numerous applications. Epitaxial device layers are used to produce high performance discrete devices, heterojunction devices, optoelectronic components and photodetectors [2, 3, 5–7, 10, 62, 63]. In many cases, a SiGe layer is grown on a Si substrate. The resulting layer is strained due to the lattice mismatch with the substrate [17,64]. The strain in the layer changes the electronic properties of the material and requires that the device be engineered around the strained properties. The advantage of using a layer is that the SiGe structure can be integrated onto silicon wafers. In optoelectronics, the SiGe acts as the receiver and transmitter of the optical signal [12, 13]. Standard silicon structures can be printed on the same chip for additional signal processing. This type of system on a chip is also utilized for IR detection. A SiGe layer for radiation detection and standard silicon readout circuitry is contained on the same chip [14, 15].

Heterojunction devices are the most common use for SiGe device layers. The heterojunction device takes advantage of the increased mobility found in SiGe to improve switching performance [19, 20]. This property has made this type of device very useful in production of high frequency electronics such as those found in Telecom applications [8, 9, 18].

The applications discussed so far have involved SiGe layers on a Si substrate. As there is no economical source of SiGe substrate material, significant work has been focused on producing high quality devices on Si substrates. Despite the success in producing SiGe structures on Si, the strain induced in the layers does limit the performance and application of devices [2, 8, 9].

Bulk SiGe across its composition range would have application as a substrate for epitaxy. Producing SiGe device layers on a SiGe substrate would offer different material capabilities to the SiGe device layers in use today. In addition to SiGe and Si device layers, a SiGe substrate can be lattice matched to III-V semiconductor device layers such as GaAs [3, 21]. This would allow the integration of III-V device layers into Si based devices. The lattice parameter of SiGe varies almost linearly with composition between the value for Si and the value for Ge [17].

SiGe is sensitive to a range of radiation in the IR region, approximately 1.3μm to 20μm [12, 13]. This property has lead to the material finding use as a solar cell material and an infrared detector [46]. In solar cell technology, bulk SiGe can be used as a substrate for other solar cell materials. Specifically, the SiGe substrate can be lattice matched to GaAs and a GaAs solar cell structure grown [3,21]. Currently, this type of cell is built on Ge substrates. The lattice mismatch between the GaAs and Ge requires a buffer layer to be grown to distribute the strain. The use of the SiGe substrate is desirable as it enhances the efficiency of the GaAs device. This is due to its sensitivity in the infrared regime and carrier multiplication phenomena [65, 66].

SiGe is also proposed as a material for high energy photon detection [3, 67, 68].

Current Ge based detectors for X-Rays require cryogenic temperatures due to the material's small band gap. Si possesses a more favorable band structure for this type of detector. However, the atomic number of silicon is much lower than germanium. The detection efficiency is proportional to the atomic number. So Si can operate at higher temperatures but is less efficient while germanium is efficient but requires low temperature. The band structure of silicon germanium varies with composition relatively smoothly with one discontinuity where the structure changes from Si-like to Ge-like [2]. By using a SiGe alloy, it has been proposed that high efficiency X-Ray detectors can be produced that operate at higher temperatures, than Ge based detectors.

Other applications of SiGe include optical materials. For both X-Ray regime and IR regime optics, graded silicon germanium crystal optics has been proposed. Varying the composition of the material allows for tuning of the optical properties [65, 69].

An early use of polycrystalline SiGe was as a thermoelectric material. The material has been found to efficiently convert thermal energy into electric energy. SiGe based power sources have been used on numerous NASA satellite missions converting heat from radioactivity into electricity [3, 70–73].

2.4.2 Transport Properties

SiGe forms a solid solution across its composition range. There is a large separation between the solidus and liquidus lines [16, 74]. This is evident in the phase diagram, which is shown in Figure 2.19. This separation is a major issue when synthesizing the highly uniform material required for semiconductor applications [75]. The composition in the grown crystal will tend to vary as the rejected constituent, germanium, builds up at the growth interface. This is illustrated in Figure 2.20. The transport of silicon into the growth interface is of utmost concern in ensuring the composition of the growing crystal stays constant. The rejection of germanium from the solidification interface will cause the melt to become dilute in silicon. Feeding silicon into the melt can overcome this but detailed understanding of how the introduced silicon will mix into the bulk melt is required.

Values for the physical properties of SiGe melts are not well documented. The high temperatures involved with these types of studies along with the full composition range have kept the system from being fully explored.

Focusing on the properties related to melt and solution growth, the SiGe system

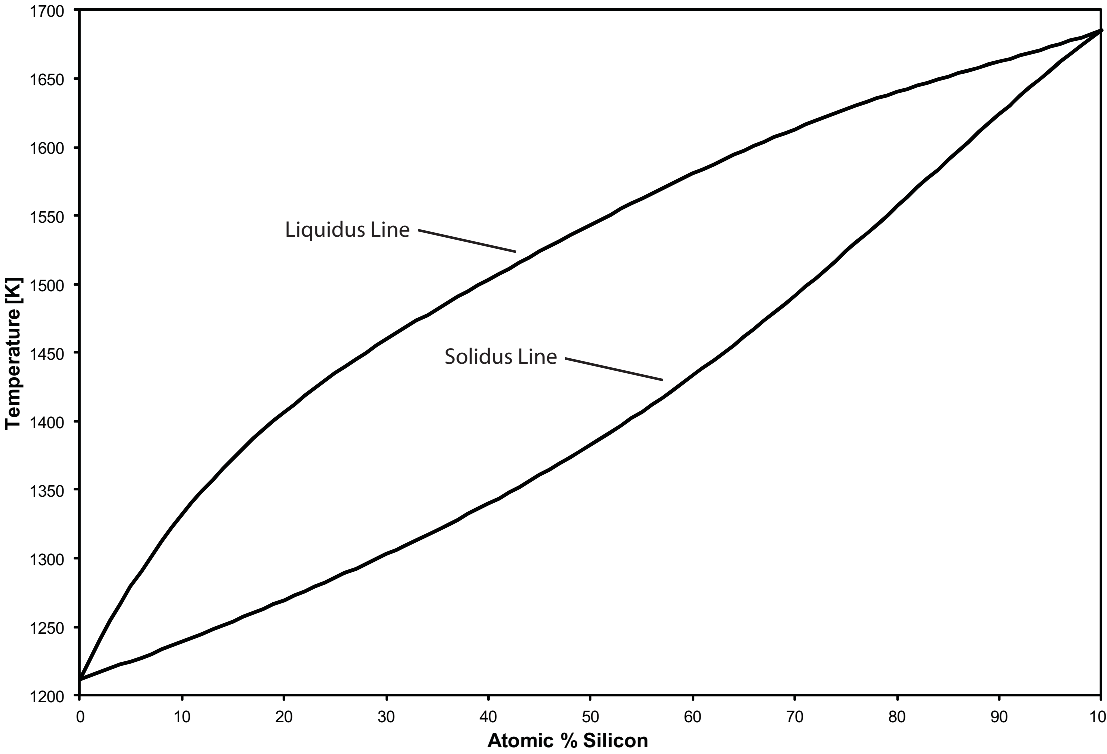

Figure 2.19: The figure above is a digitization of the SiGe phase diagram [74]. The wide separation between the solidus and liquidus lines is visible.

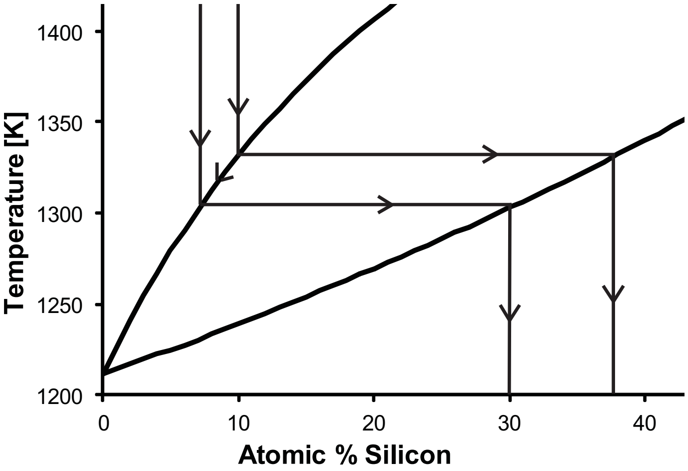

Figure 2.20: The diagram above illustrates the rejection of germanium into the melt during solidification. The solid is at a higher Si concentration than the liquid, so silicon is preferentially consumed during solidification. This changes the melt composition towards the Ge-rich side and the next layer will be solidified from a different liquid composition and therefore have a different solid composition.

possesses some interesting features. First, there is a wide gap between the densities of the two constituents. Silicon is a much lighter material, $2.53 g/cm^3$ at melting, than germanium, $5.59 g/cm^3$ at melting [53, 76]. At 300K the material density varies according to $2.329 + 3.593x - 0.499x^2$, where x is atomic % Ge [51]. A similar function will exist for the melt at growth temperatures. A fluid element containing a higher silicon composition will experience a buoyancy force in the presence of fluid elements with lower silicon content. The solutal expansion coefficient of SiGe is reported as 5.3×10^{-3} per atomic % Si [25]. This is a significant effect in SiGe melts. Additionally, SiGe melt has a thermal expansion coefficient reported as $1.2 \times 10^{-4}\ 1/K$ [25]. Both thermal and solutal driven convective flows can be strong transport mechanisms in the melt. However, the buoyancy of the silicon can also have a stabilizing effect on the melt. The solutal buoyancy force can stabilize the fluid against thermal driven convection. This can make the transport mechanism in the melt effectively diffusion dominated [25].

The diffusion coefficient in SiGe is reported in the range of 1 to $3 \times 10^{-8}\ m^2/s$ [25, 58, 77]. This value is not well investigated or available in current literature. Given that some processes can proceed diffusion dominated, better information on the diffusion process of Si in Ge melts is needed to optimize growth conditions.

2.4.3 Crystal Growth

SiGe has been grown by numerous techniques with varying levels of success. The melt growth techniques have seen the most focus as they provide the most practical path to commercialization. Solution growth techniques have also been explored.

2.4.3.1 Czochralski

Czochralski grown SiGe crystals have been produced across the entire composition range. Conventional Czochralski has been used to produce graded composition material [4, 78–83]. To correct the composition variation, a method to control the composition of the melt is required. One method is to re-feed silicon into the melt. As germanium is rejected back into the melt at the growth interface, solid silicon is fed into the melt to keep the melt composition constant. Another group of melt replenishment techniques are the double crucible methods [27]. The inner and outer crucibles contain melts of differing compositions. The crystal is pulled from the inner crucible and material from the outer crucible can be fed into the inner crucible to control composition.

The success of melt replenishment methods is determined by the mixing and transport of the constituents in the melt. Specifically, the germanium rejected at the interface and the silicon being replenished must both mix quickly back into the melt to keep the material solidifying at a constant composition. This type of fast mixing could be accomplished with strong convective flow. However, strong flow around the growth interface will degrade the growth interface and result in unfavorable growth conditions. Therefore a delicate balance must be struck to achieve optimal growth. Melt replenishment techniques currently show compositional variations in grown crystals due to these issues [27].

The availability of SiGe seeds also affects the melt growth techniques. Most studies on Czochralski use Si seeds, for entire SiGe composition range. Some studies use Ge seeds for Ge-rich SiGe growth. The use of matched SiGe seeds is limited as it is difficult to produce material for seed stock [58, 59]. It has been noted that the use of Si and Ge seeds cause a high density of dislocations at the seed-crystal interface due to the lattice mismatch [58]. In addition, the grown material can often transition to polycrystalline growth [84, 85].

2.4.3.2 Bridgman

Bridgman has been used to a lesser extent to produce SiGe [85, 86]. The Bridgman technique suffers from many of the problems of the Czochralski technique. In addition, there is the strain from the contact of the grown crystal with the crucible. In the Bridgman technique, it is also more difficult to institute a melt replenishment system. This makes overcoming the variation of melt composition an even harder task than for Czochralski.

2.4.3.3 Float Zone

The Float Zone technique is a promising candidate for the production of SiGe [87,88]. The melt is being continuously fed by new feed material as the melt zone moves. The feed material can be SiGe of the same composition as that being grown [54]. In this case, when the solidification and melting interface velocities are the same, the melt composition should remain constant. This would eliminate compositional variations in the grown crystal.

The same issues surrounding seed material for Czochralski also apply for Float

Zone. Experiments often utilize Si or Ge seed material [54, 55]. An additional issue for Float Zone is that the seed material is typically the same diameter as the material being grown. For bulk production, large diameter seed crystals would be required. In Czochralski growth, small diameter seeds can be used as the growing crystal can be necked out to a much larger diameter than the seed diameter.

2.4.3.4 Solution Growth

For solution growth techniques, Liquid Phase Diffusion and Zone Melting have been used to produce SiGe [36–38, 89–92]. Zone Melting is a very similar technique to Liquid Phase Diffusion. Both have produced graded single crystal material. In addition, Zone Melting has been used to produce constant composition material by translating the growth interface to maintain a constant temperature. In the LPD and Zone Melting techniques, the composition of the growing material is determined by the temperature at the growth interface. Both of these techniques are limited by their growth rates as the transport is diffusion dominated. In addition, only small diameter, $25mm$ and under, material has been produced.

2.5 Modeling Crystal Growth Processes

The modeling of growth processes is a very important topic in crystal growth. Crystal growth processes are inherently expensive, time consuming and, due to high temperatures and other factors, often unavailable for in-situ observation. The optimization of a crystal growth process often involves numerous variables. The number of variables involved is often too many to reasonably investigate experimentally. In addition, the cause of experimentally observed phenomena is often not readily apparent from the physical results. Due to these factors, numerical modeling techniques are applied to crystal growth methods for optimization and greater understanding of the transport mechanisms at work. Continuum models for crystal growth processes are well studied and have been show to produce agreement with physical results.

2.5.1 Continuum Model for Binary Crystal Growth

Modeling of the crystal growth system is not the main topic of this work and will only be presented in brief in this section.

2.5.1.1 Balance Laws

The balance laws are presented in detail in many sources and their derivation will not be covered. Presented below are the local balance equations for a multiple component continuous material on both a discontinuity surface and a control volume [93].

Conservation of Mass for α Constituent

$$\rho\left(\frac{\partial c^\alpha}{\partial t} + c^\alpha_{,k} v_k\right) + \bar{i}^\alpha_{k,k} = \hat{r}^\alpha \qquad \text{in } V_{-\sigma} \tag{2.1}$$

$$\|\rho c^\alpha (v_k - u_k) + \bar{i}^\alpha_k\|\, n_k = \hat{s}^\alpha \qquad \text{on } \sigma \tag{2.2}$$

Conservation of Mass for Mixture

$$\frac{\partial \rho}{\partial t} + (\rho v_k)_{,k} = 0 \qquad \text{in } V_{-\sigma} \tag{2.3}$$

$$\|\rho(v_k - u_k)\|\, n_k = 0 \qquad \text{on } \sigma \tag{2.4}$$

Balance of Momentum

$$\rho \dot{v}_l = t_{kl,k} + \rho b_l + f^{em}_l \qquad \text{in } V_{-\sigma} \tag{2.5}$$

$$\|\rho v_l (v_k - u_k) - t_{kl} + t^{em}_{kl}\|\, n_k = \nabla_{sl}\gamma^\sigma + 2\gamma^\sigma \Omega n_l \qquad \text{on } \sigma \tag{2.6}$$

Balance of Energy

$$\rho \dot{\epsilon} = t_{kl} v_{l,k} + q_{k,k} + \rho h + \sum_{\alpha=1}^{N} \rho^\alpha b^\alpha_l \bar{v}^\alpha_l + J_k E_k \qquad \text{in } V_{-\sigma} \tag{2.7}$$

$$\left\| \frac{1}{2}\left(\rho(v_l v_l + \epsilon) + (E^2 + B^2) + \sum_{\alpha=1}^{N} (c^\alpha \bar{v}^\alpha_l \bar{v}^\alpha_l)\right)(v_k - u_k) - q_k - (t_{kl} + t^{em}_{kl}) v_l \right\| n_k = \gamma^\sigma v^\sigma_l 2\Omega n_l \qquad \text{on } \sigma \tag{2.8}$$

Entropy Inequality

$$-\rho(\dot{\Phi} + \eta\dot{\Theta}) + \left(\sum_{\alpha=1}^{N} \mu^\alpha \bar{i}^\alpha_k\right)_{,k} + \frac{1}{\Theta}\left(q_k - \sum_{\alpha=1}^{N} \mu^\alpha \bar{i}^\alpha_k\right)\Theta_{,k} + t_{kl} v_{l,k} + J_k E_k \geq 0 \tag{2.9}$$

Table 2.1: Balance Equation Nomenclature

V	Fluid volume
σ	Discontinuity surface
v	Fluid velocity
u	Discontinuity surface velocity
c^α	Mass Concentration of α Constituent
$\bar{i}^\alpha$	Mass Flux term for α Constituent
$\hat{r}^\alpha$	Mass Source term for α Constituent
n	Unit normal to discontinuity surface
t	Stress tensor
b	Body force term
f^{em}	Electromagnetic body force term
t^{em}	Maxwell stress tensor
γ^σ	Thermodynamic surface tension
Ω	Mean curvature
$\dot{\epsilon}$	Internal energy density
q	Energy flux
h	Energy source term
J	Current density
E	Electric field
B	Magnetic field
Φ	Helmholtz free energy function
η	Entropy
Θ	Temperature
μ	Chemical potential

2.5.1.2 Field Equations for the Simulations

The governing equations for the numerical work presented here are given below. These equations are subject to the following assumptions.

The liquid domains modeled are approximated as binary mixtures of heat and electrical conducting Newtonian fluids. Additionally, Fick's law for mass flux and Fourier's law for heat conduction are utilized as constitutive equations. The Boussinesq approximation for inclusion of the gravitational body force is assumed valid. In addition to the thermal buoyancy force, a solutal buoyancy force is also included in the Bousinesq approximation. The Soret and Dufour effects are neglected as there is no evidence of their significance in the growth process being considered. The solid domains are assumed to be rigid heat conducting solids and therefore only the energy balance is considered.

Under these assumptions, the field equations take the following familiar form. The magnetic field body force terms will be considered in the following section. The gravitational acceleration vector is taken to be aligned with the z-axis.

Liquid Phase (in cylindical coordinates):

Continuity

$$\frac{1}{r}\frac{\partial}{\partial r}(ru) + \frac{1}{r}\frac{\partial v}{\partial \varphi} + \frac{\partial w}{\partial z} = 0 \tag{2.10}$$

Momentum

$$\frac{\partial u}{\partial t} + u\frac{\partial u}{\partial r} + \frac{v}{r}\frac{\partial u}{\partial \varphi} + w\frac{\partial u}{\partial z} - \frac{v^2}{r} = -\frac{1}{\rho_L}\frac{\partial p}{\partial r} + \nu\left(\nabla^2 u - \frac{u}{r^2} - \frac{2}{r^2}\frac{\partial v}{\partial \varphi}\right) + \frac{f_r^{em}}{\rho_L} \tag{2.11}$$

$$\frac{\partial v}{\partial t} + u\frac{\partial v}{\partial r} + \frac{v}{r}\frac{\partial v}{\partial \varphi} + w\frac{\partial v}{\partial z} - \frac{uv}{r} = -\frac{1}{r\rho_L}\frac{\partial p}{\partial \varphi} + \nu\left(\nabla^2 v - \frac{v}{r^2} - \frac{2}{r^2}\frac{\partial u}{\partial \varphi}\right) + \frac{f_\varphi^{em}}{\rho_L} \tag{2.12}$$

$$\frac{\partial w}{\partial t} + u\frac{\partial w}{\partial r} + \frac{v}{r}\frac{\partial w}{\partial \varphi} + w\frac{\partial w}{\partial z} = -\frac{1}{\rho_L}\frac{\partial p}{\partial z} + \nu\nabla^2 w + \beta_T(T - T_0)g + \beta_C(C - C_0)g + \frac{f_z^{em}}{\rho_L} \tag{2.13}$$

Energy

$$\frac{\partial T}{\partial t} + u\frac{\partial T}{\partial r} + \frac{v}{r}\frac{\partial T}{\partial \varphi} + w\frac{\partial T}{\partial z} = \frac{k_L}{\rho_L \gamma_L}\nabla^2 T \tag{2.14}$$

Mass Transport

$$\frac{\partial C}{\partial t} + u\frac{\partial C}{\partial r} + \frac{v}{r}\frac{\partial C}{\partial \varphi} + w\frac{\partial C}{\partial z} = D_C \nabla^2 C \tag{2.15}$$

Solid Phase (in cylindical coordinates):

Energy

$$\frac{\partial T}{\partial t} = \frac{k_S}{\rho_S \gamma_S}\nabla^2 T \tag{2.16}$$

Typical Dissolution Interface Condition (in cylindrical coordinates):

Table 2.2: Field Equation Nomenclature

$u,\ v,\ w$	Velocity components
ρ_L	Liquid phase density
ν	Viscosity
$f_r^{em},\ f_\varphi^{em},\ f_z^{em}$	Magnetic field body force components
β_T	Coefficient of thermal expansion
T	Temperature
T_0	Reference temperature
β_C	Coefficient of solutal expansion
C	Concentration
C_0	Reference concentration
k_L	Liquid phase thermal conductivity
γ_L	Liquid phase specific heat
D_C	Diffusion coefficient
ρ_S	Solid phase density
k_S	Solid phase thermal conductivity
γ_S	Solid phase specific heat

Continuity

The dissolution is considered small and as such the mass balance equation at the interface is excluded.

Momentum

No slip condition is implemented.

$$u = v = w = 0 \tag{2.17}$$

Energy

The heat flux is considered continuous at the interface. Latent heat is considered to dissipate without disturbing the the continuity due to the slow rate of dissolution. n is normal to the interface.

$$k_S \frac{\partial T_S}{\partial n} - k_L \frac{\partial T_L}{\partial n} = 0 \tag{2.18}$$

Mass Transport

$C_{equilibrium}$ determined from phase diagram.

$$C = C_{equilibrium} \tag{2.19}$$

2.5.1.3 Magnetic Fields

The Lorentz force for a metallic liquid solution that is non-magnetizable and non-polarizable is given below:

$$\mathbf{F}^{em} = \mathbf{J} \times \mathbf{B} = \sigma_E \left(\mathbf{E} + \mathbf{v} \times \mathbf{B} \right) \times \mathbf{B} \tag{2.20}$$

The electric field term can be considered in two parts. First any applied electric fields need to be included. Second, electric fields induced by the applied magnetic field are included. In application to SiGe growth systems, the contribution of the induced field has been shown to be insignificant [93]. There are also no applied electric fields considered in this work, so the electrical field term is neglected. With this approximation, the body forces take the form of the following equations.

$$\begin{aligned} f_1^{em} &= \sigma_E(B_2 v + B_3 w)B_1 - \sigma_E(B_2^2 + B_3^2)u \\ f_2^{em} &= \sigma_E(B_1 u + B_3 w)B_2 - \sigma_E(B_1^2 + B_3^2)v \\ f_3^{em} &= \sigma_E(B_1 u + B_2 v)B_3 - \sigma_E(B_1^2 + B_2^2)w \end{aligned} \tag{2.21}$$

For a static magnetic field acting in the z direction only, the following body forces are generated in cylindrical coordinates.

$$\begin{aligned} f_r^{em} &= \sigma_E B_z^2 u \\ f_\varphi^{em} &= \sigma_E B_z^2 v \\ f_z^{em} &= 0 \end{aligned} \tag{2.22}$$

For a rotating magnetic field, with the axis of rotation as the z-axis, the following assumptions lead to a simplified body force. The material is assumed to rotate at a much lower velocity than the frequency of the applied field. This is a good approximation considering the inertia and viscosity of the fluid. This allows the removal of the time dependant forces on the fluid elements and thus the elimination of the radial and axial components. In addition, the magnetic field is assumed to be continuous and the boundaries of the fluid are considered as electrical insulators. It has been shown that this set of assumptions only result in an approximate 3% error. The advantage is a considerably simpler body force that can be integrated into the momentum balance equation without having to solve for the electric potential [94–96]. An illustration of

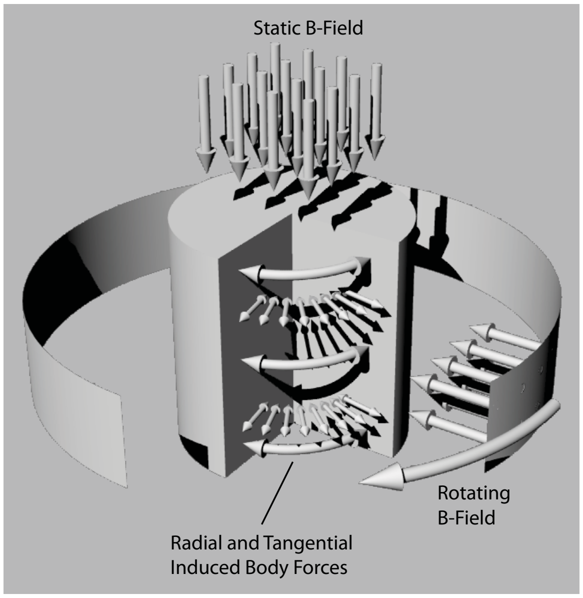

Figure 2.21: The above is a sketch of the applied magnetic fields and the induced body forces. The center cylinder with the cutaway represents the melt zone. The rotating magnetic field rotates around the vertical axis and the static field is aligned with the vertical axis.

the applied fields and their body forces is shown in Figure 2.21.

$$\begin{aligned} f_r^{em} &= 0 \\ f_\varphi^{em} &= \frac{1}{2}\sigma_E r \omega B_{RMF}^2 \\ f_z^{em} &= 0 \end{aligned} \tag{2.23}$$

Table 2.3: Magnetic Body Force Equation Nomenclature

$u,\ v,\ w$	Velocity components
σ_E	Conductivity
ω	Frequency of the rotating magnetic field
$f_r^{em},\ f_\varphi^{em},\ f_z^{em}$	Magnetic field body force components

2.5.2 Dimensionless Analysis

When the field equations are nondimensionalized, the dimensionless parameters of the field equations offer insight into the processes taking place. The most widely recognized parameter is the Reynolds number, which classifies the flow as turbulent or laminar. The parameters are computed, with values typical for the system, in order to qualitatively grasp the importance of various effects in the melt. The dimensionless parameters relevant to the model discussed in this work are presented following.

Table 2.4: Relevant Dimensionless Parameters

Symbol	**Name**	**Definition**
Re	Reynolds Number	Ratio of inertial to viscous forces.
Pr	Prandtl Number	Ratio of momentum diffusivity to thermal diffusivity.
Sc	Schmidt Number	Ratio of momentum diffusivity to solutal diffusivity.
Gr_T	Thermal Grashof Number	Ratio of buoyancy force to viscous force.
Gr_C	Solutal Grashof Number	Ratio of buoyancy force to viscous force.
Ha	Hartmann Number	Ratio of magnetic body force to viscous force.
Ta_B	Magnetic Taylor Number	Ratio of rotational inertial force to viscous force.
Re_B	Magnetic Reynolds Number	Ratio of fluid flux to magnetic diffusivity.

Table 2.5: Dimensionless Parameter Values

Name	**Formula**	**Value**	**Result**
Reynolds Number	$Re = vL/\nu$	≈ 5	Flow is in the laminar regime.
Prandtl Number	$Pr = \nu/\kappa$	$\approx 5 \times 10^{-3}$	Thermal transport is primarily by conduction. κ is the thermal diffusivity.
Schmidt Number	$Sc = \nu/D$	≈ 5	Convective and diffusive mass transport will both figure in the melt.
Thermal Grashof Number	$Gr_T = g\beta_T \Delta T L^3/\nu^2$	$\approx 1 \times 10^8$	Thermal convective flow is significant.
Solutal Grashof Number	$Gr_C = g\beta_C \Delta C L^3/\nu^2$	$\approx 1 \times 10^7$	Solutal convective flow is significant.
Hartmann Number	$Ha = B_{st} L\sqrt{\sigma_L/\rho\nu}$	$\approx 1 \times 10^3$	The static field magnetic body force is significant, but not very high compared to viscous forces.
Magnetic Taylor Number	$Ta_B = \sigma_L B_{rot}^2 \omega_B L^4/2\rho\nu^2$	$\approx 1 \times 10^8$	The rotating magnetic field body force is high compared to viscous forces.
Magnetic Reynolds Number	$Re_B = vL/\eta$	$\approx 5 \times 10^{-6}$	The flow in the melt does not appreciable effect the magnetic field. η is the magnetic diffusivity.

2.5.3 Numerical Solutions

Finite volume numerical techniques and finite element numerical techniques have both been utilized with success for modeling growth processes. In this study, both techniques were employed in modeling the transport processes. The two methods differ in their method of discretizing the fluid balance equations [97]. The finite volume formulation ensures conservation of the variable on the control volume and therefore the entire volume. More care is needed in the finite element method to ensure this conservation. However, the finite element formulation has been shown to be more stable in many applications [98, 99].

Other considerations such as geometry can play a role in the technique used. In this study, the crucible geometry was very simple but the melt is subject to high body forces. The high body forces make the numerical stability of the technique a priority. Solutions were obtained with finite volume and finite element methods for comparison.

In the numerical work completed by the author, the ANSYS CFX commercial software package was utilized. This is a finite volume based solver. Convergence of the simulations with high body forces proved problematic. Simulations were also prepared by a collaborator using the OpenFOAM open source software package, another finite volume based solver. In this work, the software was optimized to handle the body forces in the melt. Good numerical stability was achieved but some physical phenomena were not resolved. Finally, simulations were prepared by a collaborator using the finite element solver COMSOL. Again good convergence and stability was achieved.

Table 2.6: Physical Properties of the SiGe LPD System [25, 51, 53, 58, 76, 77, 99–101]

Property	**Si Source** (Solid)	**Ge Seed** (Solid)	**$\mathbf{Si_xGe_{1\text{-}x}}$ Melt** (Liquid)
Specific Heat $\gamma[J/kgK]$	967 at 1300K	967 at 1210K	$380 - 406$
Thermal Conductivity $k[W/mK]$	23.7 at 1273K	10.60 at 1210K	42.5
Mass Diffusivity $D[m^2/s]$			$1 - 3 \times 10^{-8}$
Mass Density $\rho[kg/m^3]$	2301.6 at 1300K	5323 at 1210K	5633
Thermal Expansion $\beta_T[1/K]$			1.2×10^{-4}
Solutal Expansion β_C[1/atm % Si]			5.3×10^{-3}
Viscosity $\mu[kg/ms]$			7.35×10^{-4}
Conductivity $\sigma[1/\Omega m]$	4.25×10^4	6.06×10^5	1.7×10^6

Chapter 3

Silicon Dissolution Processes

3.1 Introduction

In the LPD process, it is the dissolution of silicon into the melt and its subsequent transport to the growth interface that determines the growth rate. The first part of the process, the dissolution of silicon, is the process that is isolated from the rest of the LPD system for study here. The rate of dissolution into the germanium melt will be related to the transport of the silicon species in the melt.

3.2 Experimental Design

To examine the dissolution process a set of experiments were designed to study the process. An isothermal system was used to limit the transport mechanisms in the melt to diffusion. The dissolution of silicon into the melt and its subsequent transport away from the dissolution interface should be dominated by diffusion. The thermal convective transport will be minimized in an isothermal system. Solutal convection will still be present in the melt. No growth of material will take place in these experiments. Instead a solid silicon source is allowed to dissolve into the melt for a given amount of time.

The amount of silicon dissolved will be proportional to the strength of the mass transport in the melt. The dissolution process will slow as silicon enters the melt and the concentration gradient around the interface decreases. The driving factor in diffusion is the concentration gradient. Therefore as the melt gains in silicon concentration the rate of mass transport will slow. The time of the experiments

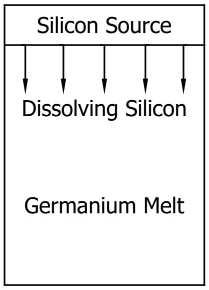

Figure 3.1: Shown above is a schematic of the experimental material layout with the dissolution interface at the top of the melt. The dissolving silicon is transported downwards away from the interface.

is kept short such that the concentration of silicon does not rise to a point where dissolution will have significantly slowed due to saturation of the melt.

The solutal convection in the melt will continue to be a significant effect despite the lack of thermal gradients. The solutal buoyancy flows will, however, be affected by the orientation of the system. The portions of the melt with higher silicon concentrations, with respect to the bulk, will experience a buoyancy force opposite to the gravitational force. This is because the presence of the silicon lowers the density in these areas of the fluid. If the silicon source is at the bottom of the melt, with respect to the direction of the gravitational force, as silicon enters the melt, those areas of melt will experience a solutal buoyancy force. That force, in this situation, will aid the transport of silicon away from the interface and higher dissolution rates should be realized.

In this configuration, with the silicon dissolving from the bottom, the top of the melt can be left as a free surface or capped to eliminate the free surface. The contribution of Marangoni convection to the mass transport in the melt can be examined by varying this condition. The extra mixing induced by the presence of the free surface would be expected to increase the transport of the silicon in the melt. Marangoni flows can be an important transport effect depending on the material and system geometry [88, 102–104]

In the opposite orientation, the silicon enters the melt at the top with respect to the gravity. This material configuration is illustrated in Figure 3.1. In this case, the buoyancy force induced by the dissolving silicon acts to keep the silicon species at the dissolution interface. The introduction of the lighter species at the top of the melt leads to a density gradient in the melt that is stabilized against convection [25]. In this situation, the solutal convective flows should be diminished in the melt. In addition,

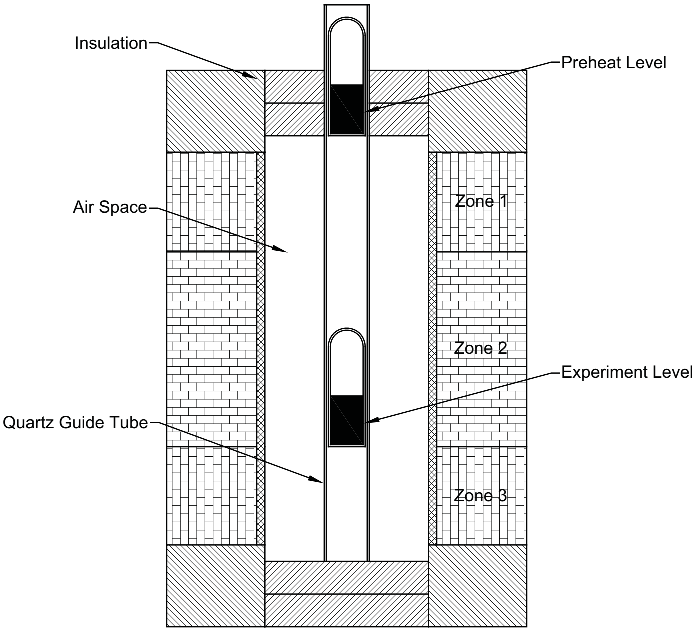

Figure 3.2: The above is a diagram of the furnace system. The furnace has a large bore ($5in$), compared to the experiment ampoule ($1in$). The airspace between the furnace liner and the experiment is constrained such that there is little airflow out and convection cells can form to aid with maintaining the $1000°C$ isotherm. The preheat and experiment positions of the crucible are indicated. The quartz guide tube serves to make moving the sample between positions simple and to constrain the furnace airspace.

any thermal flows that remain in the melt, despite the isothermal conditions, should be damped by the solutal buoyancy. This should lead to the mass transport in this configuration being diffusion dominated. Therefore, the amount of silicon dissolved and its distribution in the melt should be a function of the diffusion coefficient.

3.2.1 Experimental Procedure

In order to conduct the experiments for a known length of time, a procedure for rapidly melting and solidifying the germanium melt zone was developed. A crucible containing the pure silicon source and pure germanium melt was sealed under vacuum and preheated to $800°C$. The preheat and experiment were conducted in the same furnace. The isothermal zone at the experiment temperature of $1100°C$ was maintained throughout the experiment cycle. It is not feasible to change the furnace temperature during an experiment as the time associated with such a change is on the order of hours before the furnace fully stabilizes. Therefore, the $800°C$ preheat zone had to be maintained with the 1100°C isotherm established. The crucible was preheated directly above the isothermal zone such that the minimum temperature it was exposed to was 800°C and the maximum was 900°C. A diagram of the furnace system with both crucible positions indicated is shown in Figure 3.2. This temperature range was used as the thermal gradients in the preheat zone are unstable due to the high gradients and air flow from the furnace. The chosen range guaranteed no premature melting of the germanium and a high enough temperature to allow for quick transition of the germanium into melt when introduced to the isothermal zone. Diffusion between the solid phases will take place, but diffusion in the solid phase is orders of magnitude less than the diffusion in the liquid. The lack of isotherm over the crucible should not adversely affect the experimental results. Instead, it should help in the quick transition of the solid germanium into a molten zone. Modeling of this procedure has shown, for an isothermal 800°C preheat, the time for the sample to reach the experiment temperature is on the order of a minute.

The sample is rapidly dropped into the isothermal zone to start the experiment. Rapid melting of the germanium melt will occur and thermal equilibrium is quickly reached. The silicon source material has a much higher melting point than the experimental temperature and remains solid during the experiment. The silicon begins dissolving once in contact with the melt. To halt the process, the samples were rapidly pulled from the furnace and quenched in ice-water. Using this procedure the time for the dissolution process could be limited to the desired experiment time with an error of only 1 to 2 minutes. All samples were processed with the same procedure. Standard experiment times of 10, 20 and 30 minutes were used.

The experiments were conducted in a 22mm diameter crucible, similar to the conditions present in an LPD experiment. The experiment temperature of 1100°C also reflects the LPD process. In LPD growth, the source is held at approximately 1050 to 1100°C. The depth of the melt was set at 25mm. Again, this reflects the initial melt zone present in an LPD experiment. The geometry of the system will allow for similar flow effects to those found in the LPD process to develop.

This type of dissolution process is not only applicable to LPD growth. In melt replenishment Czochralski, one proposed technique uses silicon rods fed into the melt in order to replenish the silicon content at the growth interface. In this growth process, the mechanisms that transport silicon away from the dissolution interface are very important in order to optimize the pull rate of the growing crystal. Similarly, in Float Zone the transport of the silicon species from the melting interface to the

Figure 3.3: The dissolution crucible is shown above. On the left is a sketch of the crucible arrangement with measures. The photo on the right is of an experiment with the source at the bottom of the melt. The materials are shown just after the crucible has been loaded and sealed.

growth interface determines optimal growth rate.

The baseline Dissolution Experiments were run with no applied magnetic field. The crucible was packed with a silicon source and the germanium for the melt. The silicon sources used were $25mm$ diameter for the bottom orientation experiments and $22mm$ diameter for top source experiments. The extra diameter for the bottom source material allows it to be anchored at the bottom of the crucible. Only the center $22mm$ of the source material is exposed to the melt in this case. The source material is single crystal discs, $5mm$ thick. This thickness ensured that the melt would not fully dissolve the source in any area. The germanium was in chunk form and a sufficient mass was placed in the crucible to form the desired $25mm$ thick melt zone. This arrangement is illustrated in Figure 3.3.

The crucibles used were clear fused quartz. The crucibles were evacuated to approximately $1 \times 10^{-3}\ Pa$ and sealed with a quartz plug. For experiments with the silicon source at the bottom of the melt, the plug was welded into place such that it held the silicon on the bottom of the melt and prevented it from floating to the surface.

The processed samples were sectioned axially into two bulk halves and a $2mm$ thick centerline wafer. The centerline wafer was polished and mounted for obtaining EDS composition profiles. One bulk half was polished and then etched to reveal structure. The etch utilized to reveal the structure of the samples was $H_2O : H_2O_2 : HF$, $3 : 1 : 1$. Samples were dipped in the etch for approximately 10 seconds. If the structure was not apparent, the samples were re-dipped in the etch for additional time until the structure became apparent.

The $2mm$ thick wafers were used for EDS, energy dispersive x-ray spectroscopy, analysis. The wafers were prepared by polishing the samples surface to a sub-micron finish. The $2mm$ thickness was chosen as it was the minimum thickness that still retained enough strength to avoid easy breakage. The rapid cooling of the samples made the material very brittle. The EDS technique was chosen for analyzing the samples as it was readily available for use and is a non-destructive technique. The accuracy of the EDS technique for silicon and germanium detection was maximized by using the K-shell emission lines for silicon and L-shell emission lines for germanium. These emission spectra are close in energy while not overlapping. This makes it possible to obtain good count rates for each elements spectra [105, 106].

3.2.2 Magnetic Field

The experiments as described allowed for the examination of a variety of transport effects. In the configuration with the silicon dissolution interface at the bottom of the melt and the free surface uncovered, mass transport will be by a combination of diffusion, solutal buoyancy flows and Marangoni convection. By capping the free surface Marangoni convection is suppressed in the system and mass transport will be by a combination of solutal buoyancy flows and diffusion. With the silicon dissolving from the top of the melt the free surface is covered by the silicon and the solutal buoyancy acts to stabilize the melt against convective flows. In this case, it is expected that diffusion will be the primary mass transport effect.

To further investigate the effect of flows on the mass transport in the melt, a static magnetic field was used to manipulate the flow structure in all three of the material configurations. A static magnetic field of $0.8\ T$ was applied, along the vertical axis, to suppress convective flow. This arrangement is shown in Figure 3.4. The strength of field was chosen based on previous work to suppress convective flow. The chosen field strength is relatively high by design to ensure that a strong effect would be realized in the experimental results.

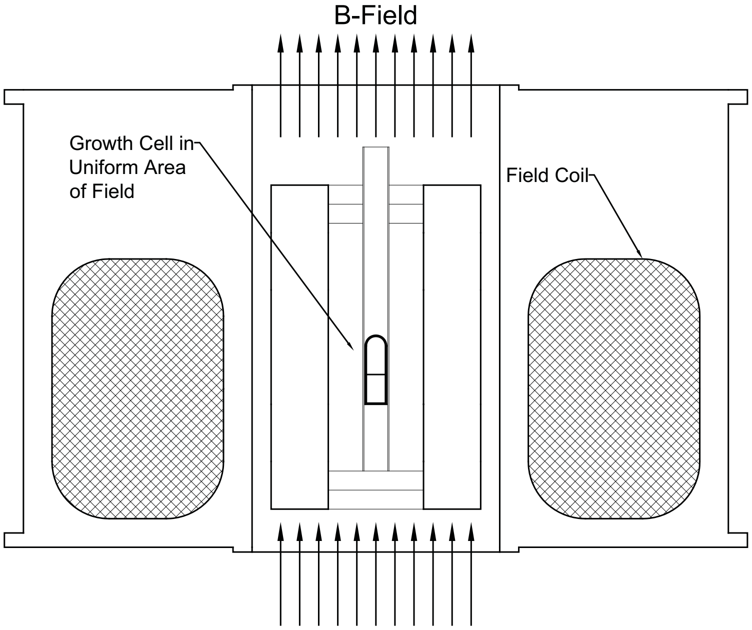

Figure 3.4: The furnace and magnetic field generator arrangement is illustrated above. The field lines are in opposite direction to gravity and aligned with the vertical axis of the crucible.

3.3 Baseline Experiments

The following work was published by the author in the Journal of Crystal Growth [33].

The baseline experiments were run with no applied magnetic field. The crucible was packed with a silicon source and the germanium for the melt. The first configuration is silicon source at the bottom of the melt. In this setup, the silicon source is placed into the crucible with the germanium on top. The plug was welded into place such that it held the silicon on the bottom of the melt and prevented it from floating to the surface. This configuration is referred to as Configuration A. The three experiment configurations are illustrated in Figure 3.5.

Configuration B is identical to Configuration A except a graphite disc is placed on top of the germanium melt. The graphite will act to suppress surface convective flows in the melt. Graphite was used as it does not wet to the germanium and the graphite disk could be reused from experiment to experiment.

Configuration C is the inverse of Configuration A. In this case the melt and source positions are reversed. The silicon source floats on top of the germanium melt from the outset of the experiment. There is no free surface in this configuration as the silicon source covers the top free surface.

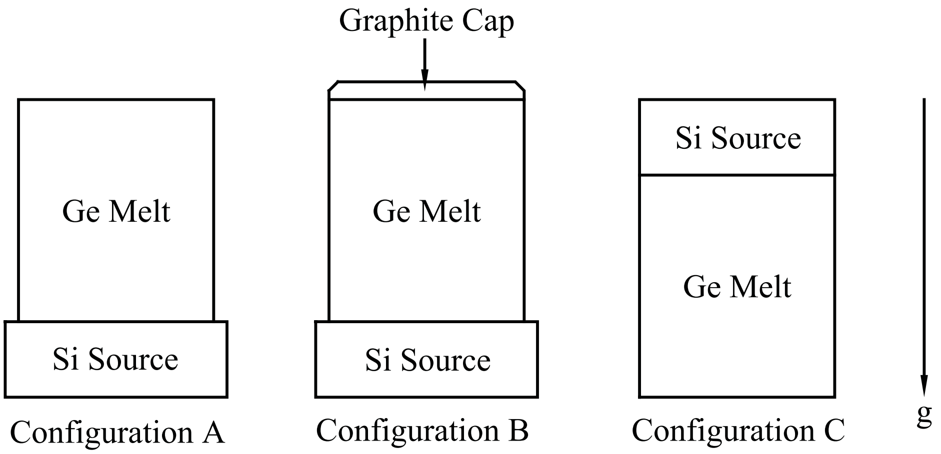

Figure 3.5: Shown are the three experimental configurations used. The direction of the gravitation acceleration vector is shown.

3.3.1 Configuration A and B

Configuration A was run for the three experimental times, $10min$, $20min$ and $30min$. In all of these experiments, a high dissolution rate was exhibited. The dissolved height of silicon was in the 2-$3mm$ range. The time evolution of the dissolution height shows a decaying trend. This is shown in Figure 3.6. This is likely due to the melt approaching its saturation limit. As the concentration in the melt rises, the transport mechanisms of diffusion and solutal buoyancy will slow as they are driven by the concentration gradients in the melt. The saturation concentration is determined by the liquidus line on the phase diagram. The melt cannot accommodate silicon above this saturation concentration. The saturation concentration does vary with temperature. However, under the isothermal conditions imposed on the melt, the saturation concentration is constant throughout the melt. Configuration B also exhibited the same time dependant behavior, with the rate of dissolution falling with time.

Comparing the dissolved heights of Configuration A and Configuration B, a trend is clear. More silicon is dissolved in the presence of a free surface at the top of the melt. The effect is small but consistent across all of the experiment times. This shows that Marangoni convection is contributing to the mass transport in the system. Again the system is in an isothermal environment. It is expected that radial temperature gradients will be minimized. The graphite cap on the free surface will effect how the

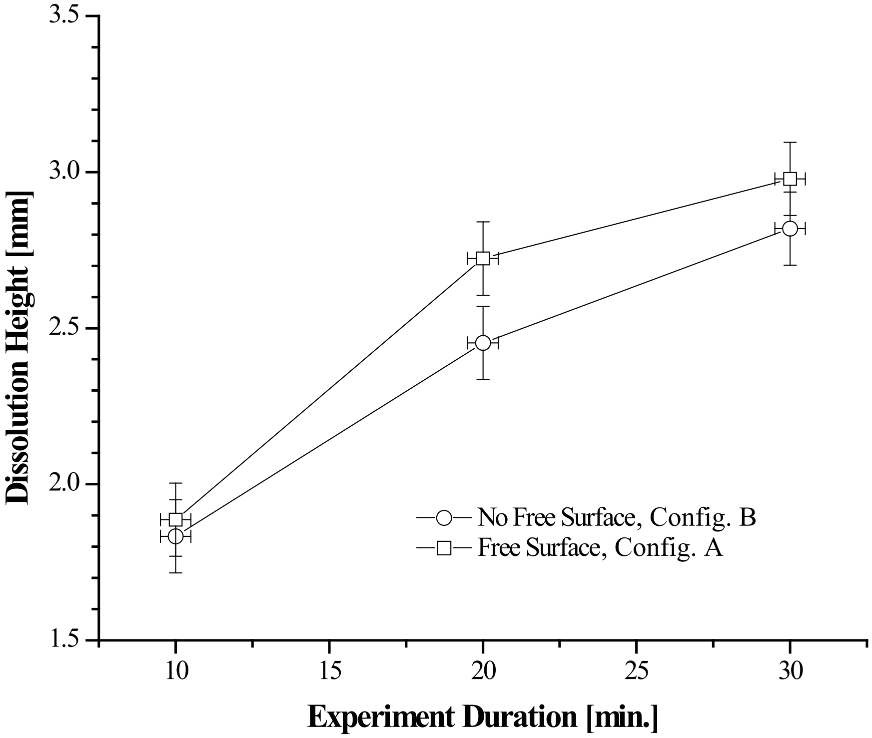

Figure 3.6: Plot of the dissolution heights of Configurations A and B with respect to experiment time.

system comes to thermal equilibrium when introduced to the experimental temperature. During this short time, there are different thermal gradients present in the melt. However the differences are minor and unlikely to be large enough to be the source of the dissolution difference given the short time period in which they occur. There is likely to be concentration gradients at the free surface. However, it is expected that silicon will preferentially build up at the free surface due to the buoyancy force it experiences. The buildup of silicon should help minimize any concentration gradients present. Given these factors, the extra mixing seen in Configuration A over Configuration B seems attributable to Marangoni convection.

In the system under study, the free surface is only approximately $350mm^2$ in size. The volume of the melt is approximately $9500mm^3$. This is a relatively high ratio of volume to surface area when compared to growth techniques such as Czochralski and Float Zone. As this ratio changes to higher surface area for similar volume, it would be expected that the contribution of Maragoni convection to the overall transport would increase. For Czochralski growth, where the melt has a lower ratio of volume to surface area, it is likely that Marangoni convection will play an important role in the mass transport. The contribution of free surface convection to mixing is substantial enough to warrant attention when considering SiGe growth systems.

In Configurations A and B, the dissolution interface shows signs of being unstable. This becomes very apparent with the samples processed for $30min$. A sample exhibiting this is shown in Figure 3.7. These samples show a very wavy dissolution interface. This is likely due to strong flow across the interface. As the thermal gradients are minimized, this flow would seem attributable to the solutal buoyancy flows. The presence of such an interface indicates the formation of unstable flow structures in the melt and rapid chaotic mixing.

The boundary layer is visible adjacent to the dissolution interface. This is shown in Figure 3.8. This is identified on the differentially etched samples. The etch highlights a thin band of high silicon concentration adjacent to the dissolution interface. The layer shows consistent thickness and uniformity across the processed samples. The visibility of this layer highlights the concentration difference between the boundary and the bulk of the melt. Rapid transport away from the dissolution interface is taking place in order to make this transition so clear. In the diffusion dominated boundary layer, the silicon concentration builds up. Then, as it diffuses into the bulk of the melt, it is rapidly mixed by convective flows.

EDS composition measurements were taken for all processed samples. The obtained composition profiles provide insight but are hindered by segregation in the melt. On quenching, the silicon segregates out of the germanium melt. This results in high silicon concentration zones within a germanium rich matrix. The silicon seg-

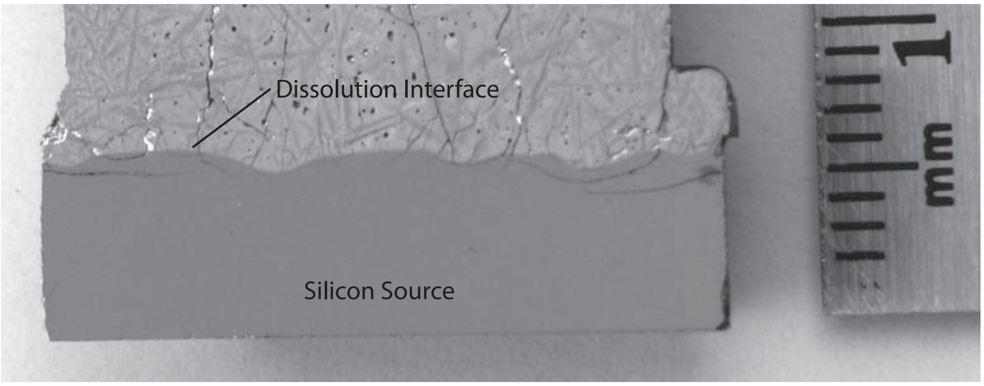

Figure 3.7: The dissolution interface for a sample processed for $30min$ is shown. The interface is very wavy indicating the dissolution is an unstable process.

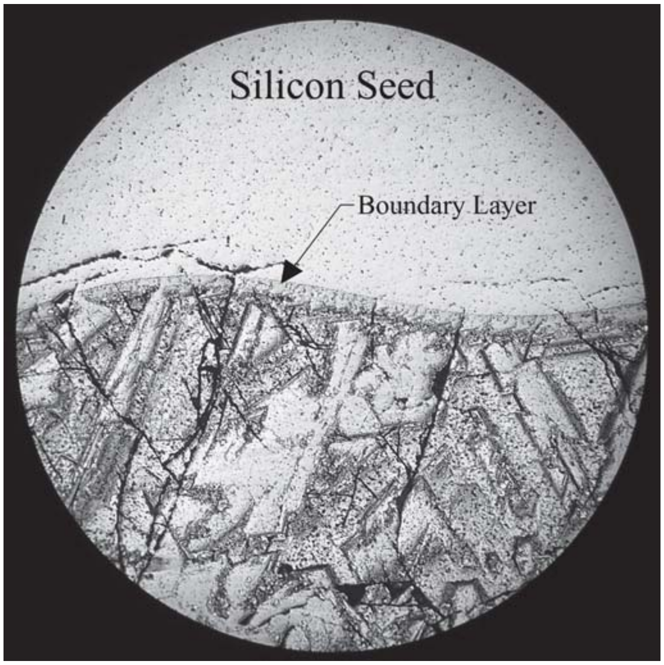

Figure 3.8: The dissolution interface boundary layer is visible on the differentially etched samples. The etch highlights the areas of higher silicon concentration. The visibility of the layer indicates a sharp change in concentration at the boundary edge. The photo above has been enhanced to increase contrast so the layer is more apparent.

regates as visibly identifiable needle like crystal structures. This is shown in Figure 3.9. The fast quenching process should help avoid macro-segregation. Microscopic segregation will still occur even with a fast quench. In the case of the silicon germanium melts here, it would appear that even with the fast quenching significant macro-segregation has taken place. The grain size of the precipitated silicon is large making accurate measurements difficult. The segregation can be smoothed somewhat by using larger areas for the composition measurements. However, there is a limit to the area that can be feasibly measured. In this work, a frame size of $450\mu m$ x $450\mu m$ was utilized. With these limitations, the composition profiles show a relatively high degree of scatter. However, some trends can still be identified.

The concentration profiles of both Configuration A and B exhibit a similar shape. There is high silicon concentration adjacent to the dissolution interface. This is consistent with the boundary layer observed in the differentially etched samples. The EDS plots are shown in Figure 3.10. The silicon concentration then drops though the center of the melt to a fairly even value. The top surface of the melt, both with and without the free surface present, shows a marked increase in silicon concentration.

Figure 3.9: The needle structure indicating the presence of silicon is visible in the photo above. A uniform random distribution of the needle structure is apparent.

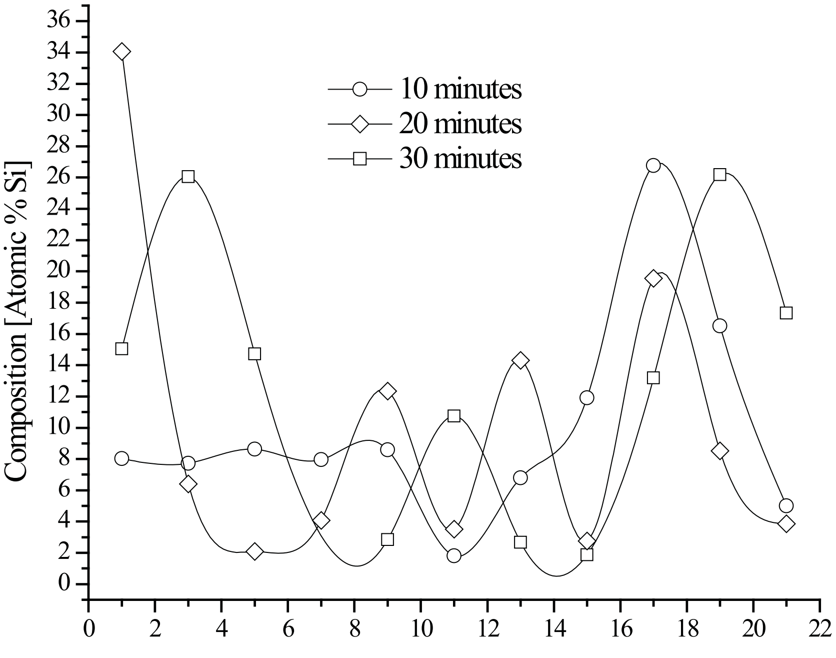

Figure 3.10: EDS composition measurements of Configuration A. The three experimental times are overlaid. The drop in composition through the center of the melt is evident.

This is consistent with the buoyancy force on the silicon causing the concentration to increase at the top surface. The radial concentration profiles in the melt were relatively flat. This supports the supposition that the concentration gradients at the free surface will be low due to silicon species building up due to the buoyancy force.

3.3.2 Configuration C

Configuration C is similar to the material setup found in the LPD experiments. There is no seed for these experiments and no thermal gradient is applied. However, the silicon is placed at the top of the melt and the temperature at the interface is comparible to that used in the LPD system. The direction of transport into the melt with respect to gravity is the same as the LPD system.

In a typical LPD experiment, a silicon source with a thickness of $2mm$ will last for approximately 5 days. In Configurations A and B, dissolution of $2mm$ was seen in around 10 minutes. This indicates that the convective transport was the predominant transport mechanism in Configurations A and B. In LPD experiments, the buoyancy of silicon acts to damp out convective flows. This effect is expected to be magnified in Configuration C as the thermal gradient has been removed from the system. The LPD system, in contrast, is subject to a high thermal gradient that can drive thermal convective flows.

The dissolution heights recorded for Configuration C were in the $0.5mm$ to $1mm$ range. This is substantially less than the heights recorded for the other configurations. A plot of dissolution heights is shown in Figure 3.11. In addition, over the time period measured it does not seem to exhibit the obvious decay behavior present in the other configurations. This is expected as the lower amount of dissolved silicon indicates the melt is not approaching the saturation concentration as quickly as the other Configurations. Close examination of the results shows there is a slight trend to a lower dissolution rate. This is likely due to the reduction in the concentration gradient as the silicon is mixed into the melt.

The extent of the silicon transport into the germanium can be visibly seen in the differentially etched samples. This is shown in Figure 3.12. The presence of silicon in the melt is characterized by the presence of a needle like crystal structure. This structure seems to form due to the macro-segregation silicon during the quenching process. The EDS composition measurements verify the end of the needle structure as the limit of silicon transport into the melt. A plot of the EDS data is shown in

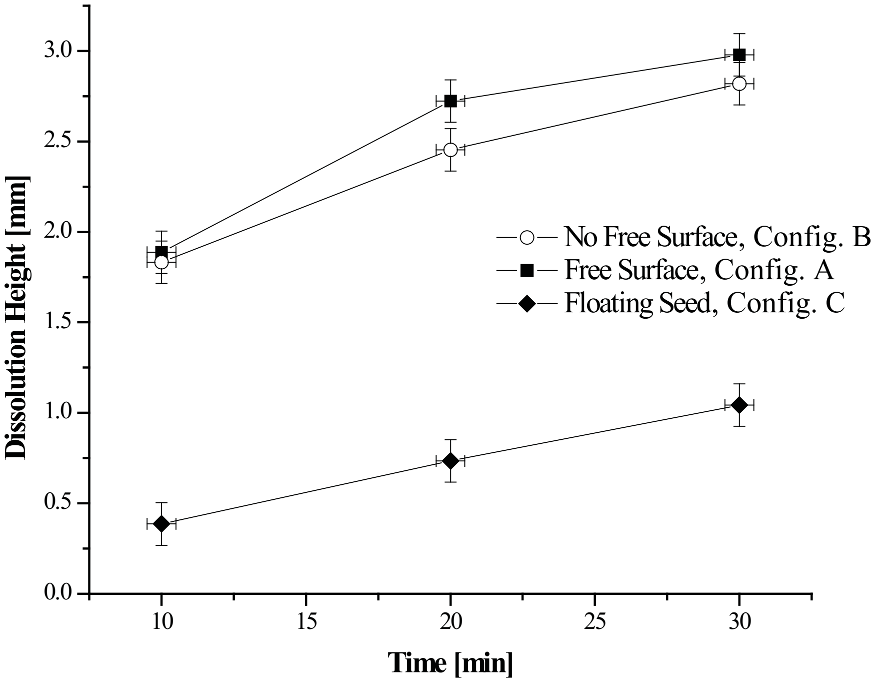

Figure 3.11: The dissolution heights for all three configurations are plotted versus time. The dramatic reduction in dissolution for Configuration C is apparent.

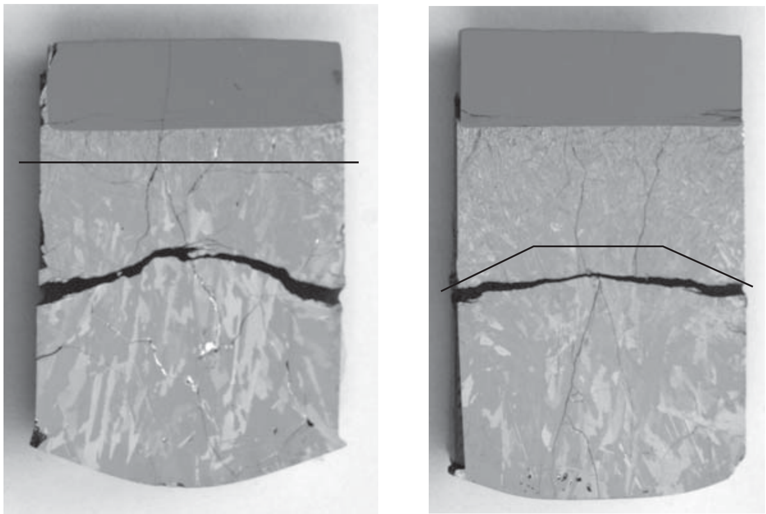

Figure 3.12: The extent of the needle structure associated with silicon concentration into the melt is illustrated by the dark lines in the photos above. The photo on the left is material processed for $10 min$. The photo on the right is material processed for $20 min$.

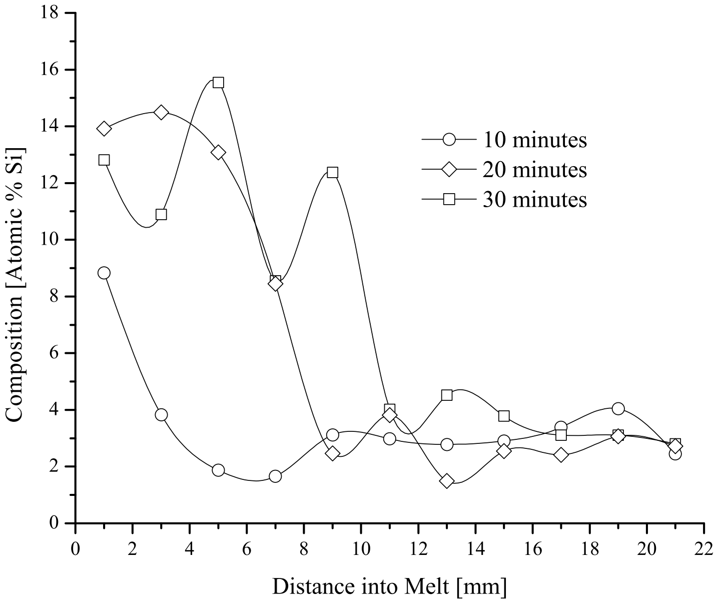

Figure 3.13: Shown above is a plot of the EDS composition values for Configuration C. Plots for all three experiment times are overlaid. The extent of silicon transport is evident.

Figure 3.13.

As it is expected that the transport in this system should be dominated by diffusion, it should be possible to extract a reasonable value for the diffusion coefficient in the system. There are thermal driven buoyancy flows in the melt during the start of the experiments as the temperature rises from the preheat temperature to the experiment temperature. Modeling of this process has shown that convective cells do form but are quickly weakened and damped out as the silicon begins dissolving and the temperature equilibrates. The system then precedes diffusion dominated. Given this, it would be expected that the effective diffusion coefficient for this experiment would be higher than the actual value due to the additional mixing at the start of the experiment.

Numerically modeling a system with no convective flow so mass transport is only by diffusion, it was found that the model predicts more dissolution than that observed. This numerical model is discussed in detail in Section 3.5.3. The diffusion coefficient that was used was $2.5 \times 10^{-8}\ m^2/s$. This value for the diffusion coefficient has been used in previous modeling of SiGe growth. The slope of the dissolution curve from the model is also different to that of the experiment results. By varying the diffusion coefficient, the slope of the dissolution curve can be changed. Good agreement can be found at a diffusion coefficient value of $5.0 \times 10^{-8}\ m^2/s$. However, the curve from the model is offset by approximately $0.4mm$ in dissolved height from the experimental result. This data is plotted in Figure 3.14. Using a linear fit on both curves shows that the slopes of the curves match well, but the intercepts are far apart. A likely cause for this is non-equilibrium effects during the dissolution process. It has been suggested that surface kinetics could play an important role in crystal growth [107]. These effects are not accounted for in the equilibrium model used in this work. Inclusion of these effects may be required for accurate modeling of the physical phenomena.

By including the solutal buoyancy body force into the numerical model, the computed dissolved height curve is slightly altered. The buoyancy force acts to induce weak flow in the melt. However, rather than limiting the amount of transport, it serves to help mix the silicon species into the melt. This is shown in Figure 3.15. With the inclusion of solutal buoyancy, the model result further diverges from the experimental result. The mixing acts as an additional additive effect to the height dissolved. The shape of the curve is maintained but the height dissolved is increased.

To better match the experiment results, the time for the dissolution interface to reach saturation was varied. As the germanium melts and contacts the silicon source, it will take time for the interface boundary layer to reach equilibrium. This interface is usually modeled as being saturated to a composition determined by the liquidus line. In this case, the concentration was varied linearly in time from zero to the saturation composition. The time to reach saturation is unknown. However, as a first approximation, the time for the system to reach thermal equilibrium, approximately 90 seconds, was used. This lowers the heights dissolved approximately $0.05mm$, a minor effect. By increasing this time further, the dissolved height continues to trend downwards but the shape of the curve is affected. The physical validity of the boundary requiring a long time to come into equilibrium requires further investigation. In general this is a process that happens quickly as this region experiences large concentration gradients at the start of dissolution and transport in the boundary layer is primarily by diffusion. A fit using this approach is shown in Figure 3.16. While the fit is still imperfect, the approach shows promise and a better fit could likely be realized by utilizing a more complex ramp function for the saturation composition.

It is also possible that some mass transport effect has been left out of the model. However, additional thermal or solutal flows would seem to only increase dissolu-

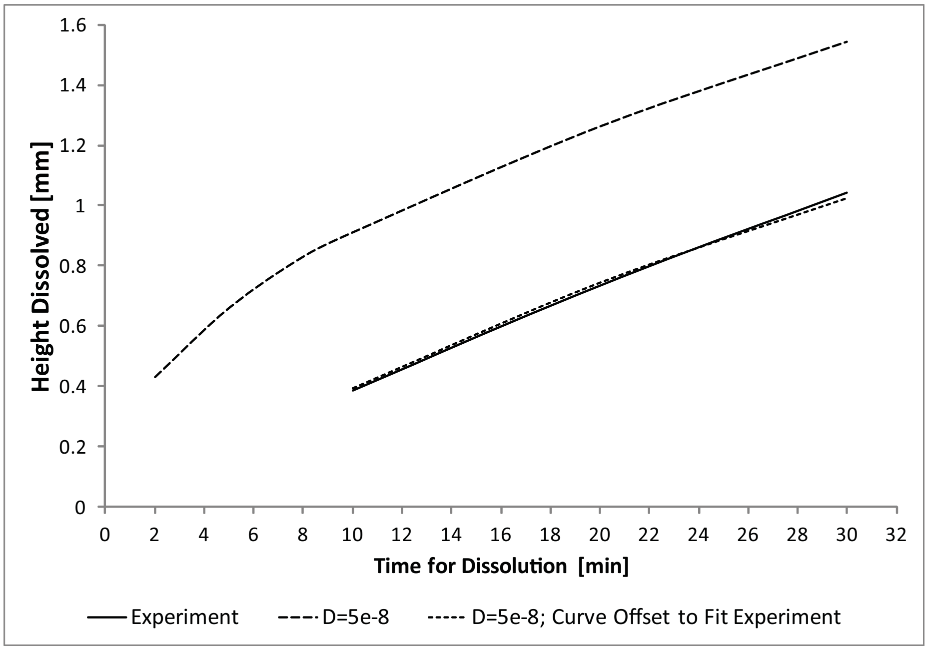

Figure 3.14: Dissolution heights of the experimental data and a numerical model using a diffusion coefficient of $5.0 \times 10^{-8}\ m^2/s$. The slopes of the curves are in good agreement, but there is offset between them.

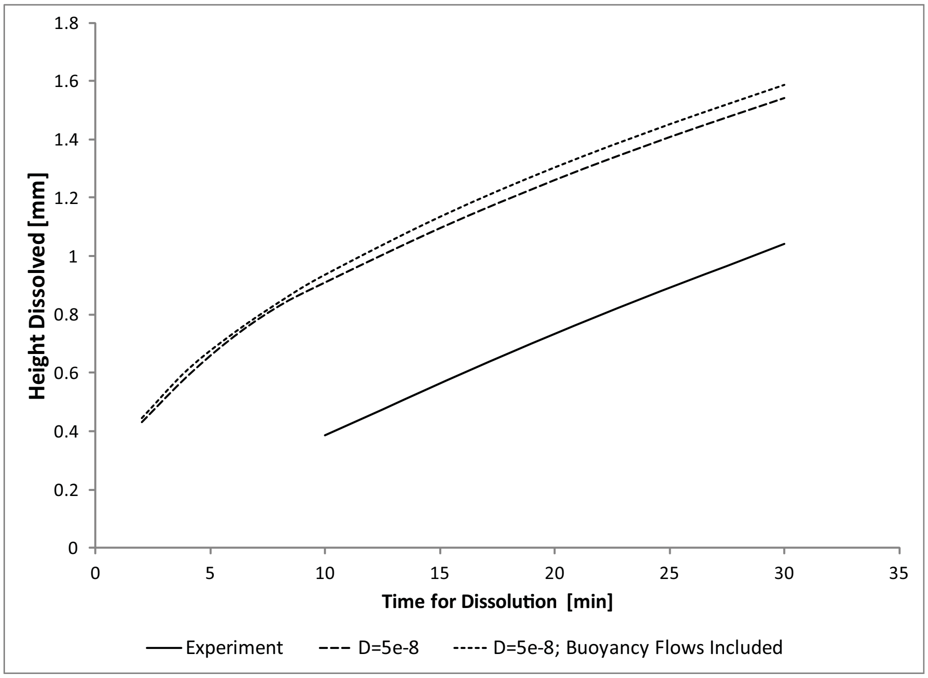

Figure 3.15: Dissolution heights of the experimental data and two numerical models, one with and one without solutal buoyancy included. The diffusion coefficient used in the model was $5.0 \times 10^{-8}\ m^2/s$.

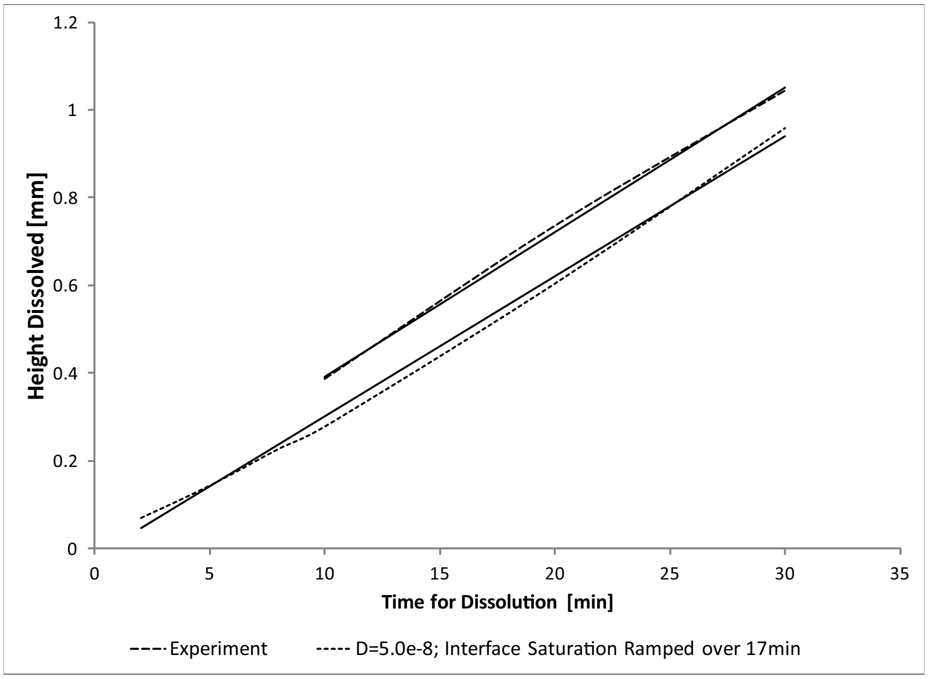

Figure 3.16: Experimental dissolution heights and modeled dissolution heights are shown. The interface condition in the model is time dependant. The concentration is ramped to saturation following the equation $0.12/1020t + 0.03$. Where t is the experiment time in seconds. The interface is ramped over 17 minutes. Linear fits have been overlaid both data sets to show the similarity.

tion and not reduce the dissolved height. A smaller diffusion coefficient does not adequately explain the reduced dissolution exhibited in the experimental results. A reduction in the diffusion coefficient flattens the dissolved height curve as well as lowering the dissolved heights. Including the solutal flows with the reduced diffusion coefficient has the effect of increasing the dissolution heights, but the flatness of the curve remains. It would seem that the initial condition for the start of the dissolution in the numerical model needs modification. The experiment curve proceeds like the modeled diffusion dominated system with a diffusion coefficient of 5.0×10^{-8} m^2/s. However, the initial rapid dissolution that takes place in the numerical model does not occur in the experimental system. It is possible that the buoyancy of the silicon has a strong effect during this time period to keep the dissolution low.

The buoyancy of the silicon has a strong effect on the dissolution and transport in the system. It should be expected that the orientation of the silicon dissolution interface will profoundly affect the effective diffusion coefficient in a SiGe growth system. In other orientations, it is likely that buoyancy driven flows will become the primary mass transport mechanism and diffusion will be secondary. This was seen in Configurations A and B.

3.3.3 Discussion

Applying these results to the LPD and melt replenishment Czochralski crystal growth techniques, a number of issues become apparent. In both techniques, transport of the dissolving silicon to the growth interface is the main determinant of growth velocity. In LPD, the dissolving silicon must supersaturate a fluid layer at the growth interface for growth to occur. The speed at which this occurs determines the growth velocity. For melt replenishment Czochralski, in order to keep the growing crystal at a constant composition, the pull speed must be set such that the added silicon can mix into the melt and keep the melt near the interface at constant composition. The rate at which silicon mixes through the bulk of the melt and replenishes the silicon consumed at the solidification interface will determine the maximum pull rate for a constant composition crystal.

For both techniques, fast growth velocities require that the transport of silicon be increased as much as feasible. It would seem that orientating the dissolution interface to take advantage of the silicon buoyancy effect would help achieve higher growth rates. The mixing of silicon into the melt is clearly improved with the dissolution interface at the bottom of the melt. However, it has been observed that the strong flow induced in this orientation has made the dissolution interface unstable. Given this, it is likely that the strong flow structure could destabilize the growth interface as well and therefore degrade the quality of the grown crystal.

Utilizing the silicon buoyancy effect to aid transport, while controlling the induced buoyancy flows, may be possible by utilizing a static magnetic field. The static field should act to suppress convective flow. This would allow for more control of the solutal driven mixing and therefore lead to more stable dissolution and growth interfaces. In a technique like LPD, the distance between the dissolution interface and the growth interface could be increased to help control mixing. For Czochralski growth, the use of a double crucible type arrangement may be more beneficial than feeding solid silicon into the melt. The buoyancy force on the melt being fed into the growth crucible would be controlled by the composition of the melt in the outer crucible. A large difference in composition would lead to strong buoyancy flows while decreasing the amount of melt that has to be fed into the inner crucible during a growth run. A small composition difference would require more material to be fed into the inner crucible during a growth run but a lower buoyancy force on the introduced material would be realized. Careful modeling of this process will be necessary to find the appropriate balance of factors.

3.4 Static Magnetic Field Experiments

A static magnetic field of $0.8T$ was applied to the experimental setups discussed in the previous section. The field strength was chosen based on previous work to suppress convective flows in a semiconductor melt. A field strength on the higher end of what has been used was chosen to highlight the effect of the static field. All other parameters of the experiments were maintained. The field was aligned along the vertical axis of the experiment and the sample was placed in a radially uniform area of the field.

3.4.1 Configurations A and B

The following work was published by the author in the Journal of Crystal Growth [35].

The applied magnetic field will first be discussed for Configurations A and B. The dissolution interface is at the bottom of the melt and the transport is characterized by strong solutal buoyancy flows. The application of a static magnetic field should act to suppress the convective flows in the melt. The magnetic field does not directly act on the axial component of the flow. Instead, the field influences the radial and tangential components which in turn suppress the formation of large convection cells. This would reduce mixing and therefore reduce the dissolved height of silicon. What is evident from the experimental results is that the application of the static field acted to enhance the dissolution of silicon into the melt. This can be seen in Figure 3.17. The flow structure in the melt is being altered by the applied field in such a way as to increase the transport of silicon.

The trend of the free surface acting to enhance the transport in the melt is evident in the experiments conducted under the static magnetic field. More silicon is dissolved when the top of the melt is a free surface. This implies that the Marangoni convection is unaffected by the application of the field as the same effect was observed with no applied field. However, the body force induced by the magnetic field will affect Marangoni flows. Therefore, it is possible that another flow effect is present in the

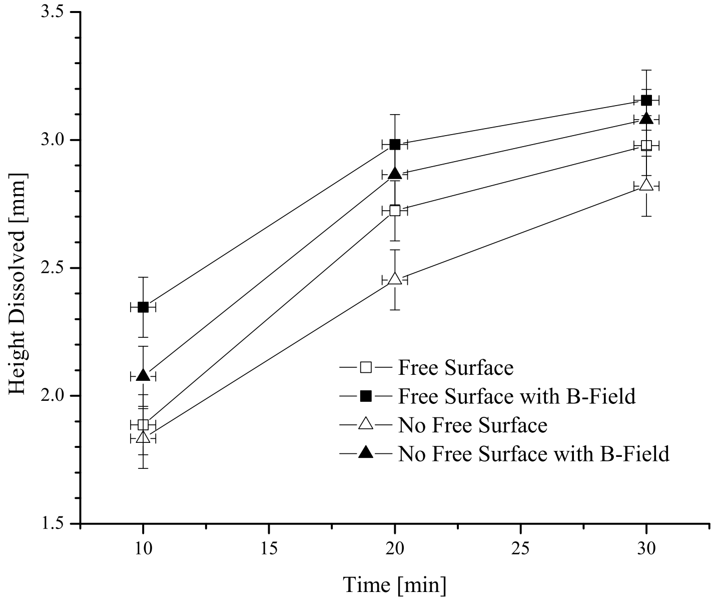

Figure 3.17: Dissolution height plots of Configurations A and B with and without magnetic field. The increased dissolution with application of the magnetic field is evident.

melt. One possibility could be stronger solutal driven Marangoni flow due to an altered concentration field in the melt. Another possible effect could be enhanced azimuthal flow from thermoelectromagnetic convection.

The mechanism of the magnetic field aiding in the transport of silicon in the melt could be explained as follows. During the heat up to the experiment temperature, thermal flows will occur in the melt. Fluid will flow up the hot crucible wall and downward through the center of the melt. The downward flows will return silicon back towards the dissolution interface. The returned silicon will reduce the concentration gradients in the area of the dissolution interface. This will slow the dissolution rate. When these currents are strong, it is expected that this could help reduce the height of silicon dissolved.

When the magnetic field is applied, the flow structure is changed and the formation of large convective cells is suppressed. This will reduce the mixing of the dissolved silicon back towards the dissolution interface. In this case, the buoyancy of the silicon causes it to rapidly transport away from the dissolution interface. The silicon will tend to build up at the top of the melt due to its buoyancy in the germanium melt.

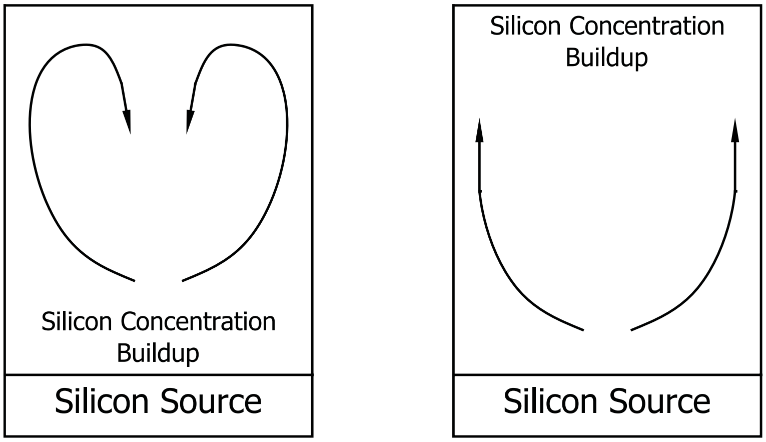

Figure 3.18: Above is an illustration of possible flow phenomena in the dissolution of silicon with (right) and without (left) magnetic field. In the sketch on the left, flow acts to remix silicon from the top of the melt back to the dissolution interface. This reduces the concentration gradients around the interface. In the sketch on the right, the flow is suppressed from remixing silicon from the top surface back to the dissolution interface. Therefore the concentration gradients around the dissolution interface remain high and more dissolution is realized.

Without the magnetic field, the build up of silicon at the top surface of the melt is partially remixed into the bulk by convective flow and acts to reduce the dissolution rate. With the magnetic field applied, the reduction in dissolution rate does not occur and larger dissolved heights of silicon are observed. The remixing of silicon from the top surface towards the dissolution interface is suppressed. This change in flow structure is illustrated in Figure 3.18. This could be the phenomena observed in both Configuration A and B.

This explanation is supported by the silicon concentration profiles in the processed samples. In the differentially etched samples, the areas with a reasonable concentration of silicon show the macro-segregation of the silicon species into a needle like structure. This reliably indicates the presence of silicon in the melt. In the samples processed without an applied magnetic field, an even distribution of the needle structure is observed. In the samples processed with the applied field, a marked reduction in the concentration of the needle structure is noted in the middle of the melt. This can be seen in Figure 3.19. This would indicate that the concentration of silicon in the center of the melt in the samples processed under the applied magnetic field is lower than the surrounding areas. The anisotropy of the silicon distribution is related

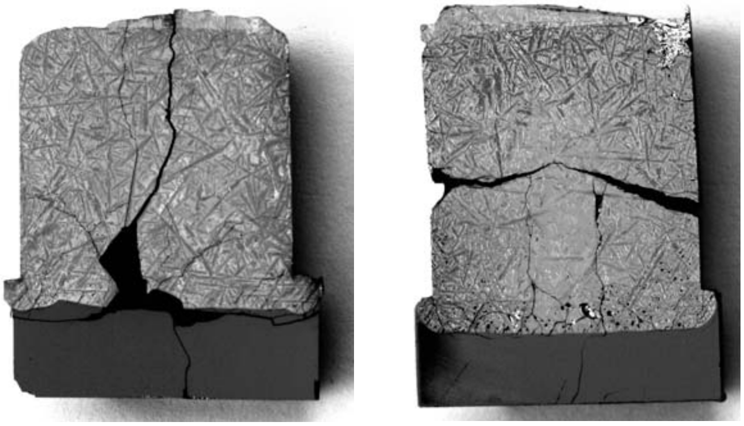

Figure 3.19: The above are photos of material from Configuration B processed for 20min. The sample on the left was processed without magnetic field and exhibits a uniform distribution of the needle structure that indicates silicon concentration. The sample on the right was processed with the magnetic field applied. The reduction of the needle structure in the center of the melt is evident.

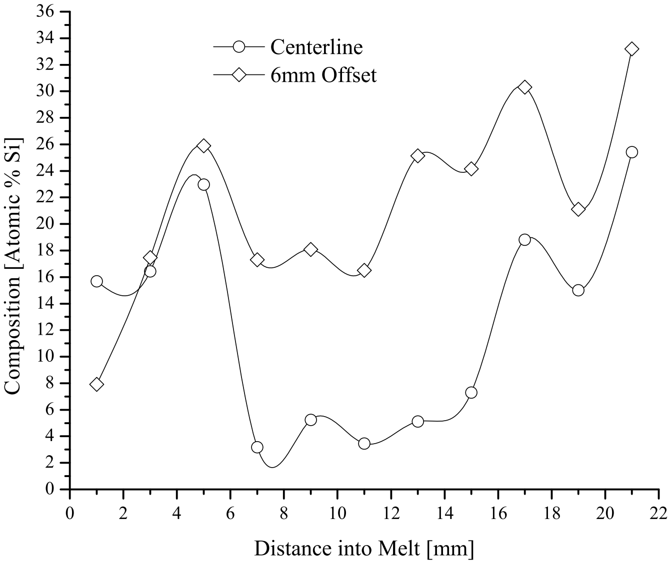

Figure 3.20: EDS composition plot of Configuration B sample processed for 20min with applied magnetic field. The centerline plot is from the center of the sample starting at the dissolution interface. the $6mm$ offset plot is another axial composition profile offset $6mm$ radially from the centerline profile. The drop in silicon concentration through the center of the melt is very evident by comparing these data plots.

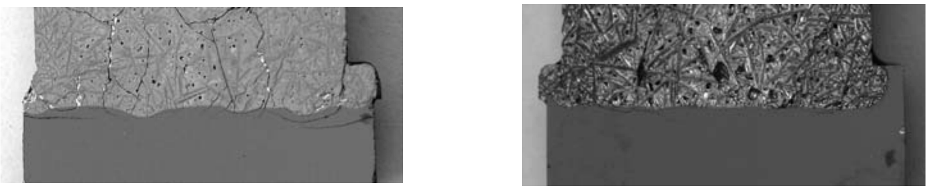

Figure 3.21: The above photos show the dissolution interface shape with and without the applied magnetic field. The sample on the left was processed without the magnetic field. The wavy interface indicating unstable dissolution is evident. The sample on the right was processed with the applied magnetic field. In this case, the dissolution interface is much smoother indicating a more stable process.

to the application of the magnetic field. This would support the earlier explanation that the magnetic field is preventing remixing of silicon back towards the dissolution interface through the center of the melt. This results in a lower concentration of silicon in the center of the melt.

This is further supported by the concentration profiles obtained from the EDS analysis. For the sample processed with the applied field, the composition profile near the crucible edge shows a relatively even concentration profile over the extent of the melt. However, the centerline concentration profile of the samples processed with the applied field show a distinct drop in silicon composition through the center of the melt. This is shown in Figure 3.20.

In the previous examination of the samples processed in Configurations A and B, it was noted that the dissolution interface was wavy. This indicates that the flow across the interface may have caused instabilities. It is likely that the instabilities are due to strong radial and azimuthal flow. With the application of the magnetic field these flows should be suppressed and the interface should stabilize. This effect was seen in the samples processed under the magnetic field. The samples show a far flatter dissolution interface when the magnetic field is applied. This can be seen in Figure 3.21.

The application of the magnetic field has a number of effects on the transport and flow in the melt. The dissolution interface is stabilized. This is likely due to reduce radial and tangential flows. The amount of dissolution is increased. Again, the radial and tangential flows are reduced and less silicon is mixed from the top surface of the melt back towards the dissolution interface. This keeps the concentration gradients around the dissolution interface high and drives more dissolution. Finally, the effect of the free surface on transport is not impacted by the applied magnetic field.

3.4.2 Configuration C

The following work was published by the author in the Journal of Crystal Growth [31].

In Configuration C with the dissolution interface at the top of the melt, the same effect of the dissolution increasing with the application of the static magnetic field was observed. This is shown in Figure 3.22. Without the field, in this material configuration, the transport proceeds as a diffusion dominated process. The dissolution interface is also very flat, indicating that the flow structure is relatively weak.

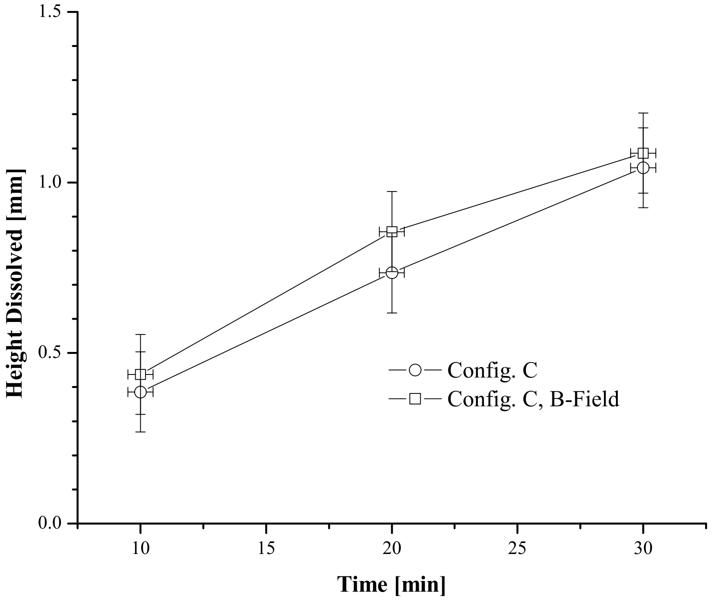

Figure 3.22: Dissolution heights of Configuration C with and without magnetic field. The trend of higher dissolution with magnetic field applied is apparent.

There will be thermally driven flows at the start of the experiment as the crucible reaches thermal equilibrium. The magnetic field is expected to help reduce these flows and keep the system diffusion dominated for the entire duration of the experiment. This is not what was observed. The magnetic field acts to disrupt the dissolution interface. Specifically, the rate of dissolution near the crucible walls is significantly enhanced over the silicon dissolution in the center of the melt. This can be seen in Figure 3.23. This implies the addition of flow structure in the melt.

With the application of the magnetic field, silicon is being mixed away from the dissolution interface more rapidly at the crucible walls than at the center of the

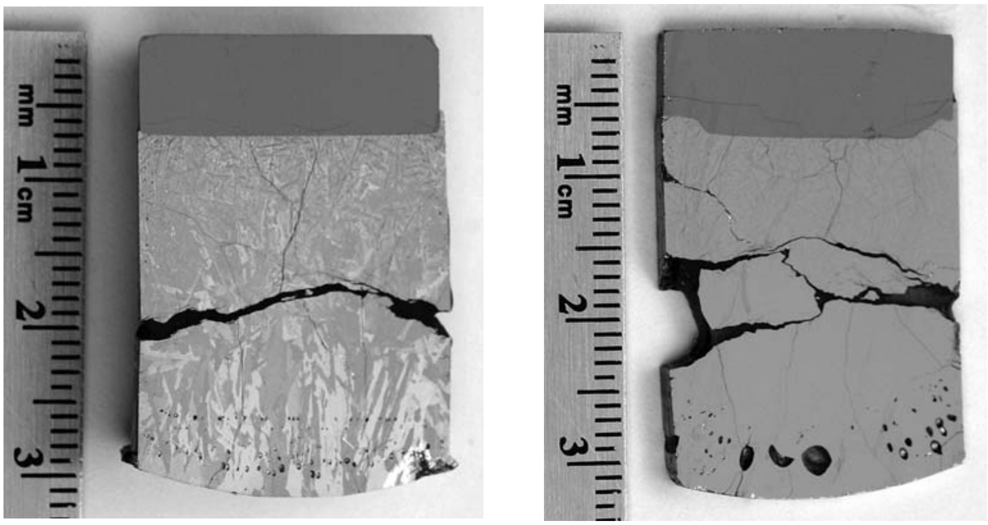

Figure 3.23: Dissolution interfaces in Configuration C with and without applied magnetic field. The photo on the left is of a sample processed without the magnetic field. The dissolution interface is very flat. The photo on the right is a sample processed with the applied magnetic field. The areas of high dissolution near the crucible wall are visible.

interface. This indicates significant alteration of the flow field. The extent of the silicon transport into the melt is only slightly affected by this modified flow structure, while the dissolution interface is dramatically altered. This would indicate that the magnetic body force is serving to enhance radial and azimuthal flows while axial flow is unaffected. The radial and azimuthal flow structure could act to mix silicon away from the crucible edge and into the center of the melt. This would drive dissolution at the crucible walls while slowing the dissolution in the center of the interface. This could lead to the deformation of the interface observed in experiments. Stronger radial and azimuthal flows could also account for the additional mixing of silicon into the melt. If the axial flows are not enhanced to the same extent as the radial and tangential, a significant increase in dissolution would not be expected.

The magnetic field was applied to suppress any natural convection that may be present in the melt. However, this was not the effect observed. Instead it seems that the field enhances radial and azimuthal flow structure in the melt. This strengthens the flow and the convective mass transport in the system.

This type of effect may be useful in crystal growth techniques. For LPD, the growth interface shape evolves with time as the silicon is not transported equally across the melt. Instead, silicon is transported more quickly through the center. The LPD growth interface starts concave to the melt. As silicon is transported faster through the center, this shape evolves from concave into convex to the melt as growth proceeds. A flat growth interface is optimal. Enhancing the radial and tangential flows to help reduce the concentration gradients in the radial and tangential plane would ensure that silicon is transported evenly through the melt, reducing the growth interface shape evolution.

3.5 Numerical Modeling

3.5.1 Configuration C under Static Magnetic Field

The following work was published by the author in Fluid Dynamics and Materials Processing [32].

In order to further examine the disruption of the dissolution interface in Configuration C with the application of a magnetic field, a three dimension numerical model was developed. The material parameters, governing equations and body forces discussed in Section 2.5 were utilized. The numerical solution was obtained using the commercial ANSYS CFX finite volume based solver. The simulated domain is shown in Figure 3.24.

With high body forces present in the melt from the magnetic field as well as the buoyancy body force terms, it was not possible to acheive a converged solution for a reasonable time length. To overcome this issue, the gravitational and magnetic body forces were scaled down while maintaining the ratio between them. The forces were both scaled down by a factor of ten. Utilizing this approach, a converged solution was obtained for a 20 minute experiment time.

The dissolving boundary is taken as stationary and saturated in silicon according the phase diagram. The thermal field is initialized at $800°C$ with boundaries of $1100°C$. This simulates the drop from the preheat zone into the isotherm of the furnace. In order to achieve a converged solution, the thermal expansion contribution to the buoyancy body force term was neglected. Thermal modeling showed that the system comes to thermal equilibrium quickly, less than 90 seconds. The method of heat transfer from the outer crucible wall to the material was considered to be entirely by conduction. Given that quartz is transparent in the infrared, radiation can be a significant factor to the initial heating. Inclusion of the radiation effect would serve to reduce the time for the system to come to equilibrium. Therefore the 90 seconds for the system to come to equilibrium should be considered an upper limit. Given the

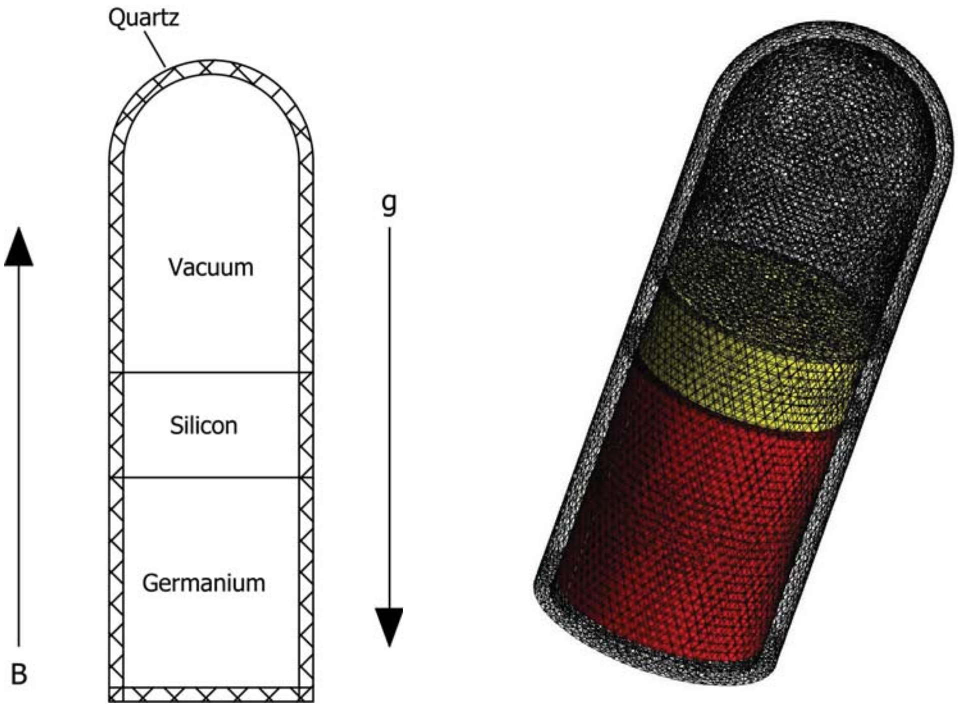

Figure 3.24: The model domains are illustrated on the left. The mesh used for the problem is diagrammed on the right.

20 minute time frame for an experiment, it would seem a reasonable approximation to neglect the effect of thermal driven flows. The effect of thermal expansion on the concentration field was checked for short simulation times to verify it did not have a notable effect.

The following is a summary of the boundary and initial conditions used.

Temperature

- All domains initialized with: $T = 800°C$
- Quartz crucible outer wall: $T = 1100°C$
- Domain interfaces are continuous.

Flow

- Melt domain initialized with zero flow velocity.

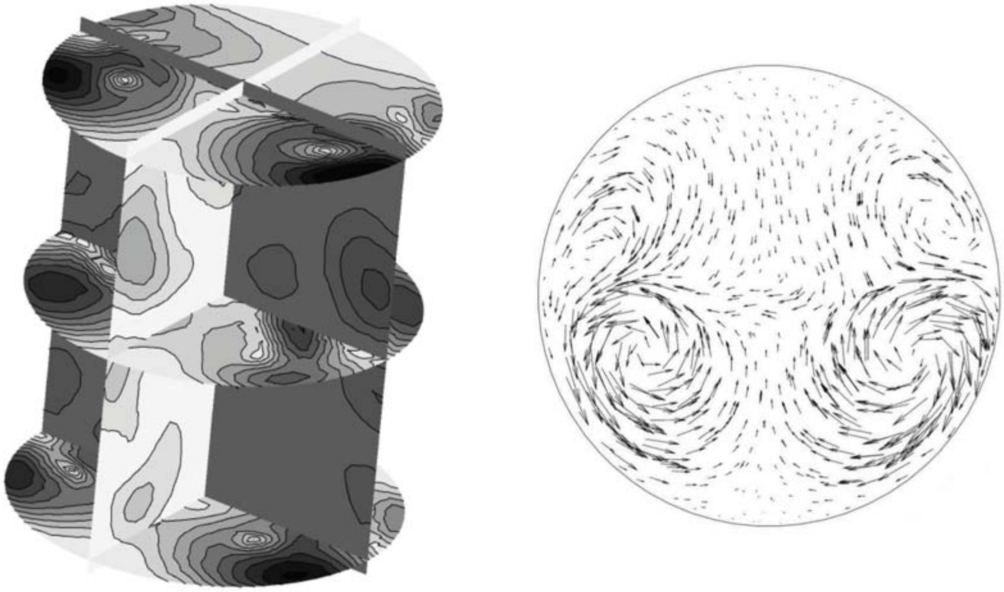

Figure 3.25: The plot on the left shows the velocity intensity through the melt volume. The dark areas represent stronger flows. Strong flow is evident in the radial tangential slices. Only weak intensity is visible in the axial planes. The vector plot on the right shows the velocity vectors and magnitude around the dissolution interface. The strong tangential and radial flows are evident.

- No slip boundary condition presumed along the melt edges: $v_r = v_\varphi = v_z = 0$

Concentration

- Melt is initialized as pure germanium.
- Dissolution boundary at fixed concentration determined by the following equation for silicon mass fraction: $c_{dis} = 1-(1.05513\times10^{-8}T^3-3.446005\times10^{-5}T^2+0.038741T-14.749675)$ (this equation is calculated from the phase diagram).
- Zero flux is assumed along the quartz-melt boundaries.

With the above conditions, a solution with and without the applied magnetic field was obtained. The solution without magnetic field exhibits the predicted behavior. The concentration profile evolves like a diffusion dominated system. There is weak flow structure around the interface but it does not seem to strongly affect the transport in the system, diffusion remains dominant.

With the application of the magnetic field, the flow structure in the melt is significantly altered. Strong flow structure develops in the radial-azimuthal plane while

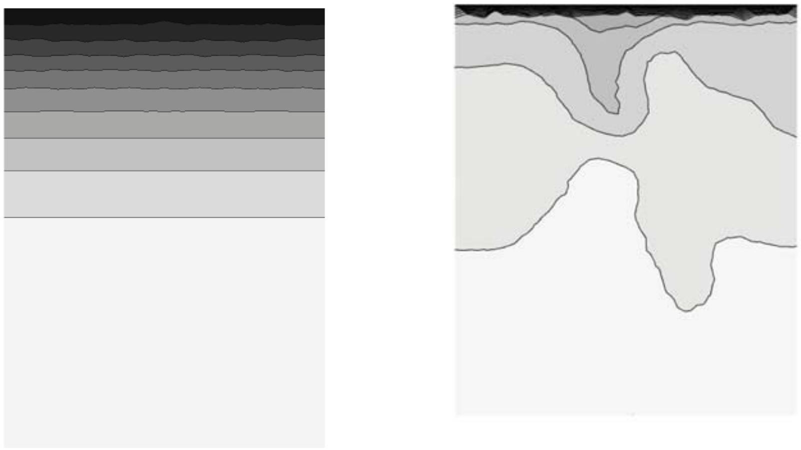

Figure 3.26: The plot on the left shows the concentration in the system modeled without the applied field. The diffusion dominated behavior is apparent. There is some weak disruption to the concentration isolines due to weak flow around the interface. The plot on the right shows the concentration field when the field is applied. The mixing of silicon towards the center of the melt is evident. The low concentration gradients in the center of the dissolution interface will slow dissolution. The high gradients near the crucible edge will accelerate dissolution.

weak flow structure remains in the axial direction. The flow is illustrated in Figure 3.25. The strengthened flow serves to mix silicon away from the edges of the crucible and towards the center of the melt. The concentration field reflects this, with steep concentration gradients at the edge of the dissolution interface near the crucible wall and shallow concentration gradients around the center of the interface. This can be seen in Figure 3.26.

The shape of concentration field will drive accelerated dissolution around the interface edges and lead to the interface observed in the experiments. However, the flow structure present in the model evolved significantly with time and does not appear to be a stable structure. The accuracy of the flows are not certain. The radial concentration profile the flow structure generates does not fully match the observed experimental result. Based on the model, it would be expected that the silicon concentration should be higher in the center of the melt. This was not observed in the differentially etched samples. The distribution of the needle structure indicating the presence of silicon was radially uniform. This can be seen in Figure 3.23.

In the model with no applied field, the centerline concentration profile exhibits a diffusion dominated shape. This is illustrated in Figure 3.27. With the application of

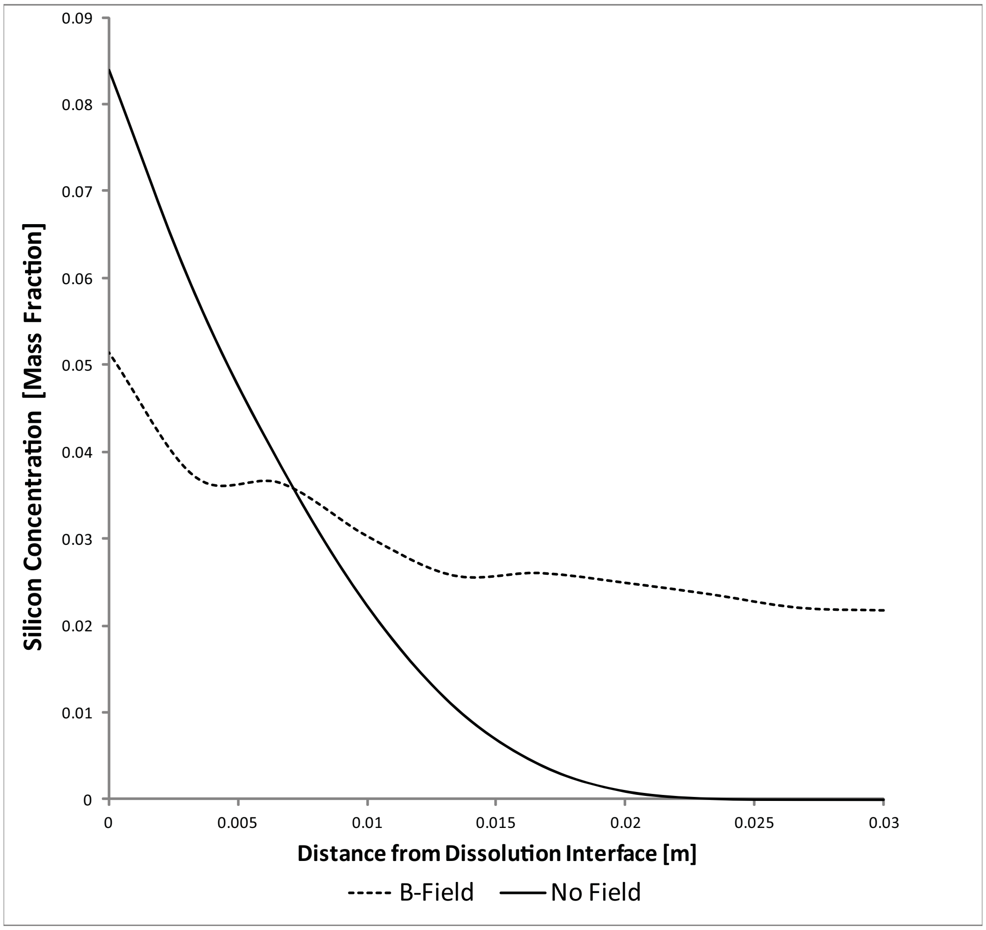

Figure 3.27: The concentration profiles from the model with and without magnetic field are overlaid. The application of the magnetic field has increased the distance that silicon has been transported into the melt.

the field this shape becomes significantly flattened and the silicon now extends further into the melt due to the additional mixing. The further extent of the silicon into the melt is seen in the experimental results. This is illustrated in the EDS compositional profiles shown in Figure 3.28.

The application of a static magnetic field inducing mixing in the melt is contrary to what has been observed in other systems. The application of a static field is usually associated with suppression of convective flows. Instead, the application of the field is seen to enhance mixing in the melt. This seems to be a characteristic of the SiGe system and may be related to the strength of the buoyancy flows in the material system.

The additional mixing incurred by applying a static magnetic field could be useful

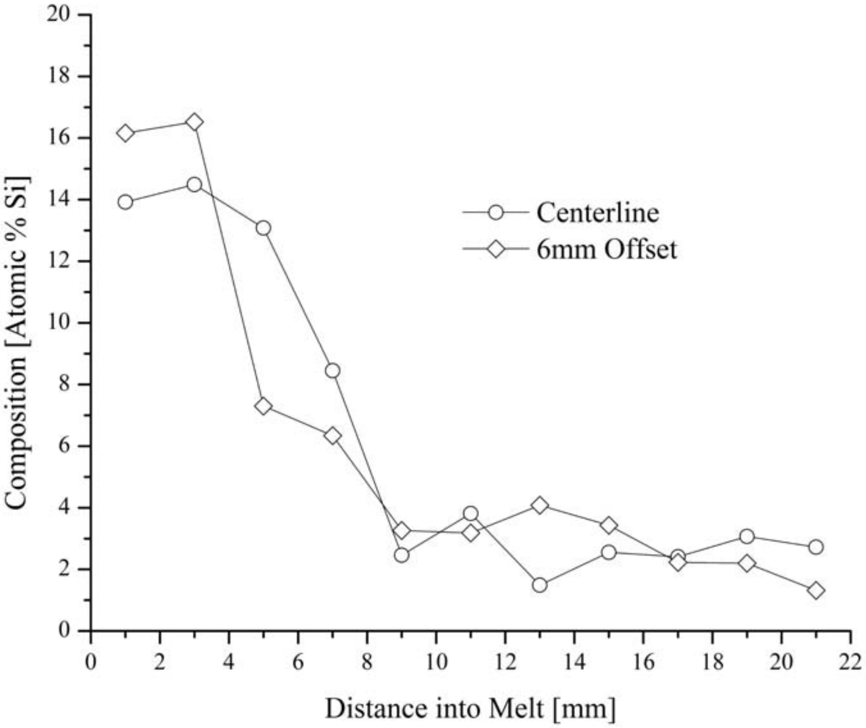

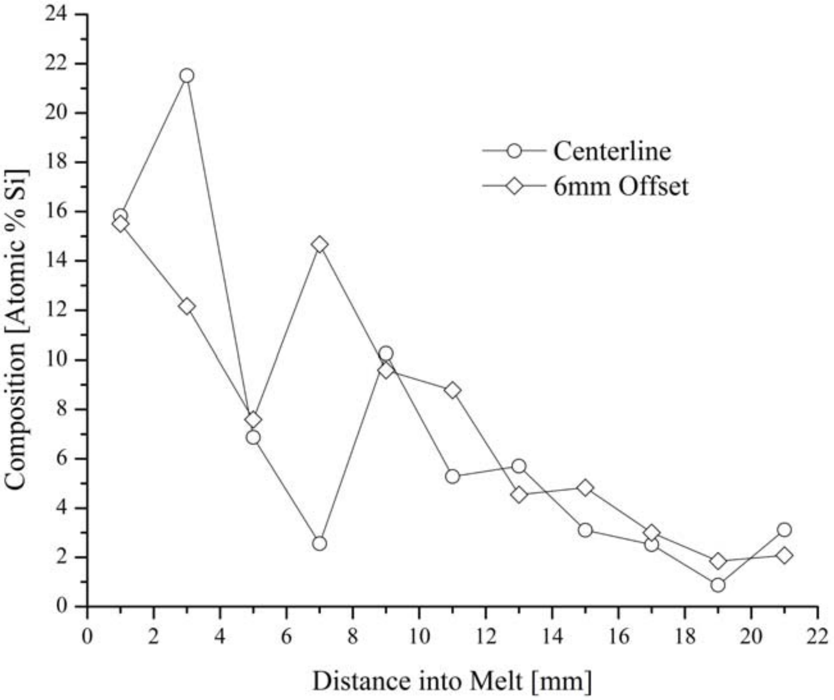

Figure 3.28: The plot at the top shows the EDS concentration profiles for the sample processed without magnetic field. The plot on the bottom shows the EDS concentration profiles for the sample processed with magnetic field. The silicon extent into the melt has increased with application of the magnetic field. Both profiles are for samples processed for 20 minutes.

in LPD growth of SiGe. The enhanced transport could lead to faster growth rates and improved interface shape. In melt replenishment Czochralski, this effect could also be utilized. Silicon introduced into the edge of the melt near the crucible wall would potentially experience additional mixing towards the center of the melt. This is where the crystal is being pulled. The mixing of silicon from the crucible wall to the growth interface is desirable in this technique as the crucible edge will be the most convenient place to replenish the melt with silicon. It is possible that the additional flow may adversely affect the stability of the growth interface.

The simulations conducted show that the magnetic field body force can act to enhance mixing in the system. The flow structure present in the melt seems to be enhanced by the magnetic field. The radial and azimuthal flows become strengthened mixing silicon away from the crucible wall. This would drive higher dissolution rates at the crucible wall.

3.5.2 Additional Treatments of Configuration C under Static Magnetic Field

The following work was primarily undertaken by A. Kidess and F. Micheghal with the author collaborating. The same system as examined in the previous section was studied using different numerical methods to better handle the body forces in the melt. The work with A. Kidess was published in the Journal of Crystal Growth and Fluid Dynamics and Materials Processing [30, 34]. The work with F. Micheghal was published in TWMS Journal of Applied and Engineering Mathematics [28].

As the flow structure obtained in the previous section was determined to be unsatisfactory, more in depth numerical analysis was undertaken. Two methods were followed. The OpenFOAM and FASTEST finite volume solvers were utilized by A. Kidess to solve for the flow structure and concentration field. A finite element approach was utilized by F. Micheghal to obtain the flow structure and concentration field.

3.5.2.1 Finite Volume Approach

From the simulations by A. Kidess, the following results were achieved. The system was again shown to reach thermal equilibrium quickly, less than 90 seconds. The concentration profiles exhibited a more stable profile. Both with and without the magnetic field, the system proceeded diffusion dominated. Curvature in the concentration field did develop near the dissolution interface with the application of the magnetic field. This is shown in Figure 3.29.

The flow is significantly affected by the application of the magnetic field. It is noted that the flow velocity directions are more effected than the flow intensity. These changes are attributable to the magnetic body forces. Stable flow is visible close to the dissolution interface in thin Hartmann layers that have formed. Outside the Hartmann layer, there is no visible flow. This is illustrated in Figure 3.30.

The model predicts very small radial concentration gradients. Even within the flow structure, the radial concentration gradients are low. There is a very slight trend to higher axial concentration gradients near the crucible wall when compared to the center. However, this effect is very small and not sufficient to explain the change in the dissolution interface observed experimentally when the magnetic field is applied. While the correct trend is predicted, the magnitude is too small to adequately predict the experimental phenomena.

To try to replicate the experimental results, an artificial heat leak was added to the top of the source material. This would cause non-isothermal conditions and possibly enhance the mixing around the crucible walls. While the experiments were designed to minimize temperature gradients, the system was modeled with a large heat loss in order to see if heat loss could contribute to the dissolution observed in the system. In examining the experimental design, the most probable location for heat loss would be the top of source. The sample is lowered into the furnace from the top which requires there is no insulation directly above the source. This is counteracted by sealing the sample in its crucible under vacuum. There is a thick region of vacuum above the source which should limit heat transfer. However, this is still the most likely location for a heat leak.

A large heat leak of $420W$ was applied which corresponded to a temperature reduction of $30K$ at the top of the source. The computed concentration profiles show significant change over the results from the simulations with no heat leak. There is a stronger radial concentration gradient at the dissolution interface. This can be seen in Figure 3.31. However, there is little to no change in the concentration profile between the simulation with the heat leak and no applied magnetic field and the simulation with the heat leak and the magnetic field applied. This would suggest that this does not reflect the experimental conditions. A strong dependence on field was noted in the experiments.

The flow field exhibits the same dependence on magnetic field that was seen in

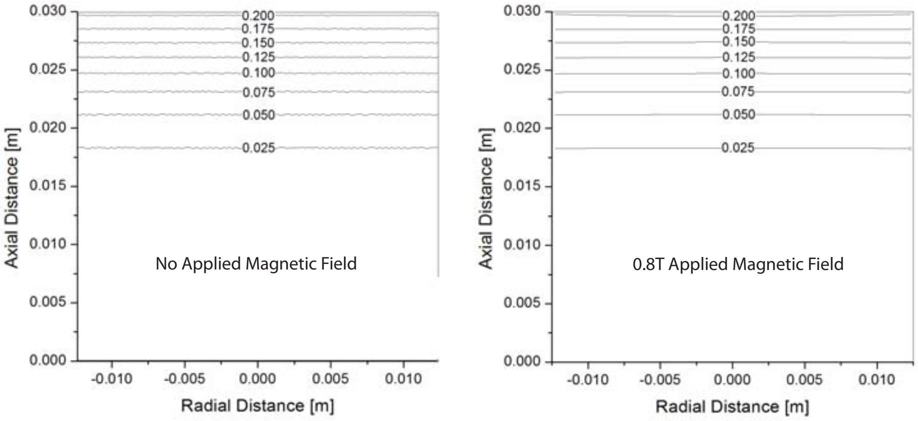

Figure 3.29: The concentration isolines with and without the applied magnetic field are shown. The calculated fields are very similar to one another. There is a very slight curvature in the concentration isolines near the dissolution interface.

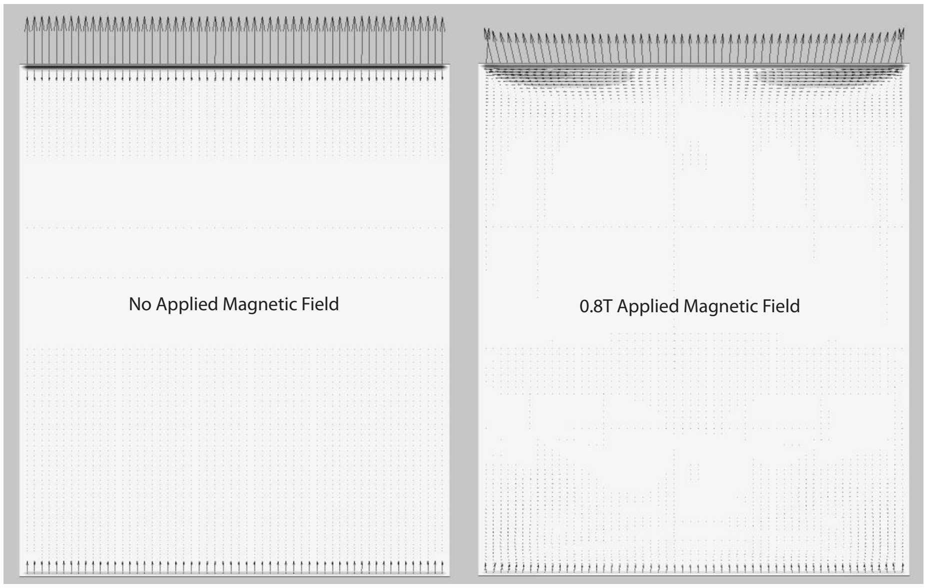

Figure 3.30: The flow fields with and without the applied magnetic field are shown. The velocity field develops thin Hartmann layers with the application of the magnetic field. The flow in the melt is isolated to this layer.

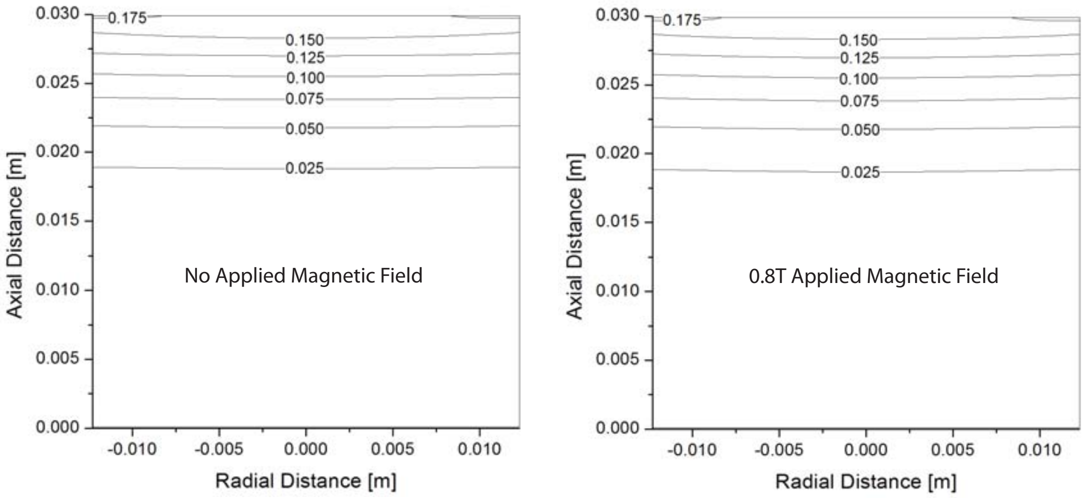

Figure 3.31: The concentration isolines are plotted with and without the applied magnetic field. The results above are from the model with the $420W$ heat leak. The additional curvature of the isolines compared to the plots in Figure 3.29 is apparent. However, the application of the field does not significantly alter the concentration distribution.

the simulations without the heat leak. These results coupled with the large heat leak required to create the effect, would seem to indicate that the experiments are in fact very close to isothermal. This implies that there is a phenomena that is not included in the present model. One possible effect is thermoelectric convection. Thermoelectric currents promote convection in the melt and can change the shape of the interface and the concentration field [23, 108]. In systems with a Hartmann number close to that found in the dissolution system, enhancement of the azimuthal flow has been observed [109]. Further investigation of this effect in the dissolution system is warranted.

Another interesting aspect of this work was to test the sensitivity of the results to the solutal expansion coefficient. The physical parameters of the SiGe system are not well investigated and the solutal buoyancy referenced has not been rigorously investigated. Simulations were conducted with two values of solutal expansion coefficient, 5.3×10^{-3} and 0.17×10^{-3}. Visibly the produced concentration profiles are identical, both with and without the applied magnetic field. The plots of the concentration profiles are shown in Figure 3.32. This supports the conclusion that the transport in the system is proceeding as a diffusion dominated system. The diffusion dominated behavior is due to the silicon stabilizing the melt against convection. This work shows that there is a range of solutal body force magnitude that could generate the diffusion

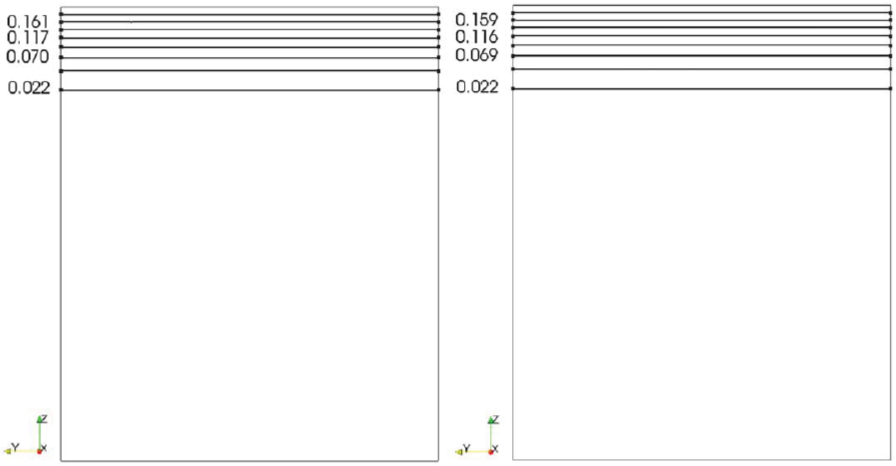

Figure 3.32: The concentration isolines are plotted for two systems without applied magnetic field. The plot on the left is the model with the solutal expansion coefficient set at 5.3×10^{-3}. The plot on the right is the model with the solutal expansion coefficient set at 1.7×10^{-3}. The plots are virtually identical.

dominated behavior. The solutal Grashof number relates the strength of the solutal buoyancy force to the viscous forces and scales with the solutal expansion coefficient. Therefore it is likely that only a change in the magnitude of the solutal buoyancy may affect the diffusion dominated behavior observed.

3.5.2.2 Finite Element Approach

In the work by F. Micheghal, the flow structure in the melt is better resolved. In this work, a finite element based numerical solution was implemented. The same set of field equations and the same physical parameters were utilized.

In the case with no magnetic field, a weak flow structure of one large convection cell forms. The melt rises up the crucible wall and down the center of the melt. The cell is characterized by stronger flows by the crucible wall and more diffuse flow in the center of the melt. The strong flow near the edge of the crucible will be incident on the dissolution interface and mix dissolved silicon away from this region and towards the center of the melt. However, as indicated from the concentration profile the flow structure in the melt is very weak and does not significantly contribute to transport. The concentration profiles in the melt are flat and the transport proceeds like a diffusion dominated system. This is illustrated in Figure 3.33.

With the introduction of the magnetic field, the flows near the crucible wall are

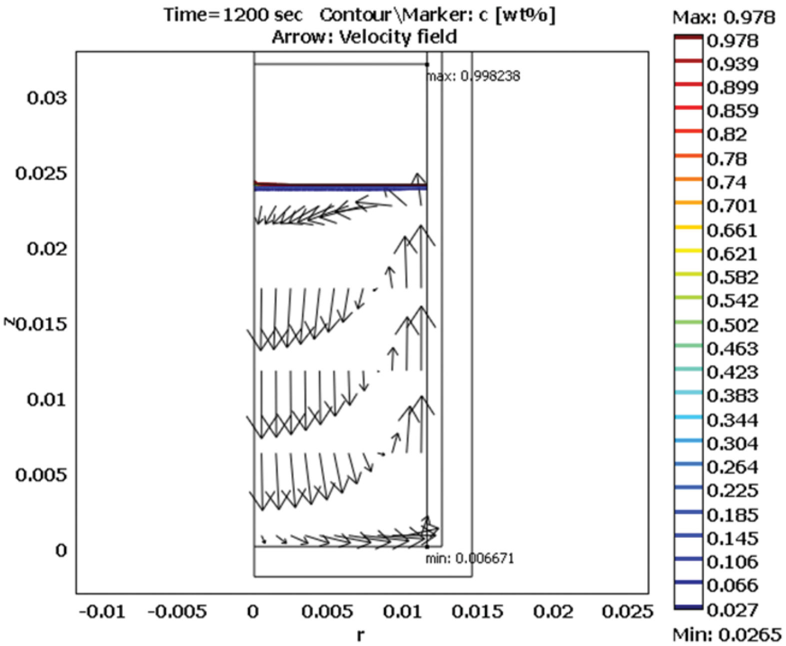

Figure 3.33: The above plot is after 30 minutes of simulation time with no applied magnetic field. The vector plot indicates the flow field and the isolines indicate the concentration.

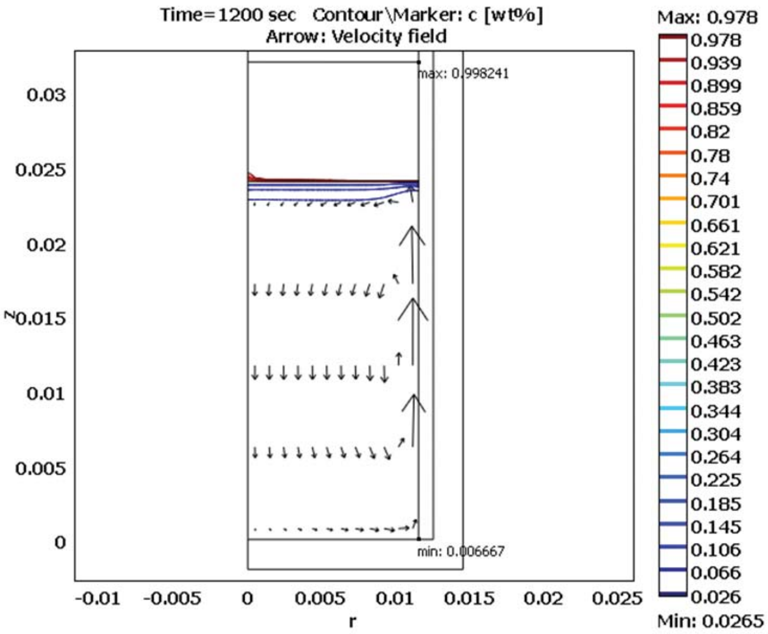

Figure 3.34: The above plot is after 30 minutes of simulation time with a $0.8T$ applied magnetic field. The vector plot indicates the flow field and the isolines indicate the concentration.

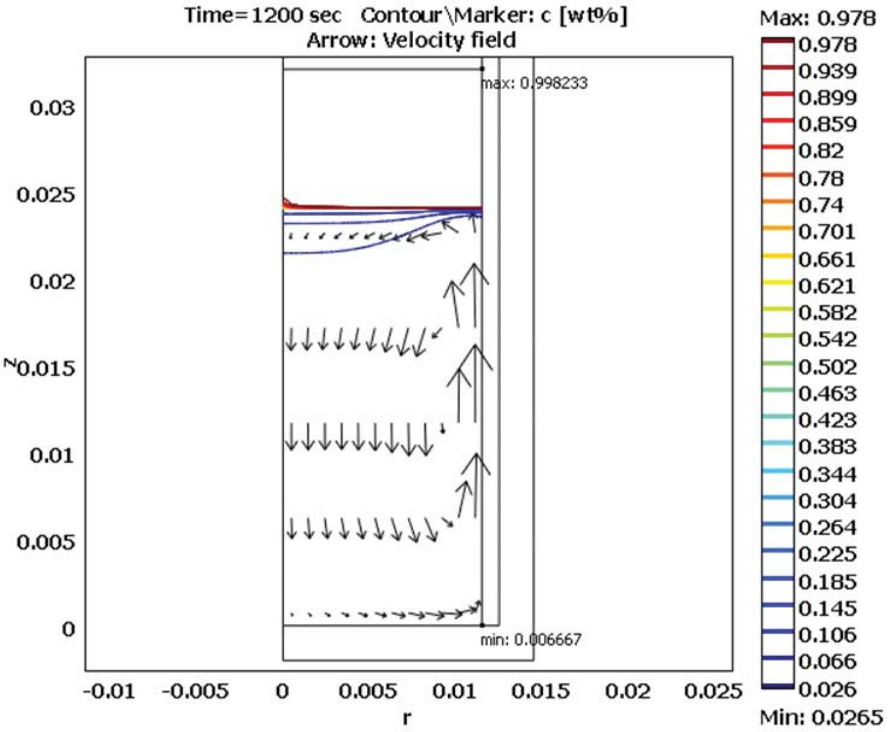

Figure 3.35: The above plot is after 30 minutes of simulation time with a $0.3T$ applied magnetic field. The vector plot indicates the flow field and the isolines indicate the concentration.

enhanced. This can be seen in Figure 3.34. These flows now have a visible effect on the concentration profile. They serve to mix silicon away from the crucible wall and into the center of the melt. In the center of the melt, the transport still precedes diffusion dominated as the flow structure in the center remains weak. The mixing of silicon away from the crucible wall will increase the concentration gradient in this area and drive more dissolution. This will lead to the interface shape observed in the experimental work.

The magnetic field level was varied to see the effect on the flow structure and concentration field. At the $0.8T$ field level, the upwards flow is confined very close to the crucible wall and the concentration gradients at the dissolution interface are similarly confined at the crucible wall. This type of scenario should produce a very similar dissolution interface shape to that observed in the experimental results. By reducing the field to $0.3T$, the flow is not as confined to the crucible wall. This is shown in Figure 3.35. The resulting concentration gradients are spread out further into the dissolution interface as well. This should spread the areas of high dissolution further towards the center of the melt. The $0.8T$ field level model results agree better with the observed experiment results than the $0.3T$ field level.

In the experiments conducted, the areas of high dissolution were localized to the crucible wall. The areas of diffusion dominated transport are characterized by low radial composition gradients and the shift from the diffusion regime to the convective regime is well delineated in the model results. This compares well with the experimental results where the extra dissolution was very localized.

It appears from this work that the magnetic field is enhancing the already present weak flow structure present in the melt. This enhanced flow results in the altered dissolution interface shape observed. The evolution of the dissolution interface could not be replicated in this work. This is possibly due to the fact that the domains considered were 2-D axisymmetic and as such tangential flows were not considered. The inclusion of the tangential flows may allow for more accurate modeling of the dissolution interface evolution.

3.5.3 Dissolution Height

The dissolution trend observed in Configuration C should be directly related to the diffusion coefficient as it has been shown that the system appears to precede diffusion dominated. To extract information about the diffusion coefficient, a numerical model of the experimental setup was solved using the ANSYS CFX finite volume solver. A variety of parameters were varied in order to gain a good fit with the experimental values.

As the system is presumed diffusion dominated, the flow field and temperature field were not solved. Only the species mass transport by diffusion was considered. The dissolution interface was taken as an equilibrium saturation condition for the experiment temperature of $1100°C$. The other boundaries were considered impermeable. The model was calculated for the $30min$ experiment time. The intermediate time steps were recorded for comparison to the experimental data. The concentration profile from the model was integrated to determine a mass of dissolved silicon in the melt. This can then be correlated to a dissolved height.

The results show a much different phenomena than that observed in the experiments. During the initial stages of the model, the dissolution is rapid as the concentration gradients are high. As time proceeds this rate slows. The experimental results seem to be missing this initial period of high dissolution. The diffusion coeffi-

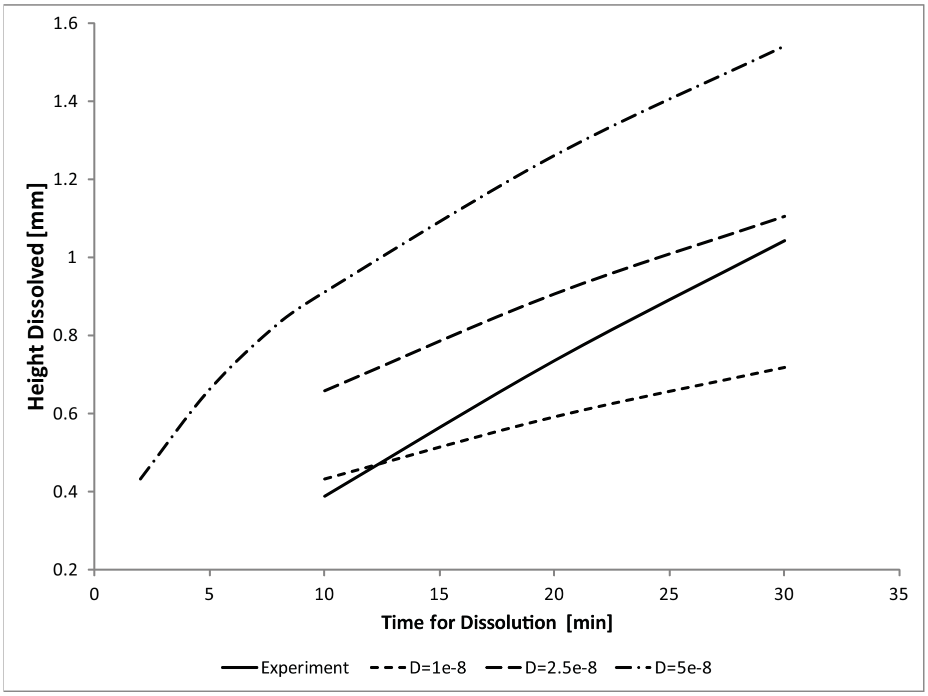

Figure 3.36: The graph above illustrates the dependance of the dissolution height curve on the diffusion coefficient. The inability to match the experimental results with the current diffusion dominated model is apparent.

cient used in the model effects the slope of the dissolution curve after the initial high dissolution period. It does not markedly affect the initial quick dissolution. Diffusion coefficients of 5.0×10^{-8}, 2.5×10^{-8} and 1.0×10^{-8} m^2/s were modeled. The results are shown in Figure 3.36.

The slope of the curve generated with the 5.0×10^{-8} m^2/s diffusion coefficient follows the experimental result almost perfectly. However, the model experiences the time of quick dissolution and is thus offset from the experimental data. In order to explain this difference, two additional effects were considered in the model. Firstly, solutal buoyancy was introduced and the flow field solved.

The introduction of the solutal buoyancy into the model generated weak flow around the interface. This added additional transport into the system and as a result the dissolution heights increased slightly. This did not affect the overall shape or slope of the curves. It only offset the curve to a slightly higher dissolution height. This is shown in Figure 3.15.

Another effect explored was a time dependant dissolution interface. The dissolution interface boundary condition was initially set to the saturation concentration value. Rather than have the interface saturated at the beginning of the simulation, the interface was started at zero concentration and then linearly ramped to reach the saturation concentration. This may account for non-equilibrium effects rate limiting the silicon dissolution into the melt during the initial phases of dissolution. It was found that a long ramp period was required in order to get a curve that approximated the experimental curve, on the order of 15min. An example of this is shown in Figure 3.16. While the modeled curve does not perfectly align with the experimental data, this does show that a rate limiting effect at the beginning of the experimental time could produce a dissolution height curve similar to the one observed.

This illustrates that the initial dissolution period may include non-equilibrium effects not included in this continuum model. This may be important to understanding the silicon transport rate in the melt. To investigate this further, the effective diffusion coefficients for the Configuration C experiments conducted with and without magnetic field were determined. These were calculated by using the analytical solution of Fick's Law in one dimension. This is shown in Equation 3.1.

$$C_{Si} = C_{Si(x=0)} \mathrm{erfc}\left(\frac{x}{2\sqrt{Dt}}\right) \tag{3.1}$$

The concentration profile defined by this equation can be used to calculate the total silicon dissolved and therefore the height of silicon source dissolved. Using an iterative solve process, the height dissolved from the analytical equation is matched to the experimental result by varying the diffusion coefficient. These results are plotted in Figure 3.37.

The effective diffusion coefficient increases with time in both the experiments conducted with and without applied magnetic field. In the experiments conducted with the magnetic field, the effective diffusion coefficient seems to be asymptotically approaching a diffusion coefficient of approximately $2.5\times10^{-8}\ m^2/s$. The experiments conducted without the magnetic field could also be displaying the same behavior, but the time frame of the experiments are not sufficient to show the trend to the same extent as the experiments conducted with the magnetic field. This phenomena is not unexpected as the diffusion coefficient will vary with silicon composition in the melt. At the start of the experiment there is no silicon in the melt. As the experiment proceeds the silicon concentration increases as does the effective diffusion coefficient. Therefore it would seem that the diffusion coefficient is increasing to a stabilized value with increasing silicon concentration. The application of the magnetic field

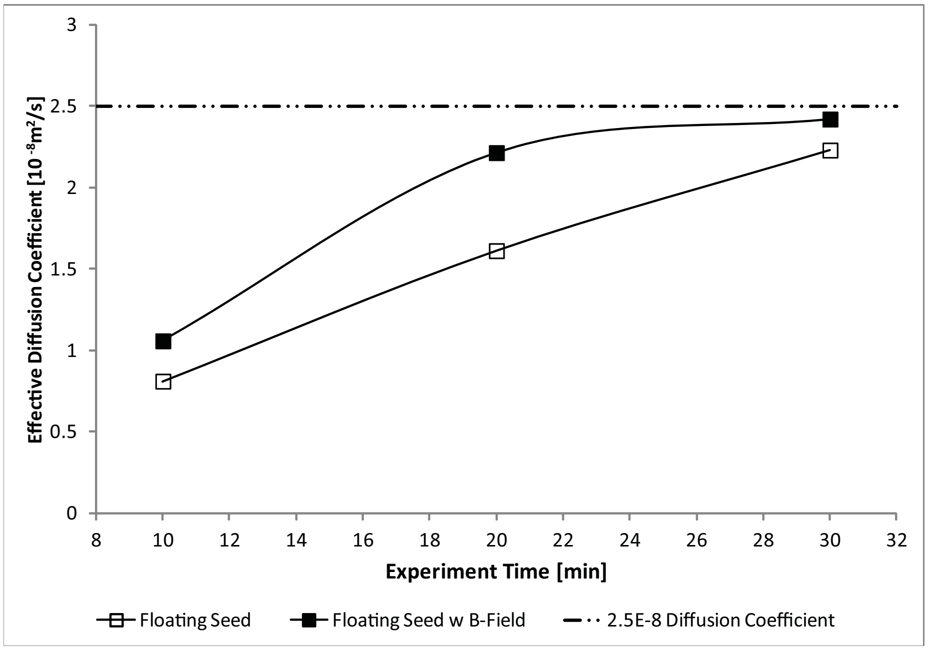

Figure 3.37: The graph above shows the variation of the calculated effective diffusion coefficient for Configuration C with and without applied magnetic field.

would seem to accelerate the rate at which the effective diffusion coefficient increases. This is likely due to modification of the flow structure around the interface.

3.6 Small Diameter Dissolution Experiments

The following work was presented at the International Symposium on Physical Sciences in Space and published in the Journal of Physics CS [29]

In order to extract more information about the diffusion coefficient a series of experiments were performed in small diameter crucibles. The smaller diameter helps to suppress flow in the melt and ensure that mass transport is diffusion dominated. The crucible setup was similar to the experimental configurations presented earlier with two key differences. The diameter was reduced to $8mm$ and the length of the melt was increased to $60mm$. The increase in height was to ensure that little to no silicon would reach the bottom of the melt and dissolution rate should be independent of melt composition.

Diameters smaller than $8mm$ were trialed but the surface tension of the melt caused technical issues. The source material would often not wet to the melt or voids would form in the melt column. This could be overcome by applying a force to the top

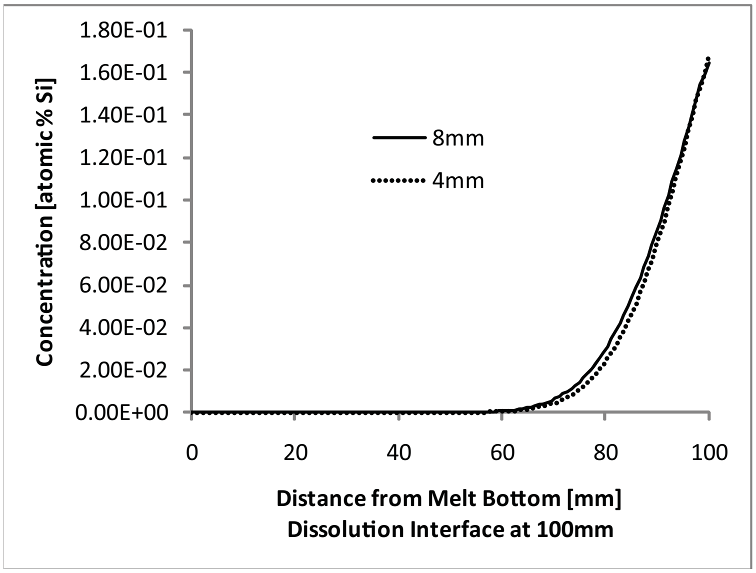

Figure 3.38: The plot above shows the modeled concentration profile for two crucible configurations. Both the $4mm$ and $8mm$ diameter crucibles are shown.

of the source to ensure proper contact, however this introduces significant complexity to the system. Both the $4mm$ and the $8mm$ system were modeled to investigate the effect of diameter on transport. The model included diffusive mass transport and solutal buoyancy flows. The resulting composition profiles from the two modeled systems were virtually identical. As such, it was decided to use the $8mm$ system. This result is shown in Figure 3.38.

Two material configurations were utilized, one with the silicon at the top of the melt and one with the silicon at the bottom of the melt. Rather than examine the time dependence of the dissolution heights, these experiments examined the temperature dependence of the dissolution height. Three temperatures were used for this work, $1000°C$, $1050°C$ and $1100°C$. The experiments were all conducted for one hour.

The dissolution heights obtained for the samples with the silicon at the top of the melt show a weak trend to higher dissolution with temperature. This is shown in Figure 3.39. As the experiments were conducted in an isothermal environment, this would indicate that the diffusion coefficient also weakly depends on temperature. The trend is not well resolved in this set of experiments. Additional experiments to better resolve this effect are required. It is possible that allowing the samples to dissolve for a longer time would help this issue. However, the length of the melt was calculated based on the one hour experiment time. If the experiment time is to be increased, the length of the melt would need to increase in order to keep the condition of the

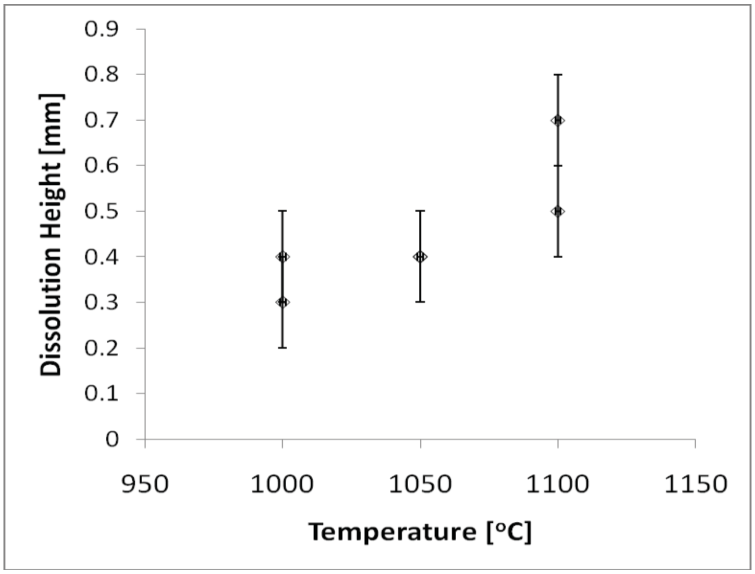

Figure 3.39: The graph above shows the dissolved height versus temperature. A trend to higher dissolution with higher temperature is evident. However, for the experiments conducted this dependance is weak.

bottom of the melt having minimal silicon concentration or this requirement would need to be relaxed.

The samples with the silicon at the bottom of the melt exhibited drastically different behavior. This is illustrated in Figure 3.40. The silicon was completely dissolved during the experiment time. This provides a good illustration of the dependence of the dissolution rate on the orientation of the interface. The formation of strong solutal buoyancy flows seems unaffected by the smaller diameter crucible utilized.

Another reason for using a long column of melt was to extract composition information to compare to diffusion dominated composition profiles. The composition information could then be used to directly measure the diffusion coefficient. However, due to the low concentration of silicon in the melt, there is significant thermal expansion of the germanium rich melt during solidification. The presence of silicon in the melt helps to reduce this effect. The thermal expansion causes the melt column to be significantly disturbed during cooling due to cracking of the crucible and subsequent melt leakage. This makes it impossible to reliably correlate a position in the quenched material to a position in the melt column. It may be necessary to use a shear cell type arrangement to obtain this information. This would eliminate the uncertainty about the material's position in the melt column. In addition, it would help to reduce macro-segregation issues.

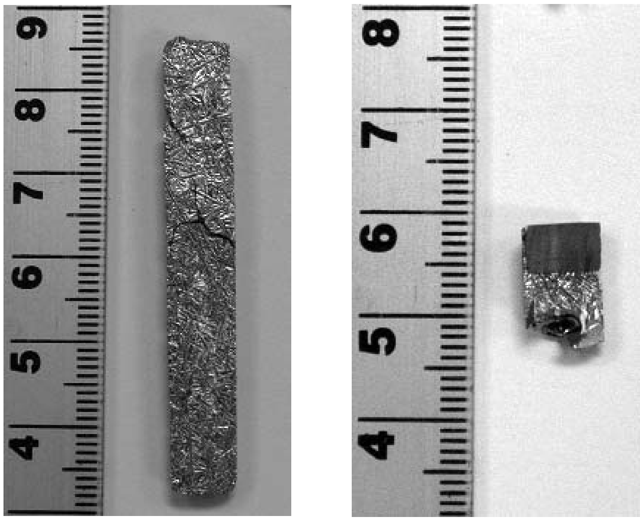

Figure 3.40: Material samples processed in the 8mm crucible. The sample on the left had the silicon at the bottom of the melt. The source material has completely dissolved and there is a strong uniform needle structure though the melt. This sample has been differentially etched. The needle structure indicates the presence of silicon in the melt. The sample on the right had the silicon at the top of the melt. There has been little dissolution and little transport of silicon into the melt. The lack of transport is evidenced by the lack of needle structure in the melt. This sample was also differentially etched.

Chapter 4

Liquid Phase Diffusion Growth of SiGe

4.1 Introduction

The Liquid Phase Diffusion, LPD, growth process will be examined in this section under a variety of flow and thermal conditions. Through variation of these parameters, better understanding of their impact on the growth process will be determined. In the LPD system, growth takes place under equilibrium conditions. There is no translation or temperature change required to initiate growth. A strong temperature gradient is imposed over the growth cell. Solute is introduced at the hot end of the growth cell and a concentration gradient develops across the growth cell. The concentration gradient induces transport from the hot end to the cold end of the growth cell. As solute is transported to the cooler end of the growth cell, the solution will surpass its saturation concentration and growth will initiate through precipitation.

In silicon germanium growth by LPD, it is expected that any modified flow structure should have significant impact on the growth process. SiGe growth by LPD proceeds as a diffusion dominated process. The buoyancy of the silicon species in the melt effectively damps convective flow and the transport is predominantly by diffusion. As diffusive transport is a relatively slow process, any additional mass transport induced by the modified flow conditions should have an observable effect on the growth rate.

4.2 Experimental Design

The LPD system setup is very simple. The material is loaded in the crucible in three pieces. From top to bottom, there is a silicon source, germanium melt material, and a germanium seed. The silicon seeds used were $25mm$ diameter single crystal cylinders $5mm$ thick. The germanium melt material was a $25mm$ diameter cylinder of polycrystalline material, $30mm$ thick. The germanium seed was a $25mm$ diameter single crystal cylinder $15mm$ thick. All the material is contained in a clear fused quartz crucible.

The silicon source was sized to ensure that not all silicon would be dissolved during the growth period. The silicon utilized was single crystal. This was only because that was the material readily available commercially. Polycrystal material could also have been utilized. Commercial zone refined germanium was cored into $25mm$ diameter cylinders to produce the melt zone material. The cylinders were $30mm$ long, setting the melt zone depth as the same. This length was used to keep the experimental time to the desired length. Single crystal germanium seed material was utilized to allow for single crystal growth. The Ge seed's length was $15mm$. This was necessary to allow for melt back of the seed during the heating period prior to the start of growth. All materials were chemically cleaned and etched. The starting materials were all 99.999% pure.

The materials were placed in a cleaned quartz crucible. The crucible is placed in a quartz ampoule which is then evacuated $1 \times 10^{-3} Pa$. The ampoule is then sealed with a quartz plug welded in place. The crucible is spaced from the bottom of the ampoule with a thin piece of quartz tube. A diagram of a typical growth ampoule is shown in Figure 4.1.

The crucible is placed in a three zone DC furnace and heated to the growth temperature. The growth temperature environment is a steep, minimum $25°C/cm$, temperature gradient over the crucible. The crucible is positioned such that the seed melts back between 1 and $5mm$. There is a range of melt back due to the curvature of the initial interface. Depending on the temperature gradient, the dissolution interface is at a temperature of between 1030 and $1100°C$. Once growth temperature is reached, the system is left for the desired amount of growth time then slowly ramped down to room temperature.

In the baseline system used in this work, the temperature gradient used was steeper than that used in previous LPD work at the University of Victoria. The

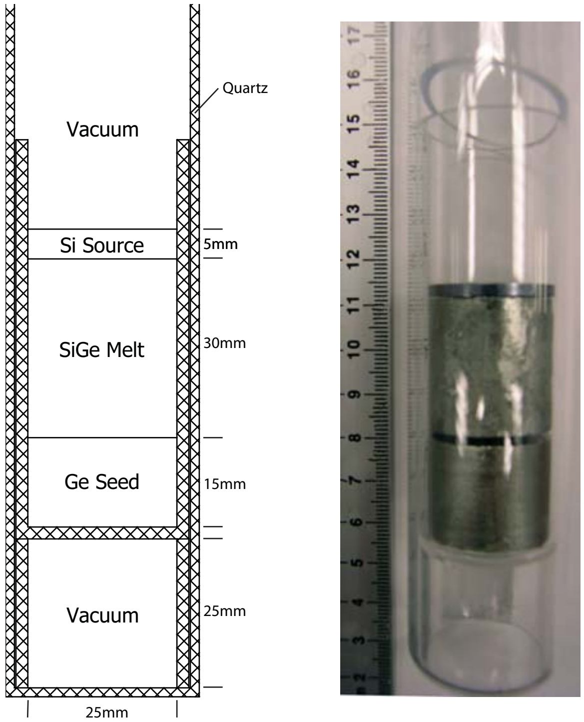

Figure 4.1: The arrangement of a typical LPD experiment is diagrammed above. A photo of a typical sealed ampoule is also shown. The ampoule pictured was used for finding the initial growth interface. The source material in the photo is smaller than the source used in the experimental setup.

use of a smaller bore furnace along with a redesigned insulation package allowed for the increased gradient. The gradient used was approximately $40°C/cm$. The steeper gradient should drive a faster growth process.

The experiments here were not processed for a full LPD growth run. Instead the experiments were shortened to approximately one half the normal experimental time. It was expected that the growth may proceed somewhat faster than in previous experiments. In addition, it was desirable to have both a section of quenched melt and grown crystal for analysis. The experiments were allowed to run for 72 hours rather than a full LPD run of 144 hours.

The furnace system used in this work was a new platform for LPD. This was necessary as the platform had to fit inside the static magnetic field generator. In addition, the furnace was wrapped with magnet coils to produce a rotating magnetic field. The platform was also equipped to translate the sample. The addition of all these features required a new furnace platform be designed and built. In the process of these modifications, the thermal profile of the system was improved and the higher

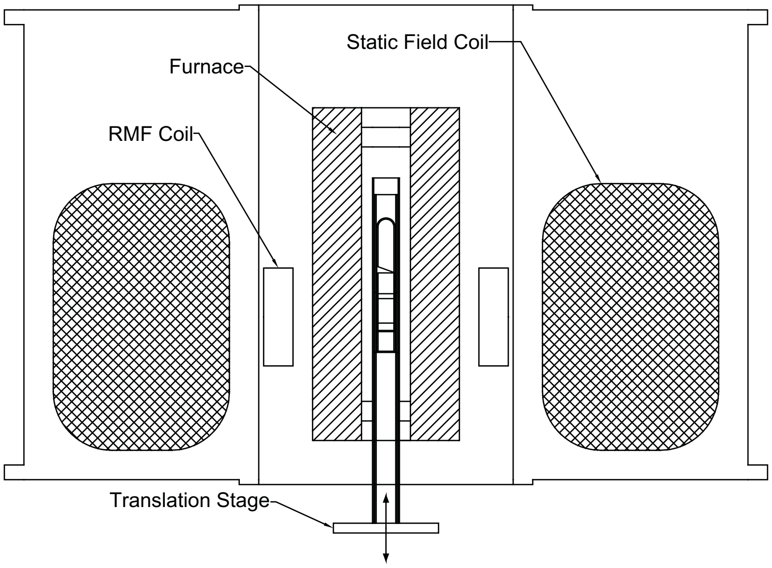

Figure 4.2: The arrangement of the LPD growth system is diagrammed above. The uniform region of the static field is centered on the crucible growth position. The peak strength of the rotating magnetic field is similarly centered on the crucible. The rotating field coils are supported independently of the furnace as the interaction of the static and rotating fields produces vibration. The furnace is supported inside the magnet on a stand equipped with a stage that can translate the crucible in the axial direction.

growth zone gradients were achieved.

The platform was designed such that all of these stimuli could be applied at once to the sample being processed. The various configurations possible are illustrated in Figure 4.2. In this work, the following combinations were investigated.

- Baseline LPD, no applied stimuli
- $0.4T$ Static Magnetic Field
- $5mT$ at $40Hz$ Rotating Magnetic Field
- Combined Static and Rotating Magnetic Fields
- Translated LPD

In addition, modification of the thermal field around the seed was investigated by inserting a graphite block underneath the seed. The details of each case will be discussed in the following sections.

The processed samples were sectioned axially into two bulk halves and a $2mm$ thick centerline wafer. The centerline wafer was polished and mounted for obtaining EDS composition profiles. One bulk half was polished and then etched to reveal structure. More information on the analysis is given in Section 3.2.1.

The following work has been presented by the author in four articles [24, 36–38].

4.3 Baseline Experiments

The Baseline LPD experiments were conducted following the same basic procedure as in previous work [25]. The samples exhibited the expected phenomena. The etched materials' melt region exhibited the presence of silicon, although with much less macro-segregation than that observed in the dissolution experiments. In the dissolution experiments, the presence of silicon was indicated by the presence of a needle structure in the melt region. Here the needle structure is not as evident. In the LPD experiments, the samples are slowly cooled after growth and not quenched as was the case for the Dissolution Experiments. This likely explains the change in structure. The presence of silicon causes the grain size in the melt's polycrystalline structure to be very small. In regions of low silicon concentration, the grain size is significantly enlarged.

The dissolution interface shows increased dissolution around the crucible edge and relatively flat shape through the center of the melt. This can be seen in Figure 4.3. This is typical of what has been seen in previous LPD work. The seed has melted back between 9 and $11mm$. The initial seed-solution interface is concave to the melt as was observed in previous LPD experiments. This interface is visible in the the differentially etched segments. However, it is only apparent at certain angles of reflection and as such is indicated by a dark line in Figure 4.3. The curvature has been significantly reduced over the original LPD setup. This is likely due to the improved thermal characteristics of the new LPD growth platform.

Over the 72 hour duration of growth, there has been approximately $5mm$ of single crystal growth. After this point, the quenched melt is visible. The exact same platform parameters, including crucible position, will be utilized in the other experiments conducted. A plot of the EDS composition profiles of these samples is shown in Figure 4.4. The approximate extent of growth for each sample is indicated on the plot. There is less scatter present in these EDS composition results when compared with the results obtained for the dissolution experiments. This is due to a more controlled

Figure 4.3: The photo above shows the differentially etched sections of the baseline experiment samples. Baseline Experiment #1 is on the left and Baseline Experiment #2 is on the right. The initial growth interface and the extent of single crystal growth is indicated on the photos as dark lines.

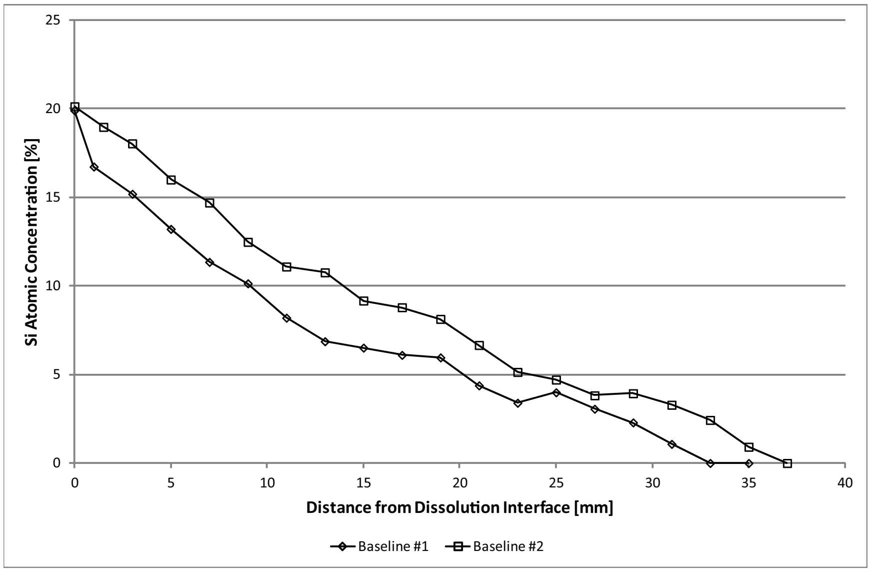

Figure 4.4: The EDS composition profiles for the Baseline Experiments are shown above. The "Distance from the Dissolution Interface" is referenced to the point in the center of the sample where the material transitions from silicon source to the melt. This is used as the reference as it is a feature easily visible on the samples when viewed in the SEM.

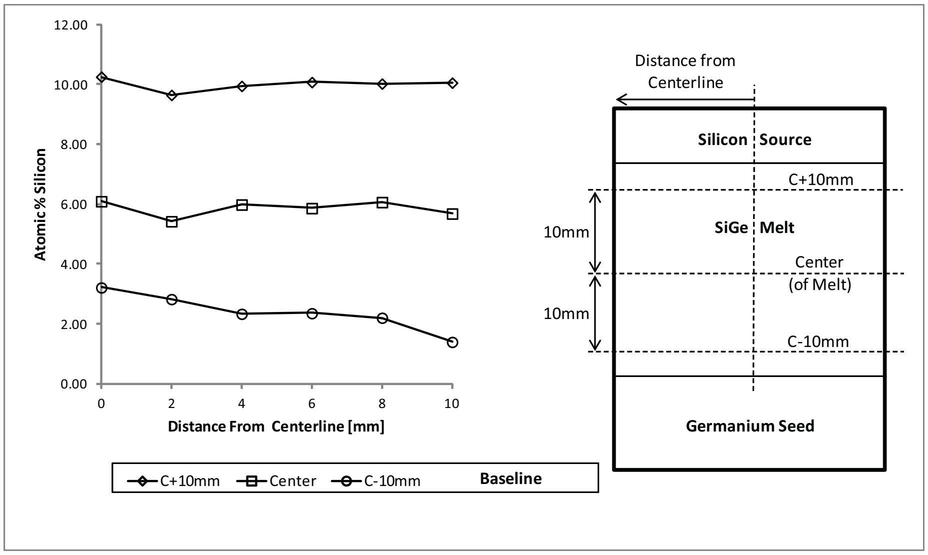

Figure 4.5: The graph above shows the radial composition profiles in the melt for the Baseline Experiment #1 sample. The position of the three profile lines are diagrammed on the right. The center of the melt is determined for each sample by measuring the distance from the dissolution to the bottom of the sample. This measure is then halved to determine the center point.

cooling process for the LPD samples. The level of macro-segregation is far lower. The radial composition plots are shown in Figure 4.5. The radial composition profiles in the samples show a relatively flat profile throughout the melt.

4.4 Static Magnetic Field Experiments

The application of a static magnetic field to the LPD growth of silicon germanium has been previously examined numerically [26, 110]. This was primarily aimed at altering the transport through the melt to affect the curvature of the growth interface. In previous experimental work, it was observed that the growth interface shape evolves from concave to the melt at the start of growth, to convex into the melt near the end of the growth process. The desired interface shape is flat. Controlling the transport of silicon through the melt could aid in establishing, then maintaining, a flat growth interface.

In this work, a static field of $0.4T$ was applied. This was the optimal value found in the previous numerical work. The field level is consistent with previous crystal growth experiments where a magnetic field has been used to suppress flow in the

Figure 4.6: The photo above shows the samples processed with the static magnetic field applied. The sample on the left is the Static Field Experiment #1 and the sample on the right is the Static Field Experiment #2. In the Static Field Experiment #2 sample, there was no melt back of the seed and the melt did not fully wet the germanium seed. In Static Field Experiment #1, the seed did wet and there was minor melt back of the seed. The initial growth interface and the limit of silicon in the melt is indicated on the sample by the dark lines overlaid.

melt. All the other experimental parameters used for the baseline experiments were repeated.

Examining the differentially etched samples and then comparing to the baseline samples, a dramatic difference is noted. The samples etched for structure are shown in Figure 4.6. The extent of silicon transport into the melt has been dramatically reduced. In fact, the silicon has not transported far enough into the melt to initiate growth on the germanium seed. The dissolution and transport mechanisms have been dramatically slowed over the baseline experiments. This is contrary to what was seen in the dissolution experiments. However in the case of LPD, the flow structure in the melt would be expected to be quite different from the Dissolution Experiments due to the thermal gradient present.

In the Dissolution Experiments conducted under isothermal conditions, the magnetic field seemed to act to strengthen weak flow structures increasing transport. In the LPD system, as there is stronger flow structure present due to the thermal gra-

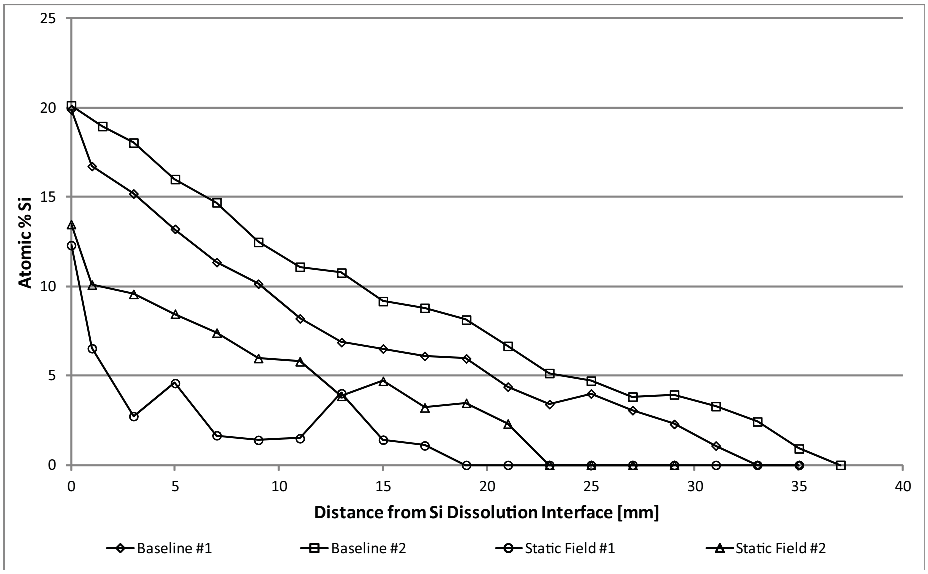

Figure 4.7: The plots above compare the composition measurements in the baseline samples with the samples processed with the static magnetic field applied. The reduced transport of silicon in the melt is clearly visible.

dient, the magnetic field is acting to suppress silicon transport. It would appear that the stronger flow structure in the LPD system is being suppressed by the magnetic field.

The lack of silicon dissolution in the samples processed with the magnetic field is also evident from the amount of silicon source remaining. The silicon source shows very little dissolved height. In addition, it does not show accelerated dissolution around the crucible walls. This is evident in the photos in Figure 4.6. Instead, the samples exhibit a very flat dissolution interface. This is again contrary to the phenomena seen in the Dissolution Experiments. There, the application of the magnetic field increased the dissolution of silicon around the crucible edge. The additional dissolution observed in these experiments was explained by increased tangential and radial flows. In the LPD samples, the opposite is observed. The reduction of radial and tangential flows is leading to a flatter dissolution interface. This is consistent with the behavior expected from the application of a magnetic field. A static magnetic field is often used to suppress convective flow in a growth system.

Another effect is also evident from the differential etched samples. The application of the magnetic field has had a strong impact on the thermal field in the system. There has been much less, only approximately $1mm$, of melt back of the germanium seed. This shows that the temperature gradient in the sample has been altered. The

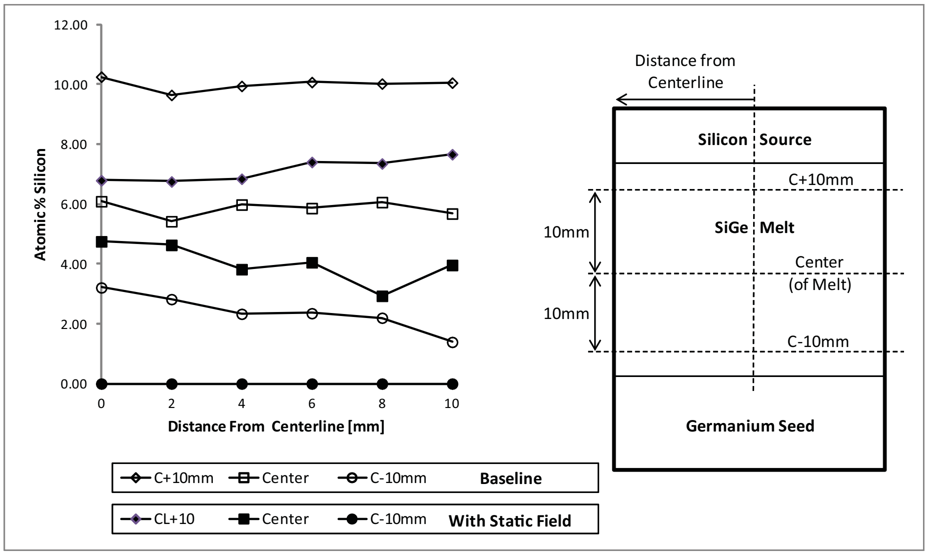

Figure 4.8: The plot above shows the radial composition profiles in the Baseline #1 sample and the Static Field #1 sample. The position of the profiles is shown for reference. The baseline and the static field experiments exhibit similar flat profiles.

temperatures around the seed have been lowered resulting in the initial growth interface moving towards the source. The initial growth interface is entirely determined by the thermal field. The seed melts back such that the interface is along an isotherm corresponding to the melting temperature of germanium, approximately 940°C.

The EDS composition profiles of the processed samples support the observations from the etched samples. A plot of these profiles is shown in Figure 4.7. The baseline experiments exhibit the expected steadily increasing compositional profile. The samples processed with the magnetic field show a much quicker drop to zero silicon concentration. The profile shows that no silicon has yet transported to the region around the growth interface.

Radial composition profiles were also analyzed. A plot of the radial composition profiles is shown in Figure 4.8. The composition profiles of both the baseline and static magnetic field samples were found to be relatively flat. This is counter to what was seen in the previous LPD work and seems to be a product of the improved thermal characteristics of the new LPD system. In the previous LPD experiments, the growth interface shape evolved with time due to curvature in the radial composition profiles. Silicon was transported faster through the center of the melt. This phenomenon was not seen in the current work.

Also evident on the composition profiles is that the application of the magnetic field seems to have lowered the saturation composition around the dissolution interface. A shift in the thermal field has already been noted around the growth interface. If the dissolution interface has also been shifted to a lower temperature this could also explain the drop in the saturation composition. The LPD ampoule is supported in the furnace by a quartz tube that runs completely through the furnace. This results in a path for heat loss directly above and below the crucible. While steps have been taken to reduce heat loss at these locations, some loss will occur.

A numerical model of the LPD system, considering fluid flow and heat loss top and bottom was examined. Thermally driven convection was considered in one version of the model and removed in another. This was to qualitatively examine the effect of the magnetic field on the thermal field in the system. It is expected that the application of the magnetic field will suppress the convective fluid flow. The modeling shows that in such a situation, with heat leaks top and bottom, the removal of the flow field does indeed induce the effects seen in the experimental results. The dissolution interface moves to a lower temperature and the temperature around the growth interface shifts as well. Plots of the modeled thermal field with and without convection are shown in Figure 4.9.

In this configuration, it may be necessary to further insulate the crucible to eliminate any heat leaks. Currently the top and bottom of the crucible are insulated by a thick vacuum zone. Therefore the primary means of heat loss would be by radiation. More consideration of possible heat loss may be necessary in future growth work. It would also be possible to simply reposition the crucible in the thermal gradient according to the new flow conditions in the melt.

It appears that the application of a static magnetic field to the LPD process may not be beneficial to the growth process. The radial composition profiles in the melt did not show any significant improvement with the application of the field. The application of the field did, however, significantly slow the transport of silicon into the melt and would therefore reduce the growth rate. A general problem in solution growth of material is that the growth rates are slow when compared to melt growth. Additionally slowing the growth process with no clear benefit does not seem to justify the expense and complexity of processing samples under a static magnetic field. It may be possible that, under different experimental conditions, the static field could improve the growth conditions. As has been noted here, the magnetic field does seem to effectively suppress the convective flow in the melt.

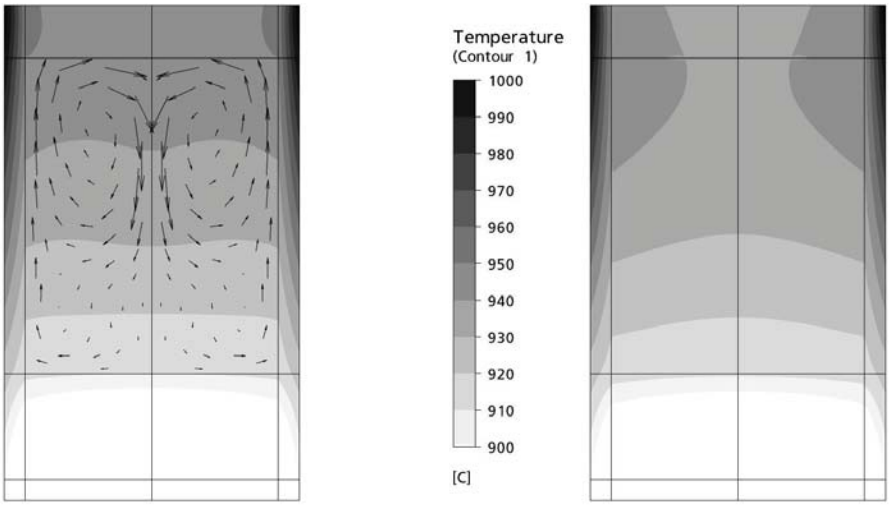

Figure 4.9: The above are plots of the thermal fields with and without the thermal buoyancy force considered. In the plot on the left, the temperature field is calculated with the buoyancy force. A vector plot of the flow field in the melt is overlaid. In the plot on the right, the thermal field has been calculated with no flow in the melt. Boundary conditions consistent with the LPD process were utilized in both cases. The shift of the thermal field with the change in the flow field is evident. This is similar to the effect expected with the static magnetic field being applied. The static magnetic field should suppress convective flow in the melt.

4.5 Rotating Magnetic Field Experiments

The application of a rotating magnetic field to LPD growth of silicon germanium has been previously examined numerically [26]. This work was, primarily aimed at altering the transport through the melt to affect the curvature of the growth interface. The application of a rotating magnetic field should induce extra mixing in the melt, aiding the transport of silicon.

A magnetic field strength of $5mT$ rotating at $40Hz$ was utilized for this work. These parameters were selected based on the modeling work. This combination of field strength and frequency was shown to help reduce radial composition gradients in the melt. The rotating field is centered on the middle of the melt zone. The field rotates around the vertical axis with the field lines aligned with the crucible's radial-tangential plane. The field is generated by three sets of electromagnets. The coils in each set are placed directly opposite one another. Each set is rotated 60° from the other. A three phase sine wave signal is produced to drive each set of electromagnets. Each phase of the signal is offset 120°. This produces a rotating field at the frequency

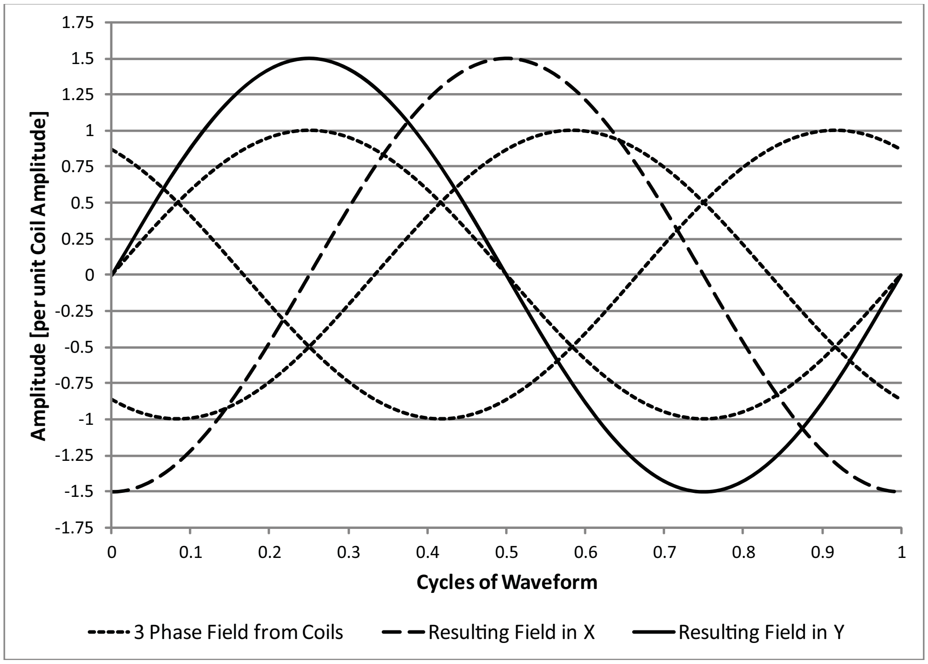

Figure 4.10: The chart above illustrates the creation of the rotating magnetic field from three sets of magnet coils. Each set of coils is connected in series across a bridge of a delta 3-phase load arrangement. The changing field from each set of coils is shown as the "Three Phase Field from Coils" lines. Each sine wave is the field created by one set of coils. The resultant field in the X and Y directions created by the coil fields are also plotted. The directions X and Y are defined as 90° from each other arbitrarily. The resulting fields in the X and Y directions are sine waves 90° out of phase. These fields result in a constant magnitude field with a vector that rotates in a complete circle over a cycle of the driving waveforms.

of the three phase signal. This is illustrated in Figure 4.10

Examining the differentially etched samples, it is clear that there is a change in structure over the baseline samples. The samples processed with the RMF are shown in Figure 4.11. There has been additional melt back of the germanium seed. This is the opposite effect to what was observed when the static magnetic field was applied. In this case, the additional mixing induced by the rotating field has shifted the thermal field downwards. This in turn has moved the initial growth interface towards the bottom of the crucible. In fact, the shift in temperature has caused a complete melt back of the seed in the center of the crucible. The edges of the seed are still intact.

There is also a significant increase in the amount of material grown during the experiments. In the baseline experiments, approximately $5mm$ of growth was observed.

Figure 4.11: The samples processed with the rotating magnetic field are shown above. The sample on the left is Rotating Field Experiment #1 and on the right is the Rotating Field Experiment #2. In the Rotating Field Sample #2, the seed completely melted back and has made the growth material highly polycrystalline. In the Rotating Field Experiment #1 sample, the seed did not melt back fully around the edge of the crucible. This resulted in regions of single crystal being produced around the outside of the crucible. The initial growth interface and extent of growth are indicated by dark lines on the photo.

In the experiments conducted with the rotating magnetic field, approximately $15mm$ of growth was observed. This is a significant increase in growth rate and indicates that the silicon transport in the melt has been enhanced.

The grown material is not fully single crystal. Due to the full melt back of the seed in the center of the crucible, polycrystalline growth is initiated in the crucible center. However, single crystal growth is initiated at the sides of the crucible from the remaining germanium seed crystal. These single crystal grains preferentially grow out the polycrystalline section. This is easily visible on the differentially etched sample.

The silicon dissolution interface is modified as well. The center of the dissolution interface is convex into the source material. The sides of the source exhibit accelerated dissolution similar to that observed in the baseline samples. The additional dissolution in the center of the melt is likely due to the modified flow structure in the melt caused

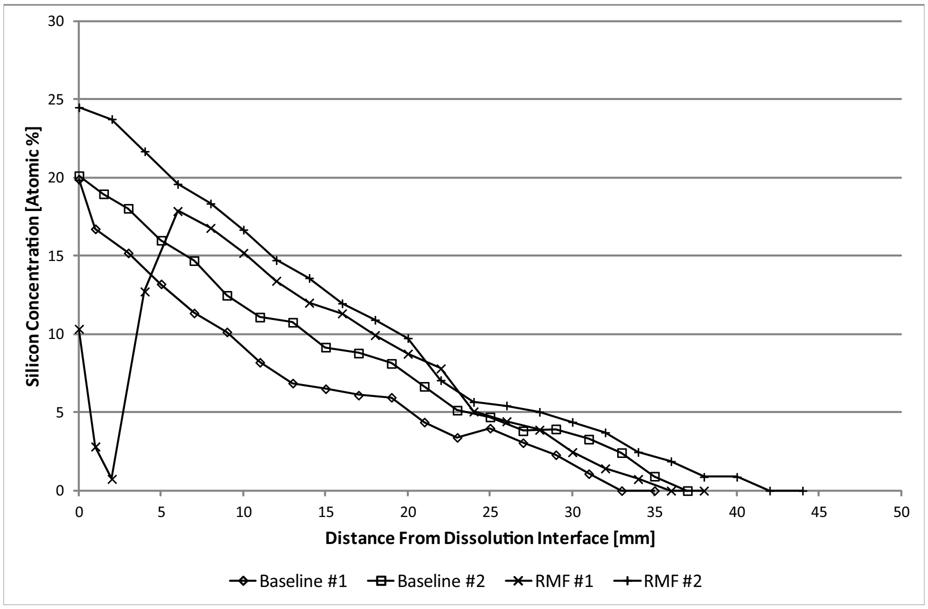

Figure 4.12: The plots above show the axial composition profiles of the baseline samples and the samples processed with the rotating magnetic field. The trend to more transport of silicon with the application of the rotating magnetic field is evident.

by the application of the rotating magnetic field.

The EDS composition profiles through the center of the material reflect these observations. This data is plotted in Figure 4.12. The silicon transport is enhanced when compared to the baseline condition. The extent of silicon transport also shows the additional melt back of the seed. In addition, the profile shows that the saturation composition at the dissolution interface has increased over the baseline experiments. This indicates that the temperature gradient has been shifted in this region of the crucible as well. As in the case of the static magnetic field, the alteration in flow structure is the likely cause of the change in the thermal field. The thermal field in the melt seems to be very sensitive to changes in flow structure. The change in the thermal field could most easily be accounted for by repositioning the crucible in the furnace to reflect the flow conditions imposed by the magnetic field.

The radial composition profiles of the sample show the same flat profile seen in the baseline samples. This can be seen in the plot in Figure 4.13. The application of the magnetic field has not affected the radial distribution of silicon. Instead, the transport is enhanced in the axial direction while the uniform distribution in the radial direction is maintained.

The rotating magnetic field has a strong effect on the transport in the melt. The

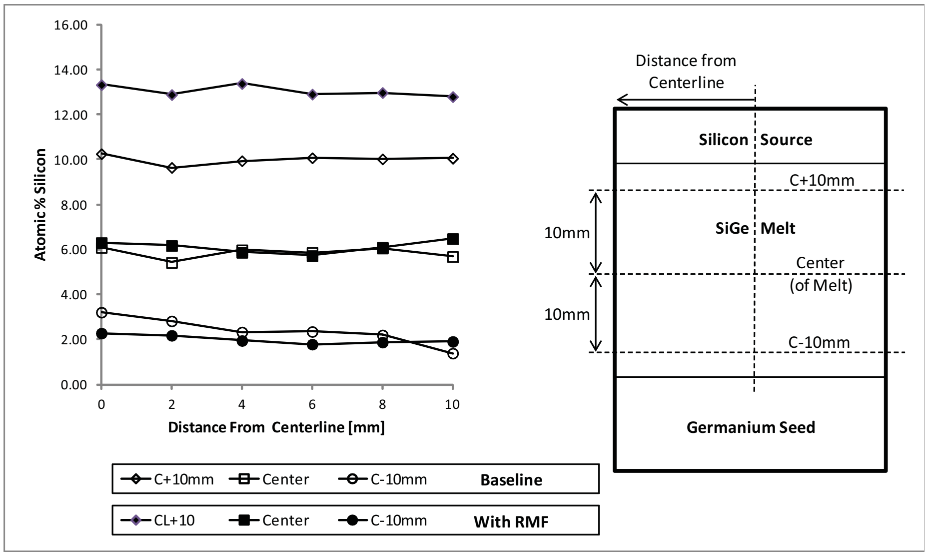

Figure 4.13: The plot above shows the radial composition profiles in the baseline samples and the samples processed with the rotating magnetic field. The profiles are very close in shape and both exhibit low composition gradients.

addition of the rotating magnetic field to the system has significantly improved the transport of silicon and increased the growth rate. This is the opposite effect to that seen with application of the static magnetic field where the growth rate was significantly slowed. Both applied fields strongly affected the thermal field in the system. In the design of future experiments, it will be imperative to consider this coupling between the application of the magnetic field and the thermal field.

The use of a rotating magnetic field may be of significant benefit to LPD growth of silicon germanium. The increased transport could be used to significantly reduce the growth time required for a bulk crystal. In addition, the distance between the seed and source could be increased. The increased transport would keep growth times similar to those currently typical in LPD while allowing the growth of material at higher silicon compositions.

In addition to LPD, application of an RMF may have benefit in melt replenishment Czochralski growth. As the additional mixing did not significantly impact the radial composition profiles, the additional transport induced may not impact the stability of the growth interface. This could be useful in increasing the transport of silicon from the edge of the crucible, where silicon is being introduced, into the top center of the melt. The center of the melt, around the growth interface, is where rejected germanium from the growth process is causing the melt to become dilute in silicon requiring additional silicon to be introduced.

4.6 Combined Magnetic Field Experiments

The combined field effects of an applied rotating magnetic field along with a static magnetic field has been examined experimentally. A magnetic field of $5mT$ rotating at $40Hz$ was applied in the radial-tangential plane of the crucible while a $0.4T$ static axial field was applied. There was significant interaction between the rotating field coils and the static field generator. While the fields would ideally be perfectly perpendicular to one another, this is not possible in practice. As such the changing field in the rotating coils produces a force that vibrates the system. To mitigate this effect, the furnace was isolated from the rotating coils such that little vibration could be transferred.

The static magnetic field has been shown to suppress the flow structure in the melt. This reduces transport by convection. The rotating field induces tangential flow, essentially stirring the melt. The mixing induced by the rotating field has been shown to be advantageous in increasing the amount of silicon transported in the melt. By combining the effect of these fields, it was hoped that the reduced natural convection in the system caused by application of the static magnetic field would allow the mixing induced by the rotating magnetic field to more strongly affect silicon transport in the melt.

The differentially etched samples again show that the thermal field in the system has been significantly altered. The samples can be seen in Figure 4.14. The seed in this case has been completely melted back. This shows that the melting point of germanium has been shifted downwards outside the crucible. The new flow structure present in the melt is presumed to be the cause of this behavior. At the dissolution interface, a higher saturation concentration will be expected in keeping with the trend seen in the other field conditions.

There has been significantly more silicon dissolved in these experiments over the baseline experiments. This is clear from the amount of silicon source material remaining. The increase in dissolved silicon will partially be due to the higher temperature at the dissolution interface. In addition, it would appear that the flow in the melt has been enhanced speeding the dissolution of the silicon.

The structure of the material produced is polycrystalline with small grains. The grain size is typical of a melt solidified with a relatively high concentration of silicon. This was observed in the baseline experiments and the static magnetic field experi-

Figure 4.14: The samples above were processed with both the static magnetic field and the rotating magnetic field applied. The seed completely melted back resulting in growth starting with the material self-seeding around the crucible bottom. This has resulted in the material being highly polycrystalline.

ments. This would seem to imply that there has been significant transport of silicon into the melt.

The EDS composition profiles obtained for these samples support the above observations. The EDS data is plotted in Figure 4.15. There has been a significant increase in silicon transport into the melt over the baseline experiments. In addition, there has been an increase in transport over the rotating field alone experiments. The addition of the static magnetic field would seem to have enhanced the effect of the rotating field, thereby increasing the transport of silicon into the melt. The suppression of the convective flow in the melt would seem to have enhanced the effect of the rotating magnetic field.

As there is no seed interface in these experiments, due to the complete melt back of the seed, the melt has self seeded at the bottom of the crucible. The spontaneous nucleation at the bottom of the crucible is indicated by the small grained polycrystalline material observed. Other indications of this process are visible on the composition profiles. At the bottom of the profiles, near the bottom of the crucible, there is a distinct upturn in the composition profiles. This implies that the melt in this area was significantly super-cooled prior to solidification. This would be consistent with

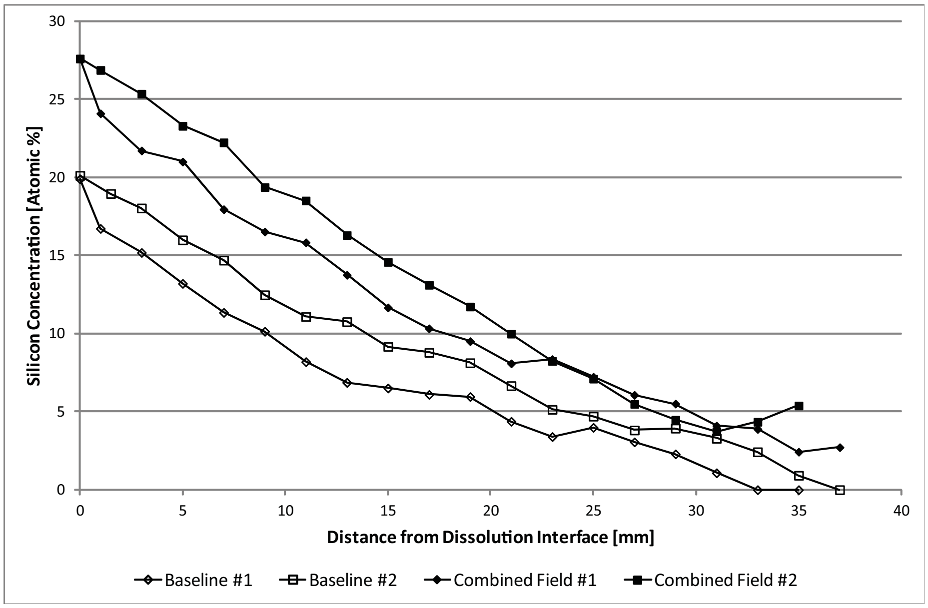

Figure 4.15: The centerline composition profiles for the samples processed with both static and rotating magnetic fields as well as the data for the baseline experiments are plotted above. The trend to higher silicon transport over the baseline samples with the application of the magnetic fields is evident. The upturn in composition at the bottom of the melt is a distinct feature. This is most likely due to the self-seeding process in this area of the melt.

a lack of nucleation sites due to the absence of the seed crystal. The melt is constitutionally super-cooled by the transported silicon. Once the melt is super-cooled spontaneous nucleation can take place. The melt in general has to be super-cooled further to initiate self-seeding than if there was a seed present. This is due to the extra energy of formation associated with spontaneous nucleation. Once nucleation has taken place, solidification takes place with less super-cooling of the melt as there are lattice sites to facilitate growth. The self seeding process would explain the upturn in the measured composition profiles while the growth after nucleation leads to the fine grain polycrystalline structure.

The radial composition profiles show the same flat distribution seen under the previous experimental conditions. This can be seen in Figure 4.16. Given the independence of the radial composition profiles from the magnetic field conditions applied to the experiments, it would appear that the altered flow structure in the melt has little impact on radial composition. It would seem that other factors in the experimental design are more critical. Strong radial composition gradients were noted in the previous LPD apparatus. The current experimental design improved the thermal

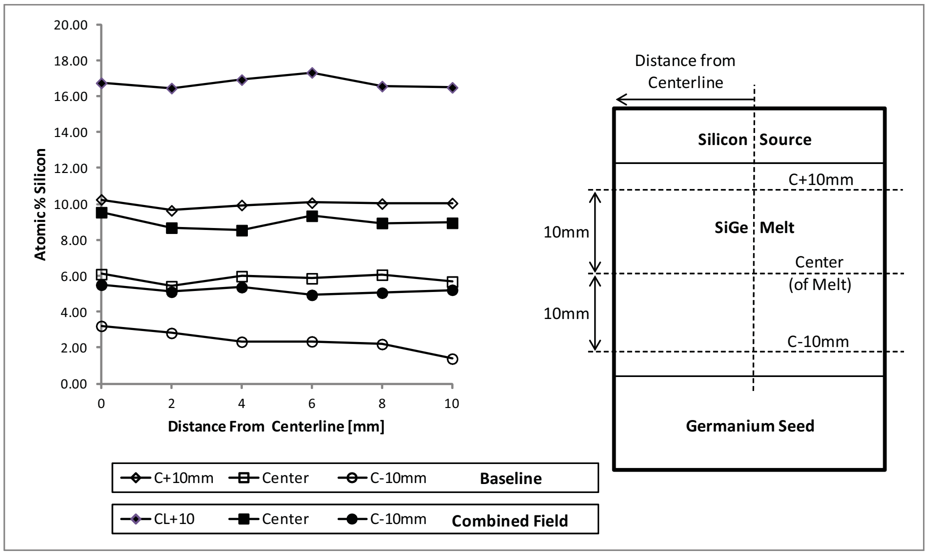

Figure 4.16: The plots above compare the radial composition profiles of the Combined Field Experiment #1 with the Baseline Experiment #1. Both samples exhibit a similar flat profile.

design over the original system. The change in thermal design seems to have had the most impact on the radial composition profiles. The change to a flat profile was noted in every configuration including the baseline samples.

While the combined field did increase the silicon transport in the melt over the rotating field alone, it did not provide as significant increase as was seen with the rotating field alone over the baseline. This is illustrated in Figure 4.17. The use of a static magnetic field generator adds significant complexity to a crystal growth experiment. The entire apparatus must fit within the bore of the field coil. In addition, the waste heat from the furnace must be managed such that the bore of the magnetic is not significantly heated. Creating a strong field, such as the one used in this work, requires a superconductor based field coil that requires cryogenic temperatures for operation. There is significant cost for integrating a field generator like this into a crystal growth process. Therefore, the benefit from the applied field must be significant.

A rotating magnetic field generator, with lower field strength, is much easier to implement. As can be seen in the composition profiles, a significant improvement in silicon transport is noted with the application of the rotating magnetic field over the baseline experiments. Adding the static magnetic field on top of this only produces a minor increase over the rotating field alone. It would seem that this small increase

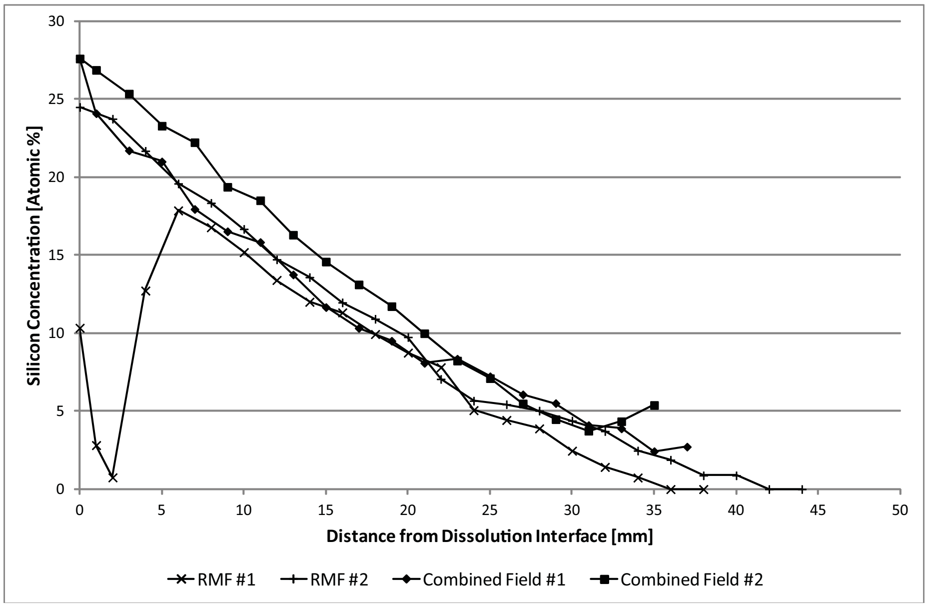

Figure 4.17: The plots above are the centerline composition profiles for the samples processed with rotating magnetic field alone and the samples processed with both magnetic fields applied. The minor increase in silicon transport with the addition of the static magnetic field is evident.

in transport is not worth the extra cost and complexity of the static field. However, the static field does impact the effectiveness of the rotating magnetic field. As such, there may be a combination of fields that produces an optimal result with significant improvement to transport in the system. Additional numerical modeling of the system could be used to optimize the field levels with the goal of increasing silicon transport through the melt.

4.7 Translated Experiments

A significant drawback of the LPD technique is that it produces a bulk crystal with graded composition. As the growth interface advances, the temperature at the interface changes due to the temperature gradient applied to the system. The temperature increase at the growth interface will increase the silicon composition of the growing material in accordance with the phase diagram. This results in the silicon composition in the grown material being graded from pure germanium to a maximum composition that is determined by where growth terminates in the temperature gradient. The solidus line composition associated with this temperature will be the maximum composition in the graded block. Growth is usually terminated by cooling the furnace after the desired experiment duration has been reached. Growth will terminate on its own when the concentration gradient between the dissolution and growth interfaces is not steep enough to drive the constitutional super-cooling required for growth.

It has been shown in the Zone Melting technique that if the temperature of the growth interface can be held at a constant temperature, the composition gradient in the grown crystal can be greatly reduced [89, 90, 111]. In that work, the growth interface was monitored optically and the feedback used to control a translation mechanism. Using this method the growth interface could be confined to a narrow range of temperature. The Zone Melting technique is very similar to LPD.

To explore this type of approach in the LPD system, a much simpler method was devised for the preliminary investigation. The crucible was simply translated the entire melt length over a 71 hour period. The 1 hour at the beginning of the experiment's 72 hour duration was set aside to allow the system to come to equilibrium. A linear stage lowered the crucible through the temperature gradient at a constant rate of $0.429mm/hr$. The addition of the pedestal for lowering the crucible had the effect of introducing heat into the system. This resulted in the complete melt back of the seed. Growth was not initiated on a seed crystal. However, the material did self seed on the crucible wall and polycrystalline growth proceeded. The sensitivity of the experiments to the thermal design is apparent. The time to optimize the thermal conditions for an experiment is considerable. Therefore it was deemed impractical for this part of study. In addition, it was desirable to maintain the same experimental conditions as the baseline samples for comparison purposes. In the translated samples, growth velocity will be determined by the translation velocity and the silicon transport in concert. Without translation, the melt is constitutionally super-cooled by diffusion driven silicon transport to induce solidification. With translation, the melt is aided in this process by the reduction in temperature as the sample moves in the temperature gradient. This should lead to faster growth rates than the baseline condition.

The EDS composition profiles for the two samples processed exhibit the same behavior. There is an upturn in composition at the bottom of the melt attributable to the self-seeding process at the crucible wall. The EDS plots are shown in Figure 4.18.

The baseline samples consist of two areas. One is the grown material and the other is the quenched melt. The grown material extends from the zero percent silicon point,

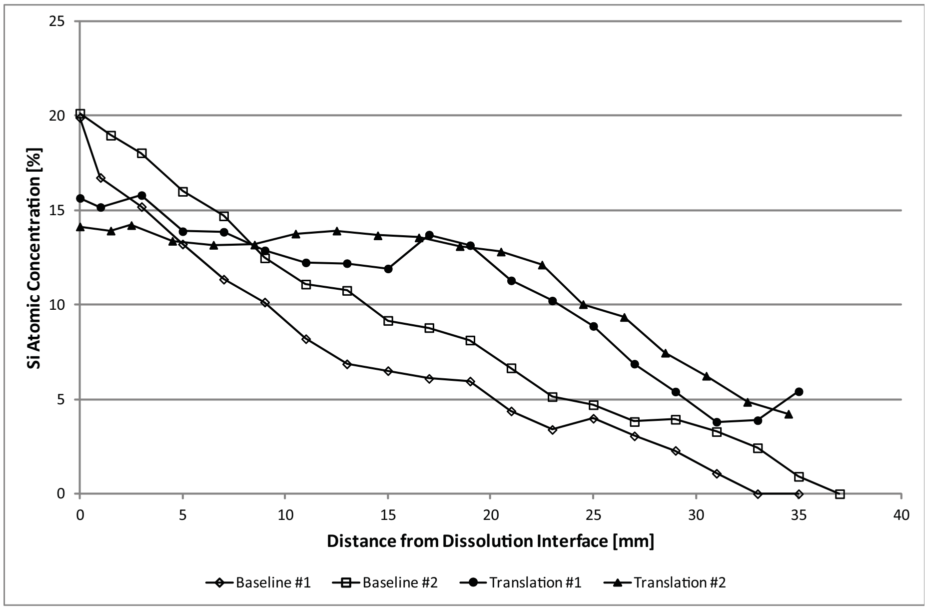

Figure 4.18: The centerline composition profiles of the translated LPD experiments are shown above. For comparison, the baseline experiments composition profiles are also shown. The region of plateau in the samples that were translated is clearly evident.

the initial growth interface, to approximately $5mm$ into the melt. The rest of the material is formed during the cool down of the sample. The slope of the concentration plot across the material is relatively constant.

In the translated samples, the composition profile after the self seeding feature proceeds with a slope close to the slope observed in the baseline samples. The velocity of the crucible effectively continuously reduces the saturation concentration for any given area of melt. Around the growth interface, growing material will reject germanium back into the melt. This dilutes the melt in silicon around the interface. Without translation, the dilution will decrease the growth velocity as more silicon must be transported into this region before the melt can be constitutionally super-cooled. With translation, the temperature in the melt is being reduced, so the amount of silicon to constitutionally super-cool the melt is also decreasing. This helps to increase the growth velocity. Additionally, with translation, the melt adjacent to the growth interface boundary layer is always moving to a higher silicon composition than the previous time step. This will increase the diffusion rate of silicon into the boundary layer as the concentration gradient is increased. The rate of germanium segregation at the solidification interface is kept more uniform during growth with translation as the temperature at the growth interface does not vary as much as it would in a standard LPD process. These factors serve to help increase the growth rate in the system. It is expected that the growth rate in the translated system should be faster than the growth rate in the baseline LPD system.

If the growth velocity becomes too high, it would be expected that regions of germanium melt dilute in silicon could become trapped in the advancing solid. Depending on the size of the inclusion, this should appear as scatter on the composition profile. No significant scatter was noted in the profile. The inclusions could be well distributed and small such that they do not cause any discernible scatter. It is also possible that a translation rate faster than that examined here may be feasible.

After the sloped region of the translated samples' composition profiles, the composition in the growing material reaches a plateau value. In this region, it would appear that the position of the growth interface in relation to the temperature field has stabilized. Solidification seems to be taking place at a relatively constant temperature. This indicates that the growth rate and the translation rate have matched up. As the translation rate is constant, the growth rate must be constant through this region of growth.

For the growth rate to become constant, the following condition must be reached. The rate of silicon transport to the growth interface must be such that the composition there is kept relatively constant. The melt side of the growth interface tends to become dilute in silicon as germanium is segregated back into the melt during solidification. The rate of germanium segregation during solidification must be matched by the silicon transport.

At the dissolution interface, the saturation composition at the melt boundary is dropping in accordance with phase diagram as the temperature drops. This will slow the overall dissolution rate into the melt. The slowing of the silicon dissolution should reduce the composition gradient in the melt. In addition, there is a narrowing gap between the growth and dissolution interfaces. The conditions above should cause the silicon composition gradient in the melt to stabilize, resulting in a constant rate of silicon transport. A constant rate of silicon transport is necessary in order to achieve a plateau in the growing materials composition profile with an applied constant rate of translation.

The plateau in the composition of the growing material indicates that the above conditions have been met. The growth interface temperature has stabilized around a single value. The composition gradient in the melt in front of the growth interface

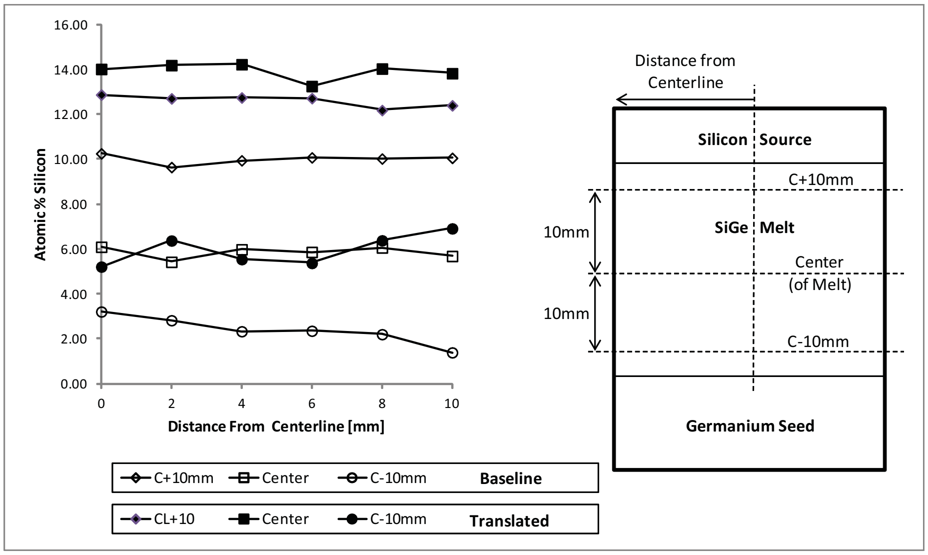

Figure 4.19: The radial composition profiles for Translated LPD Experiment #1 is plotted with the profiles from the Baseline Experiment #1. The flat composition profile is maintained despite the translation of the crucible.

has stabilized due to the reduced temperature at the dissolution interface and the shrinking melt length. A constant rate of germanium segregation from the solidifying melt and a constant rate of silicon replenishment has established.

With the addition of translation, the radial concentration profiles remained flat. This can be seen in Figure 4.19. The translation process will tend to induce radial thermal gradients in the system as the crucible will cool from the outside to the inside. This will induce radial temperature gradients in the area of the growth interface. The translation velocity would seem to be low enough to have not induced large radial temperature gradients that would affect the composition profile.

The structures of the two samples processed under translation are very similar. This can be seen in the photos of the etched sections shown in Figure 4.20. The shape of the dissolution interface shows increased dissolution around the crucible edge. The dissolution interface is not smooth but instead appears very ragged. This is possibly due to the translation process. As the melt temperature at the dissolution interface is dropping during the growth process, it is likely that the melt in this area will become constitutionally super-cooled and some solidification will occur back onto the silicon source.

The body of the material is large grain polycrystal despite the self seeding. The directional nature of the solidification will serve to increase the size of the grain

Figure 4.20: The photo above depicts the translated LPD samples. The sample on the left is Translated LPD Experiment #1 and the sample on the right is Translated LPD Experiment #2. In the Translated LPD #2 sample, there is a discontinuity in color visible midway through the sample. This indicates a distinct change in composition. In both samples, large grain structure is visible.

structure as preferential orientations for growth over take less suitably orientated grains. In one of the samples, a distinct change in color is observed in the center of the sample. The location of color change in the solid aligns with the transition from the linear increasing part of the composition profile to the flat region of the profile. In the sample with this feature, there is a drop in silicon composition as the profile transitions to the flat section. The color of the sample is strongly tied to the silicon content. As the color transition is sharp, it is expected that the drop in silicon composition will be equally as abrupt. Due to the sample spacing of the EDS composition measurements, this sharp drop was not clearly resolved.

4.8 Modified Thermal Field Experiments

The initial growth interface of the LPD process is concave to the melt. This is apparent in the experimental results as well as thermal modeling of the system. This indicates the thermal field around the growth interface has isothermal lines of similar shape. A curved interface is not optimal for growth.

With increasing curvature in the isothermal lines, the radial composition gradients in the solidified material will also increase. In order to extract material from a graded composition block of material, a flat radial composition profile is needed. In the LPD experimental work previously conducted, the growth interface shape changed during growth from concave to the melt to convex into the melt [25]. During this transition, there was a short area where the growth interface was relatively flat. The area of a flat interface could be extracted to produce a wafer with relatively constant composition over its surface. In this case, only a small region of the grown material was suitable for further use in other growth experiments. In addition, the composition of the extracted material is set by where the flat growth interface occurs rather than a composition of interest. This is illustrated in Figure 4.21.

In order to improve the flatness of the growth interface in the LPD system, a number of changes to the growth system were investigated. The first changes were necessitated by the experiments to be conducted in the magnetic fields. A new furnace arrangement had to be utilized. This furnace had shorter zone lengths and a reduced bore size. The shorter zone lengths allowed a higher axial gradient to be achieved and the reduced bore size flattened the radial temperature gradients. A simplified numerical model was prepared to show the improved trend with reducing the bore size. Plots of the calculated thermal fields are shown in Figure 4.22. With these changes alone, a significant improvement to the growth interface shape and its evolution was achieved. Radial composition plots show that the silicon concentration is relatively constant. This implies that the radial temperature gradients in the melt are small. The initial growth interface can be observed in the baseline LPD samples. It appears as a striation in the differentially etched samples. The interface in these samples continues to show curvature, concave to the melt.

To further improve the shape of the interface, a heat sink was placed below the crucible in the outer quartz ampoule. The heat sink was produced from graphite as it has high thermal conductivity and is compatible with the environment of the ampoule. The ampoule is subject to high temperature and is evacuated into the high vacuum regime. The heat sink was shaped into a "top hat" like configuration. There is a wide base in contact with the bottom of the ampoule where the temperature is lower than above. A narrow central peak extends up and contacts the bottom of the crucible in the center. This arrangement is illustrated in Figure 4.23. The idea with this arrangement was to remove heat from the center of the system. This should additionally flatten the radial temperature gradients and therefore the growth

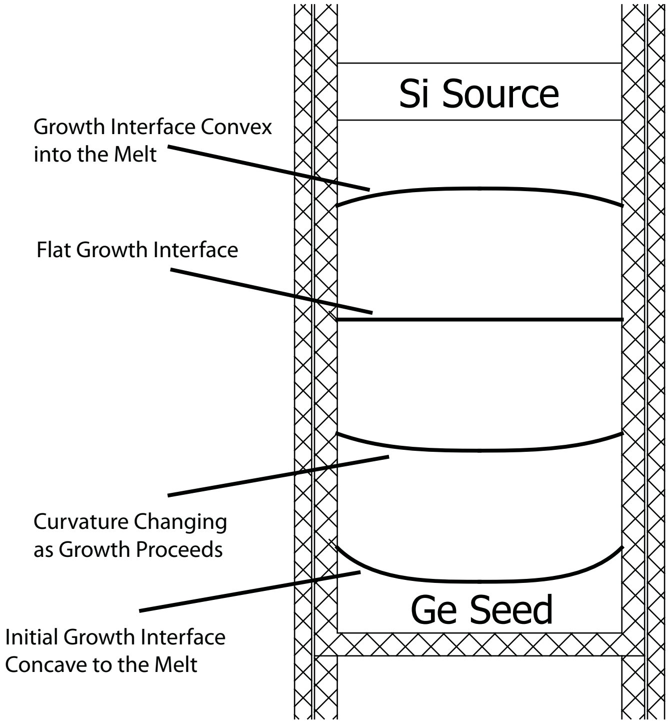

Figure 4.21: The diagram above illustrates the evolution of the growth interface seen in the previous LPD experiments.

interface.

This effect was not observed in the experiments. The graphite efficiently absorbed the radiation from the furnace and added heat into the system. This is evidenced by the complete melt back of the seed material in the samples processed with the heat sink in place. In order to utilize a heat sink in the current configuration, it will be necessary to shield the heat sink from radiative heat transfer or change the material of the heat sink.

The samples processed with the heat sink in place produced dramatically different results from what has been seen in other experiments. The samples are shown in Figure 4.24. The change is likely attributable to a significant rise in the temperature at the bottom of the crucible. The silicon source is completely dissolved in one sample and almost totally consumed in the other. This indicates a substantial increase in the transport in the system. The other notable change is that sample is divided into a top and bottom section by a distinct abrupt color change in the material. Near the bottom of the crucible the material is a dark polycrystalline material. At the top near the dissolution interface, the material is much lighter in color and shows evidence of

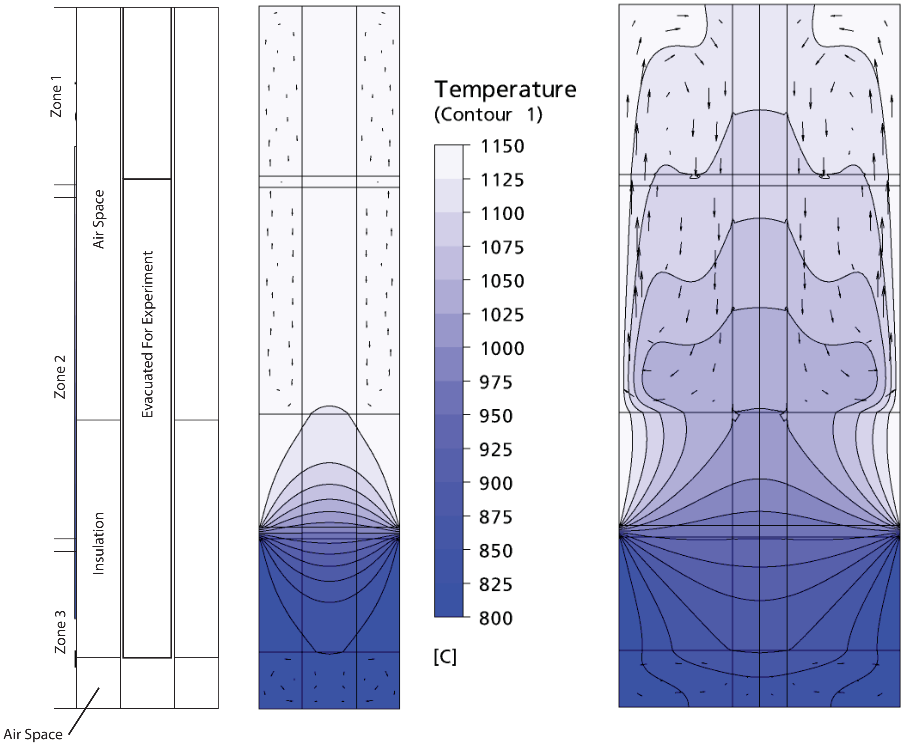

Figure 4.22: To qualitatively show the improvement in the temperature profile with the reduction of the furnace bore size, a simplified numerical model of the furnace bore was prepared. A diagram of the modeled domain is shown in the left. The result for the $2.5in$ furnace bore is shown in the center and the result for the $5in$ furnace bore is shown on the right. Zone lengths were kept the same. The domain used is typical of a furnace setup for LPD growth. Boundary conditions typical of an LPD growth system were used in both models. The temperature contours are plotted with a vector plot of the flow field in the air space overlaid. The improvement in the axial gradient is very apparent in the results.

macro-segregation of silicon in the form of needle like crystals.

The EDS composition profiles support the observations from the samples. The EDS data is plotted in Figure 4.25. In the region near the bottom of the crucible, the silicon composition is much higher than that observed in any other LPD experiment. The profile rises in silicon concentration from this point to the discontinuity line noted in the etched samples. There is a slight turn up in composition around the bottom of the crucible. This is indicative of self seeding on the bottom of the crucible due to a lack of seed material. The upturn is due to additional constitutional super-cooling needed to trigger a nucleation process. On the other side of the discontinuity, the melt composition drops to a much lower silicon concentration. The measurements are

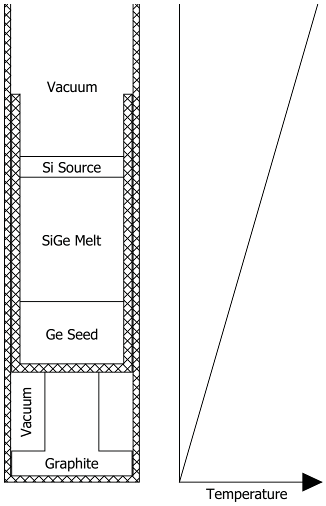

Figure 4.23: The diagram above illustrates the LPD ampoule with the heat sink inserted. The position and shape of the heat sink in the applied thermal gradient should aid in heat extraction from the center of the seed material. This would have the effect of flattening the initial growth interface.

Figure 4.24: The photo above shows the samples processed with the heat sink in place. The discontinuity line midway through the samples is clearly evident. The sample on the left is Heat Sink Experiment #1 and the sample on the right is Heat Sink Experiment #2. The large grain structure of the grown material is visible in the lower area of the samples. The needle structure in the segregated section of the sample is also clearly evident.

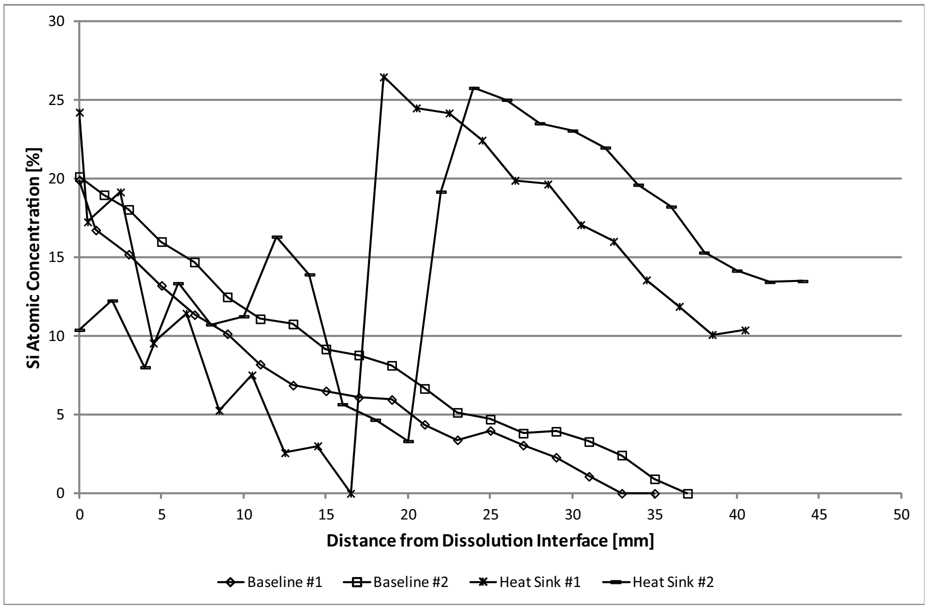

Figure 4.25: The centerline composition profiles of the samples processed with the heat sink are shown above. The Baseline Experiments' composition profiles are also included for comparison. The discontinuity visible in the etched samples is also very evident on the composition profiles.

scattered in this region of the melt due to the segregation. However, there is a rising trend in the silicon composition towards the dissolution interface.

The observed profile can be explained as follows. The discontinuity line would seem to indicate that this was the point that growth had reached when the cooling of the furnace was begun at the end of the 72 hour experiment time. The segregation in the solid above the discontinuity is indicative of a quenched melt.

The high silicon region of the material below the discontinuity is considered to have been solidified during the experiment time by the same mechanism as LPD growth. The melt in front of the growth interface is constitutionally super-cooled by transported silicon and solidification takes place on the growth interface. Using the SiGe phase diagram, the liquidus composition values can be calculated for the observed solidified material composition. This is shown in Figure 4.26. This indicates the required silicon concentration in the melt for solidification to occur by constitutional super-cooling. Due to the large separation between solidus and liquidus in the SiGe phase diagram, these values are much lower than the solid composition values.

In this system, the mass transport is assumed to be dominated by diffusion. A numerical model of a pure diffusion process for this system geometry was prepared.

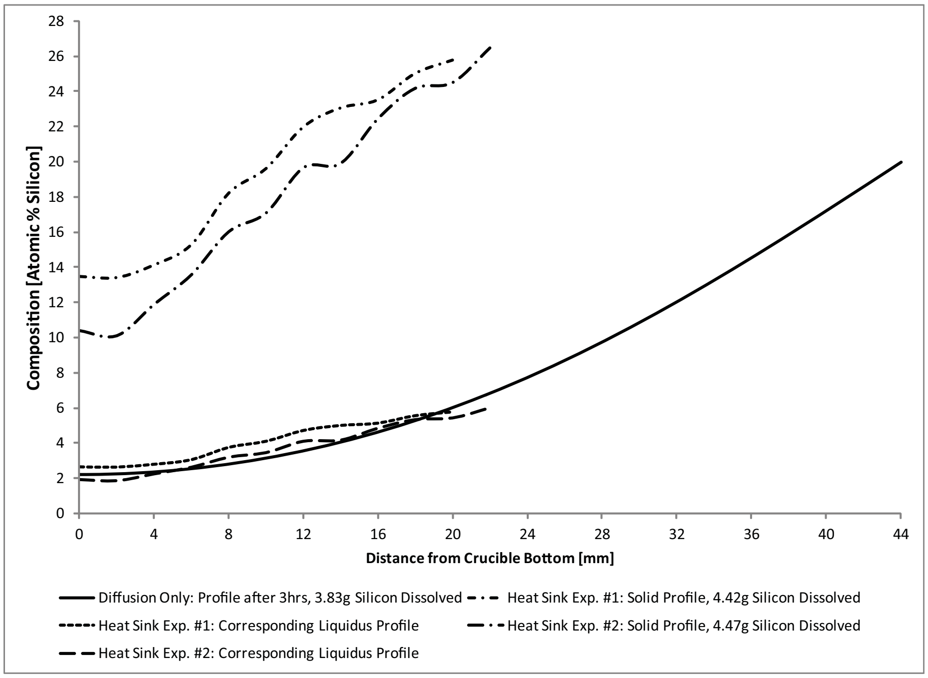

Figure 4.26: In the plot above, the centerline composition profile of the heat sink samples is shown truncated at the discontinuity. To more easily compare the slopes of the lines, the distance measure has been reoriented to measure from the bottom of the crucible. The liquidus compositions, corresponding to the solidus compositions measured in the sample, are also plotted. The gap between the liquidus and solidus profiles indicates the segregation coefficient in the material system. Also plotted is a diffusion only transport model of silicon into the melt. This has been plotted from the dissolution interface to the crucible bottom.

Solidification effects were ignored. The time for the composition of the melt at the bottom of the crucible to reach the calculated liquidus composition was solved. This was found to be approximately 3 hours. The composition that the bottom of the melt had to reach was only approximately 2% silicon. This corresponds to a liquidus temperature of approximately 967°C. The solidus composition at this temperature is approximately 10.5% silicon. As all flow effects are not included in the model, the 3 hour time for the initiation of growth is not accurate. However, it should provide at least an order of magnitude estimate. This shows that the composition profile observed is possibly due to an LPD process. Growth can be initiated long before the end of the experiment time.

The calculated liquidus composition profiles for the solidified material match the calculated diffusion profile quite well. This indicates that the growth could have been driven by a diffusion dominated process. The high degree of germanium rejection back into the melt will drive high concentration gradients in the growth interface boundary layer. This should speed transport of silicon from the bulk melt to the interface, allowing growth to proceed quickly. This is additionally helped by lower axial temperature gradients in the melt. The reduced gradient is expected due to the introduced heat from the graphite and it is evidenced from the shallow slope of the liquidus compositions. The flatness of the axial temperature gradient means the saturation composition of the melt increases less quickly as growth proceeds. The primary effect limiting growth rate would seem to be the germanium segregated at the growth interface. These factors could allow the growth to proceed faster than seen in other experiments.

The total dissolved silicon incorporated in the solid during the experiment time can be estimated by integrating the composition profile using the discontinuity as the upper bound. Using this method, both samples show similar amounts of incorporated silicon, approximately $4.5g$. This weight is a lower bound on the amount of silicon that must be dissolved during the growth period. The silicon sources used in the experiments weigh approximately $5.7g$. By integrating the calculated diffusion model's compositional profile, the total dissolved silicon in the melt is found to be $3.85g$. Based on this model, the majority of the silicon dissolution occurs during the beginning of the growth process. Given the small difference between the calculated weight of silicon in the grown material and the total weight of the source material, it is possible that growth may have proceeded further if more silicon was available for dissolution. In one of the samples, the silicon source did completely dissolve. In the other, the size of the source was greatly reduced. As the source material dissolves, the surface area in contact with the melt will eventually decrease, limiting the dissolution rate.

Once growth is initiated, the majority of the required silicon to produce the observed concentration profile is dissolved in the melt. This will aid in a fast growth rate once growth begins. The dissolution rate can be significantly slower after the initiation of growth and the observed profile achieved. If the dissolution rate does not keep up with the rate of silicon incorporation into the growing solid, the melt will slowly become dilute in silicon and the growth rate will slow. The melt becoming dilute by such a mechanism is likely the cause for the low silicon concentration region observed in the samples. The discontinuity observed between the regions was originally stated as to have been induced by the cooling of the furnace. It is also possible that this was simply the point where the melt became too dilute in silicon to support

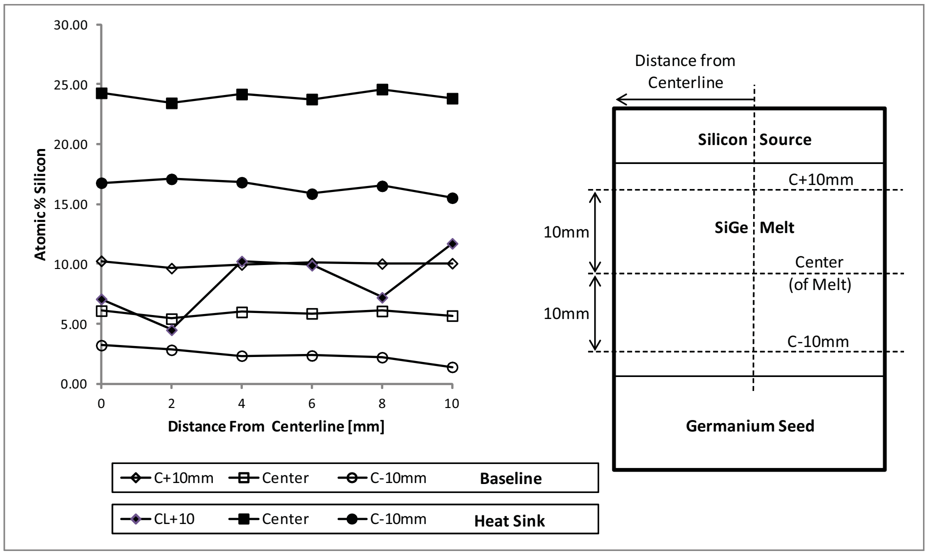

Figure 4.27: The plot above shows the radial composition profiles of the Heat Sink Experiment #1 sample and the Baseline Experiment #1 sample. The radial gradients are again low in both samples. The modified thermal field has not adversely affected the radial distribution of silicon. There is scatter in the Heat Sink "C+10mm profile line. This is because that profile line runs through the highly segregated area of the sample.

any further growth.

The radial composition gradients remain flat despite the alteration to the thermal field. This can be seen in Figure 4.27. Given the addition of heat at the center of the bottom of the crucible, it was expected that strong radial temperature gradients would form and possibly disrupt the radial composition gradients. It is possible that additional measurements at other locations in the grown material may show a more significant gradient. The discontinuity line between the two regions of material is very flat. This interface indicates that the radial gradients in this area of the melt are low.

These experiments show that the LPD technique could be extended to much higher silicon concentrations than those that have been currently produced. Despite the high segregation of silicon, the growth proceeds in a similar manner to previous experiments. The issue of seeds for growth at higher compositions could be overcome by utilizing successive LPD experiments, increasing the temperature between runs. The first run could produce material high enough in composition to be used as seed material for the next run. Higher concentrations could also be achieved with a longer melt zone. In that case, a pure germanium seed could be used. The growth time would have to be extended to allow the silicon to diffuse across the greater distance between the dissolution and growth interfaces. It is predicted that this approach would significantly slow the growth rate at the start of the process, potentially making the technique infeasible.

Chapter 5

Conclusion

The work in this dissertation explored the transport of silicon through silicon germanium, SiGe, melts by a variety of transport mechanisms. This work was conducted in environments similar to the conditions for Liquid Phase Diffusion, LPD, growth system. The results of this work will directly affect the future direction for the optimization of the LPD growth technique for SiGe. In addition, many of the trends and phenomena observed will have application beyond LPD growth. LPD is seen as a first stage growth process. In this role, the material produced by LPD would be utilized for seed feedstock for successful growth by a high-yield crystal growth technique. A technique like melt replenishment Czochralski is a good candidate for this next growth step.

5.1 Contributions

The experiments conducted in this work can be divided into two catagories. First the dissolution of silicon into a silicon germanium melt was examined in isolation. The second part of the work examined the Liquid Phase Diffusion technique specifically. The effect of a number of applied stimuli on the system were investigated.

5.1.1 Dissolution

The Dissolution Experiments examined the effect of the orientation of the dissolution interface on the rate of dissolution of the silicon seed into the melt. When the dissolution interface is at the top of the melt, the dissolving silicon entering the melt serves to stabilize the melt against convection and the transport in the melt proceeds as a diffusion dominated system. This is due the solutal buoyancy of silicon in the heavier germanium melt. This was noted in previous work with the LPD system [25]. The growth rate in LPD is slow as the growth rate is fixed by the transport rate of the silicon species through the melt. When the transport is diffusion dominated the growth rate is slow.

In order to improve the growth rate in LPD, enhancing the diffusion of silicon in the melt is desirable. By reversing the orientation of the dissolution interface, such that silicon is dissolving at the bottom of the melt, the mass transport will be increased as the solutal buoyancy force is now acting to push the silicon away from the dissolution interface. The amount of silicon dissolved into the melt was significantly enhanced when the dissolution interface was placed at the bottom of the melt. However, the enhanced transport seems to disrupt the flow in the melt such that conditions are not favorable for crystal growth.

With the dissolution interface at the bottom of the melt, the transport appears to be primarily driven by flow in the melt. There appears to be strong flow across the dissolution interface. This is evidenced by a wavy interface. The destabilization of the interface is a negative effect for crystal growth where the stability of the growth interface will have a strong effect on the quality of the grown material. The rate of transport would seem too high for stable crystal growth. The effective diffusion coefficient, as calculated from the height of silicon dissolved, has increased by a factor of ten over the diffusion dominated experiments.

With the dissolution interface at the bottom of the melt, the condition at the top surface of the melt could be varied. With the free surface uncovered, the melt could be subject to additional mixing by surface tension driven convection and higher flow velocity with no fixed boundary present. By covering the top of the melt, the surface convective flows are eliminated and the flow velocity in this region will be slowed due to the presence of the boundary. The effect of the free surface on silicon transport was found to be significant. The presence of a free surface enhanced the mixing of silicon in the melt.

To better control the flow in the system and retain some of the enhanced transport, a static magnetic field was applied to suppress the flow in the melt. The effect of the field was to enhance the silicon dissolution for both orientations of the dissolution interface. Enhanced dissolution was observed with and without the free surface present. The alteration of the flow structure by the magnetic field serves to create a condition where more dissolution is realized. For the cases where the dissolution interface is at the bottom of the melt, the disruption of convective flow in the melt could lead to the silicon building up at the top of the melt rather than the silicon being remixed back towards the dissolution interface like a convective cell would do. This would lead to higher concentration gradients around the dissolution interface and therefore a higher dissolution rate. The samples processed under these condition exhibit evidence of this change in flow structure.

With the silicon dissolving from the top of the melt, the same effect of enhanced transport with application of the magnetic field was observed. The amount of silicon dissolved increased with the magnetic field applied. Again, the change in flow structure is acting to increase dissolution. In this case, the interface also exhibits a dramatic change in shape. The dissolution around the crucible wall has been significantly increased compared to the center of the melt. This implies strong flow structure in this area. Numerical modeling of this phenomena has suggested that the application of the field strengthens the axial flow and confines it against the crucible wall. This could lead to the dissolution interface observed.

In these cases, the magnetic field is not having the effect usually associated with applied static magnetic fields. Rather than suppressing the flow, the flow structures in the melt are altered such that transport is increased. The field strength used in this work was not optimized to obtain any specific effect. Instead, a high field strength was chosen such that an observable effect would be produced. It is possible that a different field strength could modify these effects. In one of the numerical studies, the effect of enhanced dissolution around the crucible wall was increased with a lower field strength.

For the system with silicon dissolving from the top, the dissolved height of silicon was compared to the calculated distribution of silicon from the numerical models. It was found that it was not possible to match the trend seen in the experiments with the trend from the numerical model. The interface condition used in the numerical model was equilibrium saturation of the melt with silicon. This condition, combined with a constant diffusion coefficient, does not produce the experimental trend. To better match the experiment trend, a number of time dependant interface conditions were investigated. It was found that a slow ramp of concentration at the dissolution interface to the saturation value could produce a better fit to the observed results. Correlating the experimental dissolution heights to an effective diffusion coefficient produces a similar trend. The effective diffusion coefficient increases with time and appears to asymptotically approach a stable value. The diffusion coefficient is expected to vary with composition in the melt so this result is not unexpected. These experiments were conducted over a relatively short time period when compared to a full LPD experiment. Over these short time periods, the kinetics of the dissolution process and the variation of the diffusion coefficient seem to have a significant impact on the concentration in the melt.

The temperature dependence of the diffusion in the system was also investigated. A trend to increased diffusion was observed with increased temperature.

5.1.2 Liquid Phase Diffusion Growth

The transport and growth of silicon germanium by LPD was studied with a variety of magnetic field conditions applied to the system. The thermal field in the LPD system was improved through the redesign of the system to be compatible with the magnetic field generators. This significantly improved the radial composition gradients in the melt. Significant coupling between the magnetic fields and the thermal field was also noted. The application of the field shifted the temperature field resulting in either more or less melt back of the initial seed material. The strength of this coupling requires that the initial position of the growth system be determined with the magnetic field condition for the experiment in mind. For this work, the position of the system was not altered between experiments to allow for direct comparison.

The application of a static magnetic field to the system significantly slowed the rate transport in the melt. In addition, the temperature field in the melt shifted towards the dissolution interface. This resulted in little to no melt back of the initial seed crystal. The reduction of flow structure in the melt is likely the cause of these effects. The reduced flow structure in the melt will slow the growth rate. This is evidenced by the reduced transport of silicon in the melt noted in the experimental results. The initial LPD system is already stabilized against natural convection due to the buoyancy of the silicon species in the germanium rich melt. The addition of the magnetic field to further suppress the flow may be undesirable as the growth rate is negatively impacted.

A rotating magnetic field, RMF, was also utilized with the LPD system. The RMF should induce addition radial and tangential flow structure in the melt resulting in increased controlled mixing. This was the effect seen in the experiments conducted. The rotating field also impacted the thermal field in the system. The additional mixing induced by the field shifted the temperature field towards the growth interface. This resulted in almost complete melt back of the seed material. The amount of material grown during the experiment time was significantly increased with the application of the rotating field. The addition of a rotating magnetic field could be of significant advantage in LPD growth of silicon germanium. The controlled mixing induced by the magnetic field could be used to significantly increase the growth rate. This could shorten the time for an experiment or a larger melt length could be used. A longer melt length could allow LPD to reach higher compositions of silicon while utilizing a Ge seed crystal.

To improve the performance of the rotating field, a static magnetic field was applied to the system at the same time as the rotating magnetic field. The static field should suppress the convective flows and allow the induced mixing from the rotating field to become a more prominent feature in the melt flow field. This effect was seen in the experimental results. The transport of silicon in the melt is enhanced over the rotating field alone case with the addition of the static field. However, the improvement to the transport is not as significant as the case where the rotating field is applied to the baseline case with no applied fields. The same coupling with the thermal field that was observed in the rotating field alone case was observed in these experiments. This is consistent with the effect of the rotating field being enhanced by the applied static magnetic field. The application of the static field and the rotating field together does enhance the transport seen in the rotating field only case. However, with only a small increase in transport realized, it is unlikely the increase in complexity and expense that the use of the static field generator causes can be justified. It is possible that, with further optimization of the field levels in combination, an even greater increase in transport could be achieved that would justify the use of the combined field.

The LPD system was also translated to see if the axial composition gradients in the system could be reduced. This was achieved with no optimization of the translation velocity. Ideally the growth interface would be maintained in the same position in the furnace at all times resulting in a constant composition in the grown material. In these experiments, the crucible was simply translated at a constant velocity. Even under these conditions, significant flattening of the axial composition gradient was achieved. The growth of an extended section of constant composition material should be possible utilizing this technique. The matching of the translation velocity to the growth interface could be optimized through modeling and experiment or more dynamically through direct observation of the growth interface position. This could make LPD growth a far more attractive method for producing seed material for successive growth techniques.

The final experimental condition involved altering the thermal field to produce a flatter initial growth interface. A graphite heat sink was inserted below the seed to extract heat from the center of the material system. However, this was not the effect achieved as the the graphite introduced additional heat into the bottom of the crucible, completely melting back the seed. What these experiments did show was the very strong dependence of the growth on the thermal conditions in the melt. In addition, the silicon composition in the material grown during these experiments was very high compared to the normal LPD experiments. This shows that if SiGe seed material can be obtained, the LPD technique could be used to grow material to higher silicon compositions. The large miscibility gap present in the material system allows the silicon concentrations in the melt to be quite low yet the solidified material can have a high silicon concentration. The additional transport of silicon required for growth of higher composition material may lower the growth rate.

5.2 Future Work

5.2.1 Dissolution

The Dissolution Experiments will be continued with an emphasis on the small diameter experiments. The reduced flow structure with the smaller diameter should hopefully make it easier to separate out various transport effects and better study the diffusion coefficient. The time dependence of the effective diffusion coefficient should be examined with increasing experiment times to identify if there is an asymptotic value being approached. This information can be used to improve the numerical model of the dissolution process. If the observed experimental results can not be numerically duplicated, it may be necessary to further investigate the dissolution kinetics for another effect contributing to the observed experimental data.

To facilitate this work, a $8mm$ crucible platform for performing this work was developed by the author. This was briefly used in the small diameter dissolution height experiments. This apparatus can be utilized with the static magnetic field to suppress flow structure in the melt. To avoid issues with segregation and therefore allow better analysis of the melt's composition, the development of a shear cell type system should be undertaken. This would allow for much more accurate determination

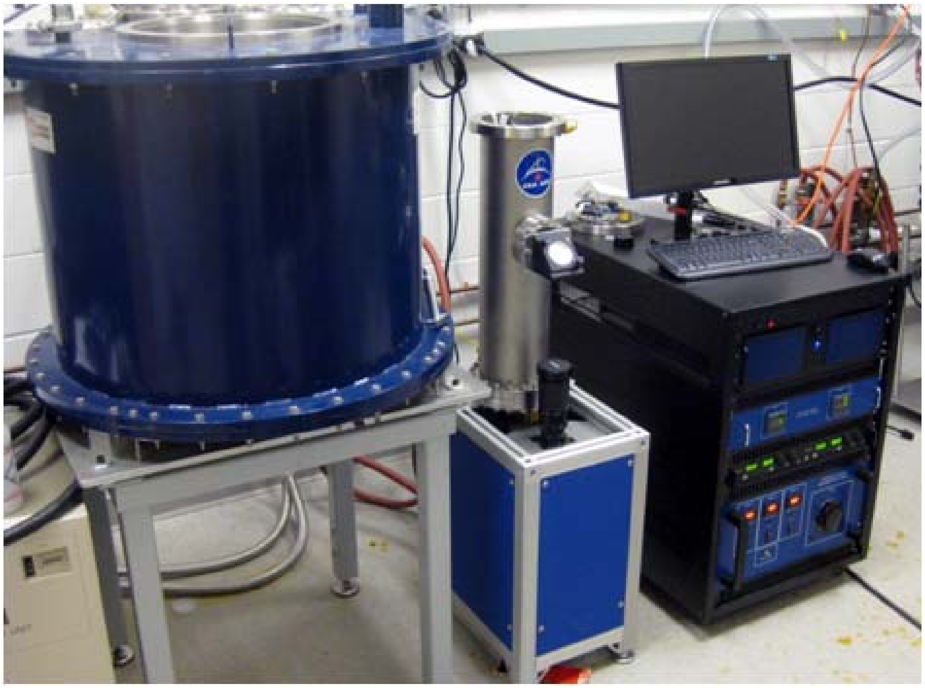

Figure 5.1: The above is a photo of the current MICAST furnace (center) its controls (right) and the static magnetic field generator (left). The infrared camera for monitoring the growth interface position is mounted just in front of the furnace. A mirror redirects the image from the furnace allowing the furnace to be used inside the static magnetic field.

of the composition in the quenched melt.

5.2.2 Liquid Phase Diffusion

The Liquid Phase Diffusion experiments should proceed forward with a focus on the rotating magnetic field and improving the growth rate. In addition, the field conditions studied here should be revisited with the crucible repositioned for each magnetic field condition. This way the initiation and evolution of the growth process can be studied. The translated LPD experiments should also be considered.

A $8mm$ crucible platform equipped with a rotating magnetic field generator and translation was developed by the author for this future work. This is similar to the dissolution platform above but with a furnace more suited for producing high axial gradients. Again this system can be used inside the static magnetic field.

In addition to the platform above, a new furnace was recently developed by the author as part of the MICAST project to investigate cast aluminum microstructure.

This furnace is pictured in Figure 5.1. This furnace, in addition to the same features as the new $8mm$ LPD system, has an optical window allowing for in-situ monitoring of the solidification velocity. This system was designed with the LPD experimental requirements in mind and can be adapted to allow for direct growth velocity measurement and eventually translation to hold the growth interface static with respect to the temperature field. An additional benefit of this platform is that it utilizes a silica aerogel crucible to provide a clear view of the solidifying sample. The aerogel essentially acts as an adiabatic zone and allows for very high temperature gradients between the heaters. This could provide another aspect of the LPD growth system to investigate.

5.2.3 Melt Replenishment Czochralski

During the course of this work, a complete refurbishment of a full scale crystal puller was undertaken. The system was completely rebuilt with the intent to use it as a melt replenishment research platform. The hot zone was redesigned for a 4 inch crucible and facilities were placed inside to allow for melt replenishment apparatus. The puller was originally designed as a silicon puller and as such this work would begin with work at the silicon rich end of the material system. In addition, growth from the germanium rich side would be possible with very little rework of the system. There are numerous configurations of melt replenishment that could be utilized within this platform to take advantage of the transport mechanisms investigated in this work. The furnace in its current form is shown in Figure 5.2.

Eventually this process could utilize seeds from the Liquid Phase Diffusion projects. SiGe seed material is not currently commercially available. Therefore, seed material would need to be produced or growth would need to be started with either a pure silicon or germanium seed.

Figure 5.2: The refurbished Czochralski furnace at the University of Victoria is shown above. The furnace has been design and equipped with facilities to allow for the future integration of melt replenishment apparatus.

Appendix A

Preparation of Materials for Experiment

Germanium and Silicon Materials

The materials were prepared according to the following process:

1. Cut, core and weigh materials to experiment requirements.
2. Ultrasonic wash the materials in water.
3. Ultrasonic wash the materials in acetone.
4. Ultrasonic wash the materials in methanol.
5. Wet etch the materials. A solution of $3:1$, $HNO_3(70\%) : HF(40\%)$, was used to etch the silicon. The silicon was left in the etch for 2-3 minutes then rinsed in water. A solution of $3:1:1$, $H_20 : H_2O_2(30\%) : HF(40\%)$, was used to etch the germanium. The germanium was left in the etch for 3-5 minutes then rinsed in water.
6. Materials are placed in methanol after the water rinse.
7. Prior to loading into the growth system, materials are dried with compressed nitrogen (4N8 purity).

Quartz Parts

All quartz parts were prepared according to the following process:

1. The quartz parts are placed into an Aqua Regia bath ($3:1$, $HCl(37\%) : HNO_3(70\%)$).
2. The Aqua Regia reaction is allowed finish, approximately 8 hours for a typical quantity.
3. The parts are rinsed with water and then left to soak in water for approximately 2-4 hours.
4. The parts are then rinsed with methanol and dried with compressed nitrogen (4N8 purity).
5. The parts are allowed to dry in air approximately 1-2 hours before use.

Graphite Parts

Post machining of the graphite parts, the following cleaning procedure was used:

1. The parts are wiped down with acetone.
2. Ultrasonic wash the parts in a methanol bath.
3. Allow the parts to dry in air for at least 24 hours prior to use.

Appendix B

Preparation of Materials for Analysis

Procedure

The Diffusion Experiment and Liquid Phase Diffusion samples were all prepared according to the following procedure:

1. Samples broken apart during the quench process are reassembled as best as possible with a quick set epoxy. This maintains the spatial arrangement.
2. Samples are wax mounted on plate for sectioning. Cuts made on the sample will be parallel to the plate.
3. Approximately $2mm$ slice removed from edge of sample opposite the plate. This will provide a flat for polishing the segment in a later stage.
4. Second cut made $1mm$ offset from center of the sample towards the plate. This splits the sample into two bulk halves. The bulk half mounted on the plate is demounted and stored. The bulk half remaining has a large flat near the center of the sample and a small flat near its outer edge.
5. The large flat face of the remaining bulk half is wax mounted to the plate for the last section.
6. The last section is made $2mm$ offset from the plate face. This produces a $2mm$ thick wafer with parallel faces for SEM analysis and a bulk piece of sample with two parallel flats that will be etched to reveal structure.
7. The $2mm$ wafer and bulk segment are wax mounted for polishing. The small flat on the bulk segment is mounted to the polishing jig. The face towards the center of the sample will be polished.
8. Both samples are polished to a submicron finish with diamond suspensions and a final step of colloidal silica.
9. The bulk segment is wet etched in a solution of $3:1:1$, $H_2O : H_2O_2(30\%) : HF(40\%)$. The material is checked every 1-2 minutes, for the LPD samples, more frequently for the Dissolution samples, to see if the material's structure is apparent. Once the material's features are prominent, the segment is rinsed and dried.

10. The $2mm$ wafer is mounted to a SEM sample stub with the backside painted with graphite to ensure good conductivity between stub and sample. The sample is now prepared for analysis.

Appendix C

Equipment Utilized for Experiments and Analysis

Experiments

- Dissolution experiment furnace. Mellen Company DC Tube Furnace; 3 zone layout with 3”-6”-3” zone lengths; 5” bore; water cooled exterior.
- LPD experiment furnace. Mellen Company DC Tube Furnace; 3 zone layout with 3”-6”-3” zone lengths; 2.5” bore; water cooled exterior.
- Static magnetic field generator. American Magnetics superconductor magnet core and controls; Custom enclosure for conduction cooled operation; 13” bore; Maximum field 1.25T.
- Rotating magnetic field generator. Custom wound coils and PLM signal generator; Magnet array has 13” OD and 8” ID; Frequency range 1 to 100Hz; Maximum field 10mT.
- Translation mechanism. Custom step motor driven stage; National Instruments microstepping controller.
- Vacuum pump systems. Varian or Leybold turbomolecular pump with rotary vane backing pump. Thermal conductivity and cold cathode gauges for vacuum measurement.

Analysis

- Sample Sectioning. Buehler IsoMet saw with low concentration diamond OD blade.
- Sample Polishing. MR Semicon LabOne polisher with South Bay Technology polishing fixture.
- SEM for analysis of Dissolution Experiments. FEI DualBean Strata 235 SEM with EDAX EDS system.
- SEM for analysis of LPD experiments. Hitachi S-3500N SEM with Oxford Instruments EDS system.

Appendix D

Materials Used in Experiments

Experiment Materials

- 5N Zone Refined Polycrystalline Germanium, material origin Russia or China.
- 5N Single Crystal Germanium rods, un-doped, OD ground to $25mm$, $100mm$ long. Material from Lattice Materials LLC.
- 5N Single Crystal Silicon rods, un-doped, OD ground to $25mm$, $125mm$ long. Material from Lattice Materials LLC.
- Quartz material is Heraeus or GE/Momentive clear fused quartz.
- Graphite material utilized is from POCO Graphite, grade DFP3.

Chemicals

- Deionized Water, $5M\Omega$
- Methanol, Reagent Grade
- Acetone, Reagent Grade
- Hydrogen Peroxide (30%), Reagent Grade
- Hydrochloric Acid (37%), Reagent Grade
- Nitric Acid (70%), Reagent Grade
- Hydrofluoric Acid (40%), Reagent Grade

Bibliography

[1] D.L. Harame, S.J. Koester, G. Freeman, P. Cottrel, K. Rim, G. Dehlinger, D. Ahlgren, J.S. Dunn, D. Greenberg, A. Joseph, F. Anderson, J.S. Reih, S. Onge, D. Coolbaugh, V. Ramachandran, J.D. Cressler, and S. Subbanna. The revolution in sige: Impact on device electronics. *Applied Surface Science*, 224:9–17, 2004.

[2] R.H. Deitch, S.H. Jones, and T.G. Digges. Bulk single crystal growth of silicon-germanium. *Journal of Electronic Materials*, 29(9):1074–1078, 2000.

[3] R.H. Deitch, S.H. Jones, and T.G. Digges. Growth of large diameter silicon-germanium monocrystals. *Materials Research Society Symposium*, 587, 2000.

[4] E. Kasper. Prospects of sige heterodevices. *Journal of Crystal Growth*, 150:921–925, 1995.

[5] P. Raue, A. Lawerenz, L. Long, M. Rinio, E. Buhrig, and H.J. Moller. Multicrystalline si1-xgex alloys for solar cell applications. *14th European Photovoltaic Solar Energy Conference and Exhibition*, 1997.

[6] G. Bremond, A. Daami, A. Laugier, W. Seifert, M. Kittler, J. Poortmans, M. Caymax, K. Said, M. Konuma, A. Gutjahr, and I. Silier. Sige thin-film structures for solar cells. *Materials*, 485:43–48, 1998.

[7] K. Said, J. Poortmans, M. Caymax, R. Loo, A. Daami, G. Bremond, O. Kruger, and M. Kittler. High quality, relaxed sige epitaxial layers for solar cell application. *Thin Solid Films*, 337:85–89, 1999.

[8] J.D. Cressler. Silicon-germanium heterojunction bipolar transistors. *Device and Circuit Cryogenic Operation for Low Temperature Electronics*, pages 69–84, 2001.

[9] D.J. Paul. Silicon germanium heterostructures in electonics:- the present and future. *Thin Solid Films*, 321:172–180, 1998.

[10] A.S. Segal, S.Y. Karpov, A.P. Sid'ko, and Y.N. Makarov. Quasii-thermodynamic model of sige epitaxial growth. *Journal of Crystal Growth*, 225:268–273, 2001.

[11] N. Usami, Y. Azuma, T. Ujihara, G. Sazaki, K. Nakajima, Y. Yakabe, T. Kondo, S. Koh, Y. Shiraki, B. Zhang, Y. Segawa, and S. Kodama. Sige bulk crystal as a lattice matched substrate to gaas for solar cell applications. *Applied Physics Letters*, 77(22):3565–3567, 2000.

[12] H. Presting. Challenges for sige-heterotechnology. *Materials Research Society Symposium*, 379:417–432, 1995.

[13] A. Splett, T. Zinke, B. Schuppert, K. Petermann, H. Kibbel, H.J. Herzog, and H. Presting. Integrated optoelectronic waveguide-detectors in sige for optical communications. *SPIE*, 2550:224–234, 1995.

[14] S. Vyas, D.W. Greve, T.J. Knight, R.M. Strong, and S. Mahajan. Growth of epitaxial gexsi1-x for infrared detectors by uhv/cvd. *Vacuum*, 46:1065–1069, 1995.

[15] R. Strong, D.W. Greve, R. Misra, M. Weeks, and P. Pellegrini. Gesi infrared detectors. *Thin Solid Films*, 294:343–346, 1997.

[16] H.J. Herzog. *Crystal Structure, Lattice Parameters and Liquidus-Solidus Curve of the SiGe System*, chapter 2, pages 45–49. INSPEC, 2000.

[17] J. Poortmans, S.C. Jain, J. Nijs, and R. Van Overstraeten. Materials properties of (strained) sige layers. *Advanced Silicon and Semiconducting Silicon-Alloy Based Materials and Devices*, pages 185–214, 1994.

[18] A. Schuppen and H. Dietrich. High speed sige heterobipolar transistors. *Journal of Crystal Growth*, 157:207–214, 1995.

[19] Y.J. Mi, H. Xie, E.A. Fitzgerald, D. Monroe, F.A. Thiel, and B.E. Weir. Extremely high electron mobility in si/gexsi1-x structures grown by molecular beam epitaxy. *Applied Physics Letters*, 59(13):1611–1613, 1991.

[20] K. Ismail, J.O. Chu, and B.S. Meyerson. High mobility in sige alloys for device applications. *Applied Physics Letters*, 64(23):3124–3126, 1994.

[21] K. Nakajima, S. Kodama, S. Miyashita, G. Sazaki, and S. Hiyamizu. Growth of ge-rich sixge1-x single crystal with uniform composition (x=0.02) on a compositionally garded crystal for use as gaas solar cells. *Journal of Crystal Growth*, 205:270–276, 1999.

[22] E.A. Fitzgerald, Y.H. Xie, D. Monroe, P.J Silverman, J.M. Kuo, A.R. Kortan, F.A. Thiel, and B.E. Weir. Relaxed gexsi1-x structures for iii-v integration with si and high mobility two-dimensional electron gases in si. *Journal of Vacuum Science Technology*, 10(4):1807–1819, 1992.

[23] P. Dold, F.R. Szofran, and K.W. Benz. Thermoelectric convection in vertical bridgman grown germanum-silicon. *Journal of Crystal Growth*, 291:1–7, 2006.

[24] N. Armour, M. Yildiz, E. Yildiz, and S. Dost. Liquid phase diffusion growth of sige single crystals under magnetic fields. *ECS Transactions*, 16(10):135–146, 2008.

[25] M. Yildiz. *A Combined Experimental and Modeling Study for the Growth of SixGe1-x Single Crystals by Liquid Phase Diffusion*. PhD thesis, University of Victoria, 2005.

[26] E. Yildiz. A numerical simulation study of the effect of static and rotating magnetic fields in liquid phase diffusion growth of sige single crystals. Master's thesis, University of Victoria, 2006.

[27] G.K. Azhdarov, T. Kucukomeroglu, A. Varilci, M. Altunbas, A. Kobya, and P.G. Azhdarov. Distribution of components in ge-si bulk single crystals grown under the continuous feeding of the melt with the second component (si). *Journal of Crystal Growth*, 226:437–442, 2001.

[28] F. Mechighel, N. Armour, S. Dost, and M. Kadja. Mathematical modeling of the dissolution process of silicon into germanium melt. *TWMS Journal of Applied and Engineering Mathematics*, 1(2):127–149, 2011.

[29] N. Armour and S. Dost. Diffusion limited silicon dissolution into a germanium melt. *International Symposium on Physical Sciences in Space: Journal of Physics CS*, 327, 2011.

[30] A. Kidess, N. Armour, and S. Dost. Numerical study of the effect of magnetic fields in dissolution of silicon into germanium melt. *Journal of Crystal Growth*, 312(8):1402–1406, 2010.

[31] N. Armour and S. Dost. Effect of an applied static magnetic field on silicon dissolution into a germanium melt. *Journal of Crystal Growth*, 311(3):780–782, 2009.

[32] N. Armour and S. Dost. Numerical and experimental study of forced mixing with static magnetic field on sige system. *Fluid Dynamics and Materials Processing*, 5(4):331–344, 2009.

[33] N. Armour, S. Dost, and B. Lent. Effect of free surface and gravity on silicon dissolution in germanium melt. *Journal of Crystal Growth*, 299(1):227–233, 2007.

[34] A. Kidess, N. Armour, and S. Dost. A numerical study of silicon dissolution under magnetic fields. *Fluid Dynamics and Materials Processing*, 7:29, 2010.

[35] N. Armour and S. Dost. The effect of a static magnetic field on buoyancy-aided silicon dissolution into germanium melt. *Journal of Crystal Growth*, 306:200–207, 2007.

[36] N. Armour and S. Dost. Effect of a static magnetic field on silicon transport in liquid phase diffusion growth of sige. *Journal of Crystal Research and Technology*, 45(3):244–248, 2010.

[37] N. Armour and S. Dost. Silicon transport under rotating and combined magnetic fields in lliquid phase diffusion growth of sige. *Journal of Crystal Research and Technology*, 45(4):335–340, 2010.

[38] N. Armour and S. Dost. The effect of applied magnetic fields on silicon transport in liquid phase diffusion growth of sige. *ECS Transactions*, 28(5):161–170, 2010.

[39] Walter Borchardt-Ott. *Crystallography*. Springer-Verlag, 1993.

[40] S. Hassani, A. Lusson, A. Tromson-Carli, and R. Triboulet. Seed-free growth of (111) oriented cdte and cdznte crystals by solid state recrystallization. *Journal of Crystal Growth*, 249:121–127, 2003.

[41] S.M. Sze. *Semiconductor Devices: Physics and Technology.* John Wiley & Sons, 1985.

[42] P.T. Landsberg. *Solid State Theory: Methods and Applications.* John Wiley & Sons, 1969.

[43] Charles Kittel. *Introduction to Solid State Physics.* John Wiley & Sons, 1986.

[44] A. Chen. *Semiconductor Alloys.* Plenum Press, 1995.

[45] R. Triboulet, G. Neu, and B. Fotouhi. Growth and characterization of the complete cd1-xznxte alloy series. *Journal of Crystal Growth*, 65:262–269, 1983.

[46] M.Y. Bakirov, R.S. Madatov, and Y.M. Mustagaev. Pv cells based on solid-solution ge-si single crystals. *Geliotekhnika*, 22(3):9–11, 1986.

[47] E.S. Yang. *Fundamentals of Semiconductor Devices.* McGraw Hill Book Company, 1978.

[48] J.C. Tranchart, B. Latorre, C. Foucher, and Y. Le Gouge. Lpe growth of hg1-xcdxte on cd1-yznyte substrates. *Journal of Crystal Growth*, 72:468–473, 1985.

[49] I. Yonenaga. Czochralski growth of gesi bulk alloy crystals. *Journal of Crystal Growth*, 198:404–408, 1999.

[50] Peter Van Zant. *Microchip Fabrication.* McGraw Hill, 2000.

[51] F. Schaffler. *Properties of Advanced Semiconductor Materials.* John Wiley & Sons Inc, 2001.

[52] L. Helmers, J. Schilz, G. Bahr, and W.A. Kaysser. Macrosegregation during bridgman growth of gesi mixed crystals. *Journal of Crystal Growth*, 154:60–67, 1995.

[53] Y. Sato, T. Nishizuka, T. Tachikawa, M. Hoshi, T. Yamamura, and Y. Waseda. Viscosity and density of molten germanium. *High Temperatures - High Pressures*, 32:253–260, 2000.

[54] T.A. Campbell, M. Schweizer, P. Dold, A. Croll, and K.W. Benz. Float zone growth and characterization of gesi single crystals. *Journal of Crystal Growth*, 226:231–239, 2001.

[55] N. Usami, M. Kitamura, K. Obara, Y. Nose, T. Shishido, and K. Nakajima. Floating zone growth of si-rich sige bulk crystal using pre-synthesized sige feed rod with uniform composition. *Journal of Crystal Growth*, 284:57–64, 2005.

[56] M. Ohmori, Y. Iwase, and R. Ohno. High quality cdte and its application to radiation detectors. *Material Science and Engineering*, B16:283–290, 1993.

[57] N. Armour, H. Sheibani, and S.Dost. Growth of cadmium zinc telluride by liquid phase electoepitaxy. *Journal of Crystal Research and Technology*, 41(10):939–945, 2006.

[58] I. Yonenaga and Y. Murakami. Segregation during the seeding process in the czochralski growth of gesi alloys. *Journal of Crystal Growth*, 191:399–404, 1998.

[59] N.V. Abrosimov, S.N. Rossolenko, W. Thieme, A. Gerhardt, and W. Schroder. Czochralski growth of si and ge-rich sige single crystals. *Journal of Crystal Growth*, 174:182–186, 1997.

[60] K.W. Benz and P. Dold. *Semiconductor Crystal Growth from the Melt: Magnetic Fields and Micro-Gravity Effects*, chapter 1, pages 1–30. Transworld Research Network, 2007.

[61] J. Friedrich. *Control of Melt Convection in VGF and CZ Crystal Growth Configurations by using Magnetic Fields: Theory and Examples*, chapter 2, pages 31–60. Transworld Research Network, 2007.

[62] J. Konle, H. Presting, H. Kibbel, K. Thonke, and R. Sauer. Enhanced performance of silicon based photodetectors using silicon/germanium nanostructures. *Solid-State Electronics*, 45:1921–1925, 2001.

[63] S. Yasuhiro. New device applications of sige heterostructures. *Superficies y Vacio*, 16(4):1–5, 2003.

[64] M.I. Kozhukh, L.N. Belokurova, S.B. Vakhrushev, A.N. Titkov, and L.L. Shulpina. Study of ge-si solid solution crystals by x-ray topography and neutron diffraction. *Nuclear Instruments and Methods*, 213:483–487, 1983.

[65] J. Wollweber, D. Schulz, and W. Schroder. Sixge1-x single crystals grown by the rf-heated float zone technique. *Journal of Crystal Growth*, 163:243–248, 1996.

[66] S.A. Healy and M.A. Green. Efficiency enhancements in crystalline silicon solar cells by alloying with germanium. *Solar Energy Materials and Solar Cells*, 28:273–284, 1992.

[67] R. Madar, E. Mastromatteo abd A. Magerl, K.D. Liss, and C. Bernard. Low pressure chemical vapor deposition of massive si1-xgex gradient crystals and applications in short-wavelength diffraction. *Surface and Coatings Technology*, 54/55:229–233, 1992.

[68] P. Alexander and H. Shulman. Ge-si alloy - a new type of nuclear radiation detector. *Nuclear Instruments and Methods*, 104:597–604, 1972.

[69] M. Kurten and J. Schilz. Czochralski growth of sixge1-x single crystals. *Journal of Crystal Growth*, 139:1–5, 1994.

[70] J. Schilz and V.N. Romanenko. Review: Bulk growth of silicon-germanium solid solutions. *Journal of Materials Science: Materials in Electronics*, 6:265–279, 1995.

[71] C.B. Vining. A model for the high-temperature transport properties of heavily doped n-type silicon-germanium alloys. *Journal of Applied Physics*, 69(1):331–341, 1991.

[72] D.M. Rowe. Recent advances in silicon-germanium alloy technology and an assessment of the problems of building the modules for a radioisotope thermoelectric generator. *Journal of Power Sources*, 19:247–259, 1987.

[73] K. Suo, W. Zhang, J. Li, J. Zhao, and Z. Zhou. Thermoelectric properties of czochralski gesi crystal. *Chinese Journal of Structural Chemistry*, 26(10):1247–1251, 2007.

[74] R.W. Olesinski and G.J. Abbaschian. The ge-si system. *Bulletin of Alloy Phase Diagrams*, 5(2):180–183, 1984.

[75] I. Yonenaga. Growth and fundamental properties of sige bulk crystals. *Journal of Crystal Growth*, 275:91–98, 2005.

[76] W.K. Rhim and K. Ohsaka. Thermophysical properties measurement of molten silicon by high temperature electostatic levitator: Density, volume expansion,

specific heat capacity, emissivity, surface tension and viscosity. *Journal of Crystal Growth*, 208:313–321, 2000.

[77] G.L. McVay and A.R. DuCharme. Diffusion of ge in sige alloys. *Physical Review B*, 9(2):627–631, 1974.

[78] N.V. Abrosimov, S.N. Rossolenko, V. Alex, A. Gerhardt, and W. Schroder. Single crystal growth of si1-xgex by the czochralski technique. *Journal of Crystal Growth*, 166:657–662, 1996.

[79] I. Yonenaga and M. Nonaka. Czochralski growth of bulk crystals of ge1-xsix alloys ii. si-rich alloys. *Journal of Crystal Growth*, 191:393–398, 1998.

[80] X. Niu, W. Zhang, G. Lu, and Z. Jiang. Distribution of ge in high concentration ge-doped czochralski-si crystal. *Journal of Crystal Growth*, 267:424–428, 2004.

[81] T. Rittenhouse. *Single Crystal Growth and Characterization of Silicon Germanium Alloys*. PhD thesis, Massachusetts Institute of Technology, 1999.

[82] N. Usami, R. Nihei, I. Yonenaga, Y. Nose, and K. Nakajima. Application of czochralski-grown sige bulk crystal as a substrate for luminescent strained quantum wells. *Applied Physics Letters*, 90, 2007.

[83] D. Yang, J. Chen, H. Li, X. Ma, D. Tian, L. Li, and D. Que. Micro-defects in ge doped czochralski grown si crystals. *Journal of Crystal Growth*, 292:266–271, 2006.

[84] A. Matsui, I. Yonenaga, and K. Sumino. Czochralski growth of bulk crystals of ge1-xsix alloys. *Journal of Crystal Growth*, 183:109–116, 1998.

[85] A. Dahlen, A. Fattah, G. Hanke, and E. Karthaus. Bridgman and czochralski growth of ge-si alloy crystals. *Journal of Crystal Research and Technology*, 29(2):187–198, 1994.

[86] P. Dold, A. Barz, S. Recha, K. Pressel, M. Franz, and K.W. Benz. Growth and characterization of gesi single crystals. *Journal of Crystal Growth*, 192:125–135, 1998.

[87] H. Minakuchi, Y. Okano, and S. Dost. A three-dimensional numerical simulation study of the marangoni convection occuring in the crystal growth of sige by the

float-zone technique in zero gravity. *Journal of Crystal Growth*, 266:140–144, 2004.

[88] K. Lin, P. Dold, and K.W. Benz. Numerical study of influences of buoyancy and solutal marangoni convection on flow structures in a germanium-silicon floating zone. *Journal of Crystal Research and Technology*, 40(6):550–556, 2004.

[89] Y. Azuma, N. Usammi, T. Ujihara, K. Fujiwara, G. Sazaki, Y. Murakami, and K. Nakajima. Growth of sige bulk crystals with uniform composition by utilizing feedback control system of the crystal-melt interface position for precise control of the growth temperature. *Journal of Crystal Growth*, 250:298–304, 2003.

[90] Y. Azuma, N. Usami, T. Ujihara, G. Sazaki, Y. Murakami, S. Miyashita, F. Fujiwara, and K. Nakajima. Growth of sige bulk crystal with uniform composition by directly controlling the growth temperature at the crystal-melt interface using in-situ monitoring system. *Journal of Crystal Growth*, 224:204–211, 2001.

[91] K. Nakajima, T. Kusunoki, Y. Azuma, N. Usami, K. Fujiwara, T. Ujihara, G. Sazaki, and T. Shishido. Compositional variation in si-rich sige single crystals grown by multi-component zone melting method using si seed and source crystals. *Journal of Crystal Growth*, 240:373–381, 2002.

[92] A. Borshchevsky and J.P. Fleurial. Growth of heavily-doped sige from metallic solutions. *Journal of Crystal Growth*, 128:331–337, 1993.

[93] S. Dost and B. Lent. *Single Crystal Growth of Semiconductors froom Metallic Solutions*. Elsevier, 2007.

[94] R.U. Barz, G. Gerbeth, U. Wunderwald, E. Buhrig, and Y.M. Gelfgat. Modelling of the isothermal melt flow due to rotating magnetic fields in crystal growth. *Journal of Crystal Growth*, 180:410–421, 1997.

[95] C.K. Ghaddar, C.K. Lee, S. Motakef, and D.C. Gillies. Numerical simulation of thm growth of cdte in presence of rotating magnetic fields (rmf). *Journal of Crystal Growth*, 205:97–111, 1999.

[96] S. Dost, Y. Liu, B. Lent, and R.F. Redden. A numerical simulation study for the effect of applied magnetic field in growth of cdte single crystals by the travelling heater method. *International Journal of Applied Electromagnetics and Mechanics*, 17:271–288, 2003.

[97] S. Patankar. *Numerical Heat Transfer and Fluid Flow.* Taylor and Francis, 1980.

[98] K.S. Surana, S. Allu, P.W. Tenpas, and J.N. Reddy. k-version of finite element method in gas dynamics: Higher-order global differentiability numerical solutions. *International Journal for Numerical Methods in Engineering*, 69(6):1109–1157, 2007.

[99] A.J. Baker. *Finite Element Computational Fluid Mechanics.* Hemisphere Publishing, 1983.

[100] V. Golyshev, M. Gonik, and V. Tsvetovsky. Study of thermal conductivity close to melting point. *High Temperatures - High Pressures*, 35:139–148, 2003.

[101] V. Alexiades and R.P. Wichner. Calculation of the specific and volumetric enthalpies of ge-si alloys. Oak Ridge National Labratory - Martin Marietta Energy Systems Libraries, 1988.

[102] Y. Okano, S. Umemura, Y. Enomoto, Y. Hayakawa, M. Kumagawa, A. Hirata, and S. Dost. Numerical study of marangoni convection effect on the melting of gasb/insb/gasb. *Journal of Crystal Growth*, 235:135–139, 2002.

[103] A. Hirata, M. Tachibana, Y. Okano, and T. Fukuda. Magnetic field effects on marangoni and natural convection in a rectangular open boat. *Journal of Chemical Engineering of Japan*, 25(1):62–66, 1992.

[104] H.M. Lu, T.H. Wang, and Q. Jiang. Surface tension and self-diffusion coefficient of liquid si and ge. *Journal of Crystal Growth*, 293:294–298, 2006.

[105] K. Heinrich and D. Newbury. *Electron Probe X-Ray Microanalysis*, pages 516–535. ASM, 1986.

[106] J. Verhoeven. *Scanning Electron Microscopy*, pages 490–515. ASM, 1986.

[107] M. Dejmek and C.A. Ward. A statistical rate theory study of interface concentration during crystal growth or dissolution. *Journal of Chemical Physics*, 108:8698–8704, 1998.

[108] S. Yesilyurt, L. Vujisic, S. Motakef, F.R. Szofran, and M.P. Volz. A numerical investigation of the effect of thermoelectromagnetic convection (temc) on the bridgman growth of ge1-xsix. *Journal of Crystal Growth*, 207:278–291, 1999.

[109] Y.Y. Khine and J.S. Walker. Thermoelectric magnetohydrodynamic effects during bridgman semiconductor crystal growth with a uniform axial magnetic field. *Journal of Crystal Growth*, 183:150, 1998.

[110] E. Yildiz, S. Dost, and M. Yildiz. A numerical simulation study of the effect of magnetic fields in liquid phase diffusion growth of sige single crystals. *Journal of Crystal Growth*, 291:497–511, 2006.

[111] G. Sazaki, Y. Azuma, S. Miyashita, N. Usami, T. Ujihara, K. Fujiwara, Y. Murakami, and K. Nakajima. In-situ monitoring of the position and temperature at the crystal-solution interface. *Journal of Crystal Growth*, 236:125–131, 2002.

[112] Z. Jiang, W.. Zhang, X. Niu, and L. Yan. Infrared measurement of ge concentration in cz-si. *Journal of Crystal Growth*, 279:65–69, 2005.

[113] H. Baker, editor. *ASM Handbook, Volume 3: Alloy Phase Diagrams.* ASM, 1992.